

國立臺灣大學理學院化學研究所

碩士論文

Department of Chemistry


College of Science

National Taiwan University

Master Thesis

中孔洞氧化矽奈米粒子的修飾及生物醫學上之應用

**Modification of Mesoporous Silica Nanoparticles for
Biomedical Applications**



蘇怡帆

Yi-Fan Su

指導教授：牟中原 博士

Advisor: Chung-Yuan Mou, Ph.D.

中華民國 100 年 6 月

June, 2011

謝誌

嫩芽綠了枝頭，暖風輕拂枝梢，轉眼間數個年頭已過；猶記得初踏進實驗室的陌生不安和那抹青澀，中間有過淚水卻也不曾少過歡笑，就這樣要畢業了。

謝謝指導教授 牟中原博士這一路的厚愛和照料，牟老師做為指導教授真的會幸福地讓人妒嫉的，因為老師對學生的好幾近寵溺了；也謝謝 洪燕博士一直以來的教導和關愛，和老師天南地北的聊天成了這些日子來最美好的光景之一。因為有你們的體諒和永遠的支持，我才能從羽翼不豐到含淚也能笑著飛行。

論文能臻至完善，除了感謝指導教授 牟中原博士和實驗室 洪燕博士，還要謝謝口試委員 陳昭岑博士和 吳嘉文博士的悉心閱覽以及寶貴建議；研究的路上也要感謝中央研究院生物醫學科學研究所 張程博士實驗室團隊的傾力幫助，完備了我的研究成果。

謝謝實驗室學長姐們的悉心拉拔和呵護備至，才讓自己慢慢茁壯長成至可獨當一面；也因為同屆夥伴們的並肩相伴和相知相惜，讓我們能帶著美好的記憶參與了彼此生命中重要的時刻；而學弟妹們的歡鬧喧嘩也總在不知不覺中給自己帶來了咬牙面對的力量。最感幸福的是，能找到一輩子讓自己珍惜的朋友，且我們約定好這些真摯且溫暖的陪伴將會一直地綿延。

也謝謝我最親愛且最在乎的家人們，謝謝你們的無條件支持及義無反顧的愛和包容；在外受怕受委屈時，你們永遠敞開的臂彎總讓我又能看見希望和勇氣。

謝謝你們，我的師長、實驗室夥伴和家人們，還有每一位在這一路上鼓勵我陪伴我且不求回報幫助我的朋友們，有你們是我最幸福的際遇。

摘要

中孔洞氧化矽奈米材料具有高表面積、大孔體積、均勻孔徑大小、表面容易修飾以及生物相容性佳等優點；因此在本研究中，我們以中孔洞氧化矽奈米材料作為主軸，依其結構與生醫應用上不同分成兩個主題。

第一部分我們成功利用共價修飾的方法，發展出具有螢光及釷金屬順磁性質的多功能氧化矽奈米複合材料($\text{Gd}(\text{OH})_3\text{-FITC@MSN}$)；此多功能中孔洞氧化矽材料具有高弛緩率 (relaxivity) 及穩定螢光等性質，並可藉細胞吞噬作用成功進入細胞內且對於細胞只存有極低的生物毒性。更重要的是 $\text{Gd}(\text{OH})_3\text{-FITC@MSN}$ 材料相較臨床使用的核磁共振顯影劑有更好的影像對比效果，再加上螢光光學及中孔洞材料等特點，此材料在未來影像追蹤以及藥物釋放等應用上有很大的潛力。

第二部份我們系統性地探討聚乙二醇分子 (polyethylene glycol, PEG) 的分子量及表面修飾密度對中孔洞氧化矽奈米材料的影響。我們找到最適合的聚乙二醇修飾條件，使中孔洞氧化矽奈米粒子在模擬生理條件的培養液中有最佳的粒子穩定性且可以成功降低小鼠巨噬細胞 (RAW 264.7) 的非專一性吞噬，並進而避開身體內的網狀內皮系統 (reticuloendothelial system, RES)，對於提升生物體內專一性標定及藥物輸送的效率有很大的幫助。

關鍵字：中孔洞氧化矽奈米材料、多功能氧化矽奈米複合材料、核磁共振顯影、顯影劑、聚乙二醇修飾、巨噬細胞吞噬

Abstract

Mesoporous silica nanoparticles (MSNs) are emerging as promising candidates in using these materials for biomedical applications because of the unique characteristics, including high surface area, uniform pore size, easy modification and great biocompatibility. In first part, we have successfully developed two kinds of materials base on mesoporous silica nanoparticles (MSN) for biomedical applications. The first part shows the synthesis and characterization of a multifunctional nanomaterial, Gd(OH)₃-FITC@MSN, possessing magnetic, fluorescent and porous properties. Its utility for both magnetic resonance and optical imaging was clearly demonstrated *in vitro*. The result shows Gd(OH)₃-FITC@MSN performed well for cellular magnetic resonance imaging (MRI) even at high magnetic field (7T), indicating it could be a promising T₁ or T₂ contrast agent.

The second part presents a systematic study of 50 nm MSN modified with PEG of different molecular weights and surface chain density. The results show that, as the surface of MSN mostly covered by PEG with molecular weight of 30 kDa, the PEGylated MSN could stably suspend in cell-culture medium and physiology environments without agglomeration and obvious size changes even incubated for two weeks. Besides, MSNs conjugated with PEG chains effectively reduce non-specific uptake of RAW 264.7 macrophage cells indicating these particles could escape from the innate immune system which is critical for efficient target-specific delivery.

Keywords: Mesoporous silica nanoparticles, multifunctional nanoaprobates, MRI, contrast agents, PEGylation, phagocytosis

Table of Contents

摘要.....	I
Abstract.....	II
Table of Contents.....	III
List of Figures.....	V
List of Schemes.....	X
List of Tables.....	XI
Chapter One General Introduction.....	1
1.1 Emerging Nanomaterials.....	1
1.2 Mesoporous Materials.....	10
1.3 Mesoporous Silica Nanoparticles (MSN) in Biomedical Applications.....	14
Chapter Two Gadolinium-functionalized Mesoporous Silica Nanoparticles as Magnetic Resonance Imaging Contrast Agents.....	21
2.1 Introduction.....	21
2.1.1 Biomedical Imaging Modalities.....	21
2.1.2 Introduction of Magnetic Resonance Imaging (MRI).....	24
2.2 Experiments.....	30
2.2.1 Materials.....	30
2.2.2 Synthesis of Gd(OH) ₃ @MSN.....	30
2.2.3 Synthesis of Gd(OH) ₃ -FITC@MSN.....	32
2.2.4 Cell culture and Assays.....	34
2.2.5 Physical and Chemical Characterization.....	37
2.2.6 Magnetic Resonance Characterization.....	39

2.3	Results and Discussion.....	41	
2.3.1	Properties of Gd(OH) ₃ @MSNs through Two Synthetic Procedures.....	44	
2.3.2	Characterization of Various Gadolinium-Loaded MSNs.....	53	
2.3.3	Characterization of Gd(OH) ₃ -FITC@MSN.....	60	
2.3.4	Biological Applications of Gd(OH) ₃ -FITC@MSN.....	65	
2.4	Conclusion.....	73	
Chapter Three			
Controlled PEGylation of Mesoporous Silica Nanoparticles for			
Reduced Non-specific Uptake by Macrophage Cells.....			74
3.1	Introduction.....	74	
3.1.1	Brief Introduction of Reticuloendothelial system (RES).....	74	
3.1.2	Commonly Used Polymers for Escaping from RES.....	76	
3.1.3	Polyethylene Glycol (PEG) for Surface Modification – PEGylation.....	78	
3.2	Experiments.....	82	
3.2.1	Materials.....	82	
3.2.2	Synthesis of Thiol Group Modified Mesoporous Silica Nanoparticles.....	85	
3.2.3	Procedure of Polyethylene Glycol Modification (SH-RITC@MSN-PEG).....	86	
3.2.4	Cell Culture and Assays.....	88	
3.2.5	Characterization.....	89	
3.3	Results and Discussion.....	91	
3.3.1	Quantification of Thiol Group.....	92	
3.3.2	Systematic Study of PEGylation of Rhodamine B Dye Conjugated MSN (SH-RITC@MSN-PEG).....	94	
3.4	Conclusion.....	111	
Reference.....			112

List of Figures

Figure 1.1 Schematic illustration of multifunctional silica-based architectures.....	2
Figure 1.2 Synthetic diagram of magnetic gold nanoshells (Mag-GNS).....	3
Figure 1.3 Sizes and emission maxima of quantum dots with different compositions...4	
Figure 1.4 Quantum dots served as contrast agents for bioimaging applications.....	5
Figure 1.5 Schematic representation of oleic acid and pluronic coated iron oxide nanoparticles as drug carriers.....	6
Figure 1.6 Gold nanoparticles served as heat source.....	8
Figure 1.7 (A) Transmission electron micrograph of MCM-41 with 4 nm size pores. (B) X-ray diffraction pattern of calcined MCM-41.....	11
Figure 1.8 Two pathways for the LCT mechanism.....	13
Figure 1.9 (A) Merged confocal image of rMSCs incubated with Mag-Dye@MSN for 1 hour. The cytoskeleton was stained with rhodamine phalloidin (red) and the cell nucleus with DAPI (blue). The T2-weighted MR images of: (B) labeled rMSCs after treatment with Mag-Dye@MSN for 1 h, and (C) unlabeled rMSCs.....	15
Figure 1.10 Fluorometric titration curves: relative fluorescence emission ($\lambda_{\text{ex}} = 370 \text{ nm}$, $\lambda_{\text{em}} = 420 \text{ nm}$) for analogous molecular (aminoanthracene)-based receptor (Δ), MSN-based sensor (\blacklozenge) and fumed silica-based sensor (\blacktriangle) in the presence of increasing amounts of ATP anion.....	17
Figure 1.11 Confocal images of FITC-MSN (green) internalized by 3T3-L1 cells; cell skeleton was stained with rhodamine phalloidin dye (red).....	18
Figure 1.12 Schematic model of the sustained-release mechanism of MSN-TA loaded with anionic drugs. (a) Before drug adsorbed, (b) after drug adsorbed, (c) drugs released by electrostatic repulsion under neutral environment, and (d) drugs release by increasing ionic strength.....	19

Figure 1.13 Schematic representation of the photoinduced intracellular controlled release of AuNPs-MSN carrying anticancer drug.....	20
Figure 2.1 (A) Spins align to magnetic field B_0 and precess under Larmor frequency ω_0 . (B) Magnetization of spins change after introducing RF pulse.....	25
Figure 2.2 (A) Schematic representation of T_1 relaxation. ²⁵ (B) Plot of M_z versus time after RF pulse.....	25
Figure 2.3 (A) Schematic representation of T_2 relaxation. ²⁵ (B) Plot of M_{xy} versus time after RF pulse.....	26
Figure 2.4 Electron configuration and magnetic moment of metal ions.....	27
Figure 2.5 Parameters influencing relaxivity.....	29
Figure 2.6 TEM images of (A) $Gd(OH)_3@MSN-A$ and (B) $Gd(OH)_3@MSN-B$	44
Figure 2.7 (A) TEM image of $Gd(OH)_3@MSN-B$, where a) is referred to the large aggregation complex and b) represents hollow sphere cores with porous surrounding. EDS results of a) and b) are shown in (B) and (C), respectively. The scale bar is $0.2 \mu m$	47
Figure 2.8 Low angle XRD patterns of surfactant-free (A) $Gd(OH)_3@MSN-A$ and (B) $Gd(OH)_3@MSN-B$	48
Figure 2.9 Relaxivities measurements of $Gd(OH)_3@MSN$ synthesized via process A (designated as A) and B (designated as B) and MultiHance® at 0.54 T. Relaxivity is the slope of the plot of concentration versus $1/T_n$, $n=1$ or 2	50
Figure 2.10 (A) T_1 - maps of $Gd(OH)_3@MSN-FITC$ synthesized by process A (upper two panels) and MultiHance® (3 rd and 4 th panels). For both sets, the spots were H_2O , $[Gd] = 0.1M$ (1 st row), $0.2M$, $0.4M$ and $0.8M$ (2 nd row) sequentially from left to right. (B) The same T_1 data as (A) but with colors to better differentiate T_1 variations. (C) T_1 -maps of $Gd(OH)_3@MSN$ synthesized by process B (upper two panels) and MultiHance® (3 rd and 4 th panels). For both sets, the spots were H_2O , $[Gd] = 0.1M$ (1 st	

row), 0.2M, 0.4M and 0.8M (2 nd row) sequentially from left to right. (D) The same T ₁ -map data as (A) but with colors to better differentiate the T ₁ variations. For (A) to (D), scale bars represent the T ₁ values, larger numbers are longer T ₁	52
Figure 2.11 TEM images of Gd(OH) ₃ @MSN with different Gd loading (A) 0 %, (B) 1.9%, (C) 3.5%, (D) 7.2% and (E) 13.2% obtained from ICP-MS.....	53
Figure 2.12 XRD patterns of Gd(OH) ₃ @MSN with different Gd loading (A) 0 %, (B) 1.9%, (C) 3.5%, (D) 7.2% and (E) 13.2%.....	54
Figure 2.13 N ₂ adsorption-desorption isotherms of Gd(OH) ₃ @MSN with different Gd loading (A) 0 %, (B) 1.9%, (C) 3.5%, (D) 7.2% and (E) 13.2%.....	55
Figure 2.14 T ₁ -weighted phantom MR images of Gd(OH) ₃ @MSN with different Gd loading (3.5%, 7.2%, and 13.2%) and Magnevist® with a 4.7T Biospec spectrometer using inversion recovery sequence; images were taken at T _R = 400 ms.....	59
Figure 2.15 T ₂ -weighted phantom MR images of Gd(OH) ₃ @MSN with different Gd loading (3.5%, 7.2%, and 13.2%) and Magnevist® with a 4.7T Biospec spectrometer using spin-echo sequence; images were taken at T _E = 80 ms.....	59
Figure 2.16 TEM images of as-synthesized Gd(OH) ₃ -FITC@MSN, (A) and (B) were taken under different magnifications.....	61
Figure 2.17 XRD patterns of extracted Gd(OH) ₃ -FITC@MSN.....	61
Figure 2.18 Dynamic light scattering (DLS) measurements of Gd(OH) ₃ -FITC@MSN.....	61
Figure 2.19 T ₁ relaxivity plot of Gd(OH) ₃ -FITC@MSN taken under 1.41T.....	63
Figure 2.20 T ₂ relaxivity plot of Gd(OH) ₃ -FITC@MSN taken under 1.41T.....	63
Figure 2.21 Flow cytometry study on NIH3T3 cell-uptake of Gd(OH) ₃ -FITC@MSN with different concentration.....	67
Figure 2.22 (A) and (D) Fluorescence, (B) and (E) optical and (C) and (F) fluorescence- and optical-merged images of NIH3T3 cells after incubated with 200 µg / mL Gd(OH) ₃ -FITC@MSN for 4 hours.....	67

Figure 2.23 MTT assay of NIH3T3 cells incubated with different amount of Gd(OH) ₃ -FITC@MSN for 4 hours.....	68
Figure 2.24 (A) T ₁ -weighted and (B) T ₂ -weighted MR images of NIH3T3 cells treated with Gd(OH) ₃ -FITC@MSN for 4 hours using 4.7 T MR instrument.....	69
Figure 2.25 (A) T ₁ -weighted and (B) T ₂ -weighted MR images of cells treated with Gd(OH) ₃ -FITC@MSN for 4 hours using 7 T MR instrument.....	70
Figure 2.26 (A) T ₁ -weighted and (B) T ₂ -weighted MR images of embryonic stem cells treated with Gd(OH) ₃ -FITC@MSN for 4 hours using 4.7 T MR instrument.....	72
Figure 2.27 Fluorescence images of embryonic cells labeled with (A) 25 µg / mL (B) 50 µg / mL (C) 100 µg / mL and (D) 200 µg / mL of Gd(OH) ₃ -FITC@MSN. The nuclei were stained by DAPI.....	72
Figure 3.1 The fate of nanoparticles after the intravenous injection.....	75
Figure 3.2 Typical polymers used as hydrophilic coating for RES-evading nanoparticles.....	76
Figure 3.3 TEM images of (A) to (I) SH-RITC@MSN-PEG _{A-I} and (O) SH-RITC@MSN.....	97
Figure 3.4 Hydrodynamic size changes in PBS for various incubation periods. Control is SH-RITC@MSN whereas A to I are corresponds to PEGylated MSNs in Table 3.4.....	100
Figure 3.5 Hydrodynamic size changes in DMEM for various incubation periods. Control is SH-RITC@MSN whereas A to I are corresponds to PEGylated MSNs in Table 3.4.....	101
Figure 3.6 Hydrodynamic size changes in DMEM plus 10% FBS for various incubation periods. Control is SH-RITC@MSN whereas A to I are corresponds to PEGylated MSNs in Table 3.4.....	103
Figure 3.7 Cellular uptake of SH-RITC@MSN and SH-RITC@MSN-PEG _{B,C,E,H} in	

RAW 264.7 in DMEM using flow cytometry. (A) RAW 264.7 without treatment. RAW264.7 treated with (B) SH-RITC@MSN, (C) SH-RITC@MSN-PEG_C, (D) SH-RITC@MSN-PEG_B, (E) SH-RITC@MSN-PEG_E and (H) SH-RITC@MSN-PEG_H.....106

Figure 3.8 Flow cytometry determination of SH-RITC@MSN and SH-RITC@MSN-PEG_{B,C,E,H} in RAW 264.7 under DMEM analyzed by the percentage of nanoparticle labeled cells. Cell only represents for RAW 264.7 without treatment. Cells treated with SH-RITC@MSN are as control. C to H are SH-RITC@MSN-PEG_{C,B,E,H}.....106

Figure 3.9 Cellular uptake of SH-RITC@MSN and SH-RITC@MSN-PEG_{B,C,E,H} in RAW 264.7 in DMEM-FBS using flow cytometry. (A) RAW 264.7 without treatment. RAW264.7 treated with (B) SH-RITC@MSN, (C) SH-RITC@MSN-PEG_C, (D) SH-RITC@MSN-PEG_B, (E) SH-RITC@MSN-PEG_E and (H) SH-RITC@MSN-PEG_H.....109

Figure 3.10 Flow cytometry determination of SH-RITC@MSN and SH-RITC@MSN-PEG_{B,C,E,H} in RAW 264.7 under DMEM-FBS analyzed by the percentage of nanoparticle labeled cells. Cell only represents for RAW 264.7 without treatment. Cells treated with SH-RITC@MSN is denoted as control. And C to H are SH-RITC@MSN-PEG_{C,B,E,H}.....110

List of Schemes

Scheme 2.1 Synthetic procedure of Gd(OH) ₃ -FITC@MSN.....	41
Scheme 2.2 Proposed equations of the formation of Gd(OH) ₃	42
Scheme 2.3 Two different synthetic procedures for Gd(OH) ₃ @MSN.....	43
Scheme 3.1 PEG modification of Fe ₃ O ₄ nanoparticles through DPA-PEG-COOH.....	80
Scheme 3.2 The formation and application of SH-RITC@MSN-PEG.....	91
Scheme 3.3 Mechanism of thiol PEGylation.....	94



List of Tables

Table 1.1 Characteristics and representative bio-applications of several commonly used nanomaterials.....	1
Table 2.1 Comparison of several imaging modalities.....	21
Table 2.2 Gd-incorporated amount analyzed by ICP-MS and hydrodynamic sizes obtained from DLS of Gd(OH) ₃ @MSN-A and -B.....	48
Table 2.3 Structural and textural data of Gd(OH) ₃ @MSN with different Gd loading...55	
Table 2.4 Relaxivity of Gd(OH) ₃ @MSN with different Gd loading at 1.41T.....	57
Table 2.5 Relaxivity of Gd(OH) ₃ @MSN with different Gd loading and commercial contrast agent Magnevist® at 4.7T.....	57
Table 2.6 Relaxivities, r_1 and r_2 of Gd(OH) ₃ -FITC@MSN and commercial contrast agent, Magnevist® under 1.41T and 4.7T.....	63
Table 2.7 T ₁ relaxation time of NIH3T3 cells treated with Gd(OH) ₃ -FITC@MSN.....	70
Table 3.1 Methoxy-poly(ethylene glycol) coated gold nanoparticles (mPEG-GNP) characteristic and <i>in vivo</i> behavior.....	79
Table 3.2 Nine conditions for coating SH-RITC@MSN with PEG.....	86
Table 3.3 Quantification of sulfur elements (w.t.%) from thiol groups of SH@MSN with adding different amounts of MPTMS.....	93
Table 3.4 SH-RITC@MSN-PEG _{A-1} with nine combinations of mole ratio of thiol groups to PEG and PEG molecular weights.....	95
Table 3.5 The comparison of zeta potentials of MSNs (SH-RITC@MSN) and PEGylated MSNs (SH-RITC@MSN-PEG) by PEG=xk;1:1 chains of different molecular weights (x=10, 20 and 30) at the mole ratio of thiol groups to PEG (1:1) in water.....	101
Table 3.6 The zeta potentials of MSNs (SH-RITC@MSN) and PEGylated MSNs	

(SH-RITC@MSN-PEG) by PEG=xk;y;z chains of different molecular weights (x=20 and 30) with various mole ratios of thiol groups to PEG (y:z) in water.....107



Chapter One General Introduction

1.1 Emerging Nanomaterials

In the past decades, nanomaterials have emerged as the most promising candidates for biomedical applications because of its unique characteristics. When the sizes of materials have been reduced from bulk to nano, they would possess unique chemical and physical properties, including small size, high surface area, quantum confinement and novel optical and magnetic effects. Table 1.1 lists several frequently reported nanomaterials in biomedical field.¹ When diverse nanomaterials are appropriately integrated into a single nanostructured particle system with combined properties, the resulting nanoplatform could be effectively applied to diagnostic and therapeutic techniques, such as controlled release of drugs, multifunctional imaging and specific targeting.² Herein, we'd like to introduce some nanomaterials and their corresponding nanoparticle systems, which have attracted significant attention for biomedical applications recently.

Table1.1 Characteristics and representative bio-applications of several commonly used nanomaterials.¹

Core material	Characteristics	Applications
SiO ₂	Biocompatibility	Biocompatible by surface coating
CdSe	Luminescence, photo-stability	Imaging, Sensing
Fe ₂ O ₃ /Fe ₃ O ₄	Magnetic property	MR imaging and biomolecule purification
Au	Optical absorption, fluorescence and fluorescence quenching, stability	Bimolecular recognition, delivery, sensing

Silica-Based Nanoparticles

Nanostructured silica materials have received enormous attention in scientific research due to the uniform size, excellent chemical stability, ease of formation, versatile functionalization chemistry, relatively low cytotoxicity, and potential applications.

Silica has also shown itself being capable of enhancing the functionality for further biomedical applications via chemical incorporation and doping of numerous molecular species. Figure 1.1 shows various types of silica-based architectures being designed, including silica as the core with molecular species modified on the surface, silica shell as where particles encapsulated in a layer of silica by Stöber process³ or reverse microemulsion syntheses⁴, and hybrid architectures assembling nanoparticles into the silica conjugated with molecular species.²

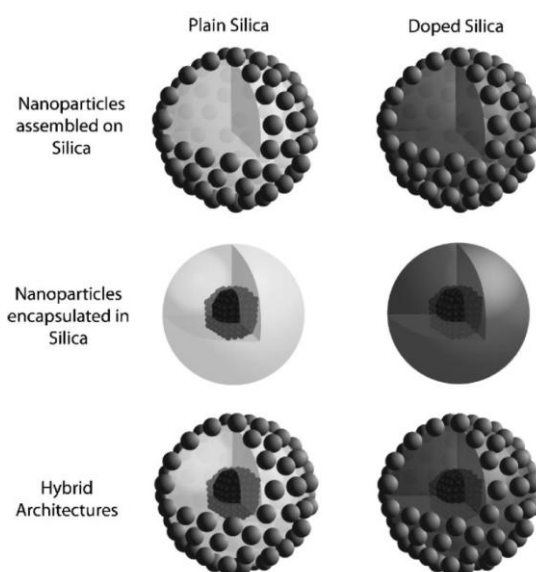


Figure 1.1 Schematic illustration of multifunctional silica-based architectures.²

For example, in 2006, Hyeon et al.⁵ reported the synthesis of the magnetic gold nanoshells through assembling 7 nm magnetite nanoparticles on 100 nm silica nanoparticles as the core and depositing a subsequent gold nanoshell of 15 nm thickness. The main concept is illustrated in Figure 1.2. The resulting magnetic gold nanoshells could be used both as a near-infrared (NIR) photothermal therapeutic agent due to the absorbance of gold in NIR range and a MIR contrast agents by the characteristics of magnetite nanoparticles. Also, by conjugating HER2 specific antibody, the magnetic gold nanoshells could target SKBR-3 breast cancer cells and ablate the cancer cells by NIR radiation.

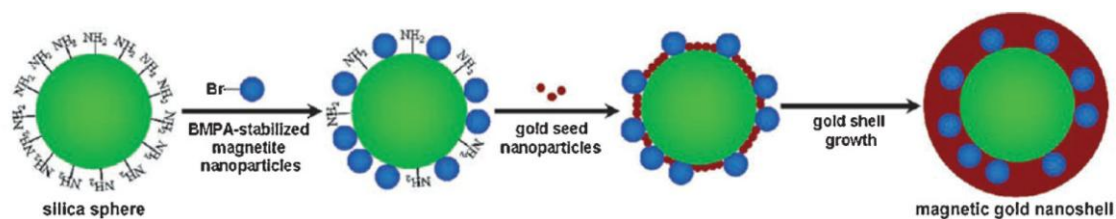


Figure 1.2 Synthetic diagram of magnetic gold nanoshells (Mag-GNS).⁵

Quantum Dots

Quantum dots are single crystals whose size and shape could be precisely tuned by the temperature, duration and ligand molecules applied in the synthetic process, which also yields the size- and composition-dependent absorption and emission. Figure 1.3 indicates that quantum dots can be synthesized from a wide variety of semiconductor materials (II-VI: CdS, CdSe, CdTe, etc; III-V: InP, InAs, etc; IV-VI:

PbSe, etc) characterized by different bulk band gap energies. And the emission wavelengths vary from 400 to 1350 nm, with sizes of quantum dots ranging from 2 to 9.5 nm.

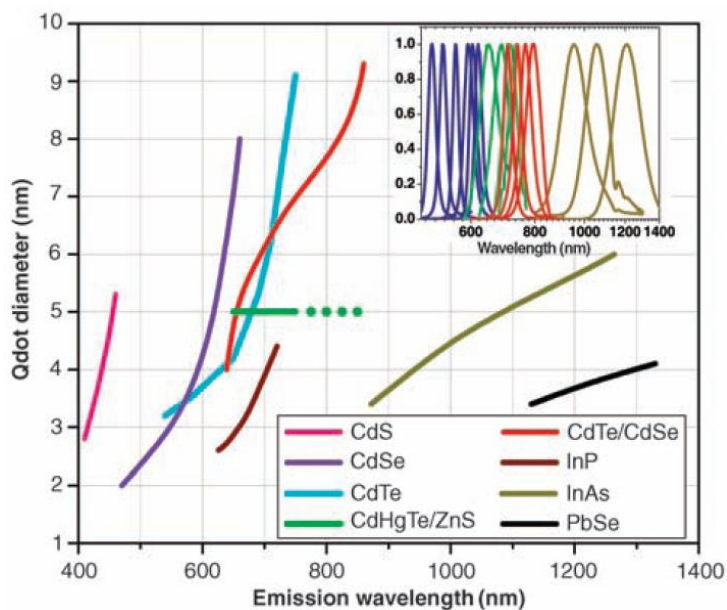


Figure 1.3 Sizes and emission maxima of quantum dots with different compositions.⁶

For biomedical applications, quantum dots possess advantages as following

- (i) quantum yield enhancement and longer life times which proved more photo-stable than current organic fluorophores;
- (ii) smaller sizes and emission extending to the near-infrared (NIR) region avoiding the cell auto-fluorescence in the visible spectrum;
- (iii) possibility of surface functionalizations; and
- (iv) sensitivity to electric or magnetic fields which could be used as contrast reagents depicted in Figure 1.4.⁶

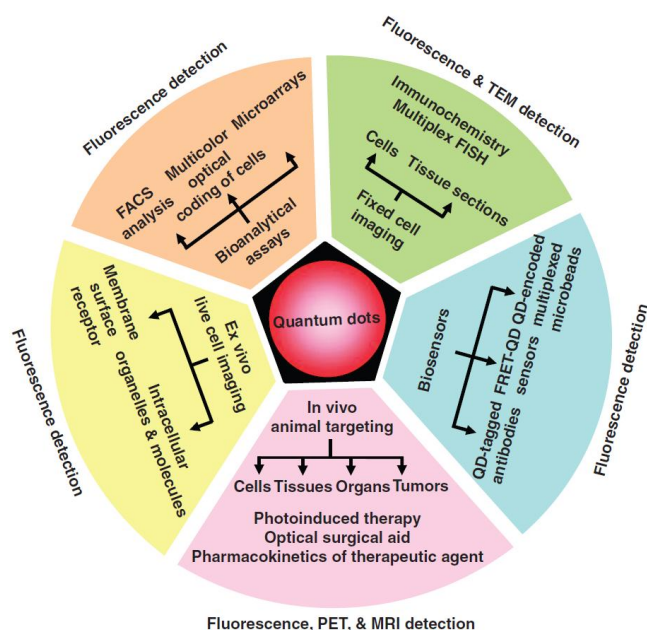


Figure 1.4 Quantum dots served as contrast agents for bioimaging applications.⁶

Iron Oxide Nanoparticles

Superparamagnetic iron oxide nanoparticles (SPINO) possess uniform chemical and physical properties, including single domains of about 5-20 nm in diameter and high magnetization values. Combining the intrinsic characteristics with proper surface coatings of the iron oxide nanoparticles would enable them potential for extensive biomedical applications, such as (i) cellular therapy, for example used for cell targeting, cell labeling, and to separate and purify cell populations; (ii) magnetic resonance imaging (MRI) contrast agent for its superparamagnetic behavior; (iii) hyperthermia by magnetic induction, capable for cancer treatment which could be applied to deep region of the body since magnetic field is not absorbed by tissues and used for tissue repair which joins two tissue surfaces by heating them sufficiently; and

(iv) drug delivery where magnetic iron oxides serve as carriers of drugs for site-specific delivery.⁷

Labhassetwar and his coworkers have developed water-dispersible iron oxide magnetic nanoparticles coated with oleic acid and pluronic F-127 and the nanoparticles could be loaded with high doses of water-insoluble anti-cancer drugs.⁸ Figure 1.5 shows that drugs are trapped into oleic acid shell, and the aqueous dispersity is resulted from pluronic anchoring at the interface of oleic acid with water. This system is demonstrated to have slow drug release over 2 weeks under *in vitro* conditions, and possess dose-dependent anti-proliferative effects on breast and prostate cancer cells. Also, the magnetic characteristic of iron oxide nanoparticles is not affected by the surface modification.

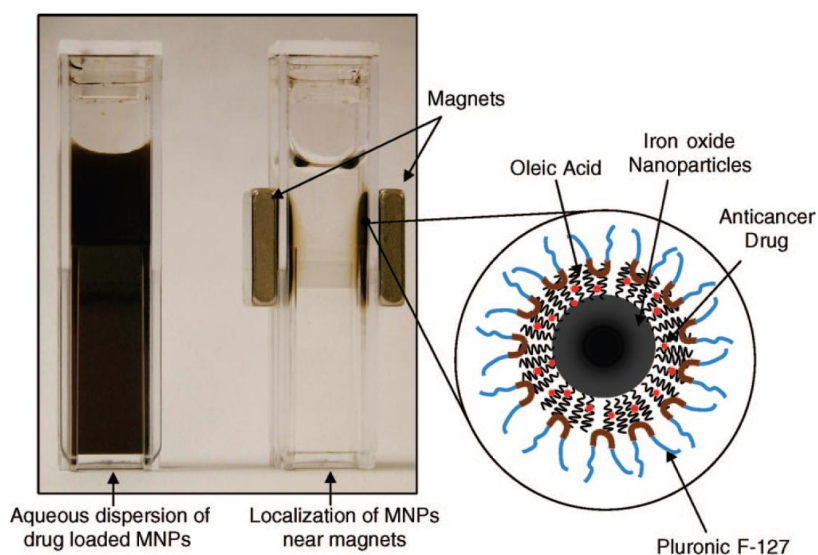


Figure 1.5 Schematic representation of oleic acid and pluronic coated iron oxide nanoparticles as drug carriers.⁸

Gold Nanoparticles

Gold nanoparticles, also called gold colloids, have attracted lots of attention for its uniform particle size and size-related electronic, magnetic and optical properties due to the so-called “quantum size effect”.⁹ Gold nanoparticles applied in the biomedical field so far could be classified into four concepts, including labeling, delivering, heating and sensing.¹⁰

For labeling, gold nanoparticles could be directed to the region of interest and provide visualization and observation of the region since they are promising contrast agents as they could be visualized with a wide variety of techniques. Due to the well-known phenomenon “surface plasma resonance”, they strongly absorb visible light and could be detected by UV-Vis spectrometer. The absorbance of visible light also enables the gold particles to be detected through either photothermal imaging or photoacoustic imaging. Besides, the gold nanoparticles could be visualized by transmission electron microscopy (TEM) as its interaction with both electron waves and X-rays.

Gold nanoparticles have been used as a delivery vehicle into cells for many years. The most common delivery methods are through gene gun which introduce plasmid DNA into plant cells for specific protein expression to achieve gene therapy, or simply deliver targeting anti-cancer drugs to cancer tissues via cell internalization. For

the above delivery purposes, no special characteristics of gold nanoparticles are applied except they are small, stable, easy to be modified through thiol-gold bond, and relatively biocompatible.

Gold nanoparticles also can act as a heat source when absorbs light irradiating. The free electrons inside the gold nanoparticles could be excited by the excitation at the plasmon resonance frequency and then relaxed to crystal lattice following the thermal energy transfer, so that the heat could be generated and released into the surrounding environment. Figure 1.6 shows three possible applications of gold nanoparticles as a heating source: (a) hyperthermia, where cells are killed when the temperature is raised as gold nanoparticles absorb light; (b) receptor-ligand bindings by heat generated; and (c) through local heating to open the polymer coating and release the cargo.

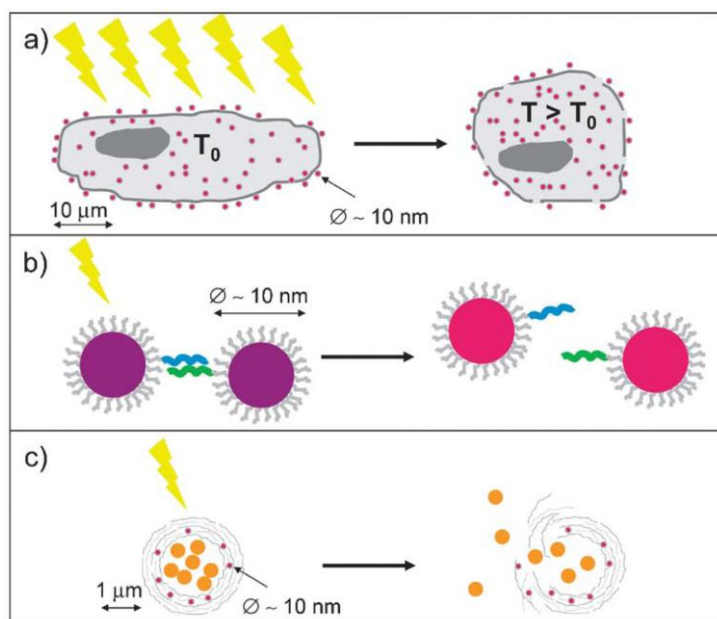


Figure 1.6 Gold nanoparticles served as heat source.¹⁰

Gold nanoparticles could also work as sensors for detection of specific analytes when conjugate with analyte-specific ligands. Usually, the changes in optical properties could indicate the presence of analytes. For instance, surface plasmon frequency in gold nanoparticles would change when the analytes bind to gold nanoparticles, fluorescence quenching results when fluorophores of analytes are in close proximity to gold nanoparticles, and surface-enhanced Raman scattering (SERS) occurs when molecules are close to gold surfaces. All could provide optical read-outs for sensing applications.

1.2 Mesoporous Silica Materials

In 1992, researchers at the Mobil Research and Development Corporation reported the exciting discovery of M41S materials which possess regular arrays of uniform channels and controllable pore sizes through the surfactant templates.¹¹ As the first synthesized mesoporous solid, MCM-41 shows narrow pore-size distribution and regular pore arrangement and is also the most investigated member of M41S family.

There are two special aspects for MCM-41: (1) structural properties and (2) surface chemistry. Transmission electron microscopy (TEM), X-ray diffraction (XRD) and nitrogen adsorption analysis are the three independent techniques required to obtain reliable characteristics of the porous hexagonal structures. TEM image from Figure 1.7(A) clearly shows the honeycomb structure of MCM-41 resulted from the hexagonal packing of unidimensional cylindrical pores.¹² Also, the ordered hexagonal array of parallel silica tubes could result in typical XRD patterns from $2\theta = 2^\circ$ to 5° . The reflections can be indexed assuming a hexagonal unit cell as (100), (110), (200), (210) and (300) as shown in Fig 1.7(B); and it is known that mesoporous MCM-41 is amorphous from the XRD patterns at high angles. In addition, adsorption isotherms could be used to determine the surface area and to characterize the pore-size distribution in cylindrical pores. The most common method for analyzing pore-size distribution in mesoporous range (2-50 nm)¹² is described as Barrett-Joyner-Halenda (BJH) method.

The difference between the lattice parameter ($a=2d_{(100)}/\sqrt{3}$) attained from X-ray diffraction and pore size determined by nitrogen adsorption analysis, the wall thickness of MCM-41 could be obtained. The surface properties of the walls normally could be examined by solid-state NMR spectroscopy and Fourier transform infrared (FTIR) spectroscopy. Solid state ^{29}Si -NMR spectroscopy is a very powerful tool to characterize the local chemical environment of silicon and the degree of condensation of Si-OH groups in mesoporous organosilica materials. Besides, FTIR is applied to measure the hydrophobic or hydrophilic properties of surfaces after modified with polar or unpolar molecules on surface.

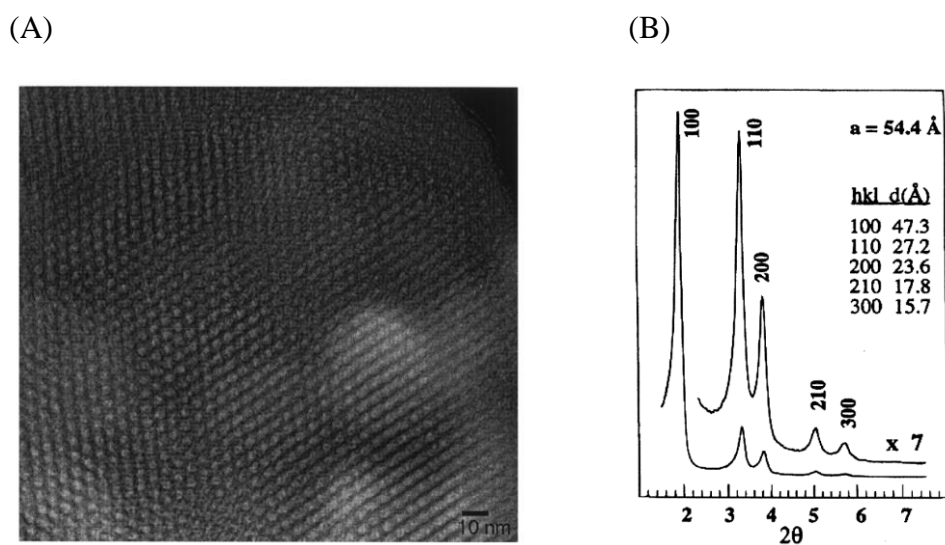


Figure 1.7 (A) Transmission electron micrograph of MCM-41 with 4 nm size pores. (B)

X-ray diffraction pattern of calcined MCM-41.¹²

Formation Mechanism

Generally, M41S family is synthesized by the combination of appropriate amounts of inorganic silica source (e.g. tetraethylorthosilicate, TEOS) and organic alkyltrimethylammonium halide surfactant (e.g. cetyltrimethylammonium bromide, CTAB) under base water solution. The formation of the organic-inorganic composite is based on electrostatic interactions between the positively charged head groups of the surfactants and negatively charged silicate species which condense into a solid, continuous network.

The basic concept of MCM-41 formation is based on the self-assembled surfactant template route as described in Figure 1.8¹³. Surfactants form micelles in the solution. At high concentration of surfactant micelles, hexagonal array of cylindrical micelles is piled up with the polar groups of the surfactants to the outside as light grey color shown in Figure 1.8¹³, and then the silicate species occupy the spaces between the cylinders depicted as dark grey color. Finally, removal of surfactant through calcinations produced hollow and porous silica network. The whole formation process is called the “liquid crystal templating” (LCT) mechanism suggested by the Mobil researchers, which proposes two main pathways for the formation of MCM-41 as described in Figure 1.8. Two mechanistic pathways in which either the liquid –crystal phase is intact before adding the silicate species (pathway1), or the inorganic silicates mediate the

ordering of silicate-enclosed surfactant micelles into hexagonal arrangement (pathway2).

The different reaction pathways are the results from surfactant properties, surfactant concentration in water and the presence of other ions.

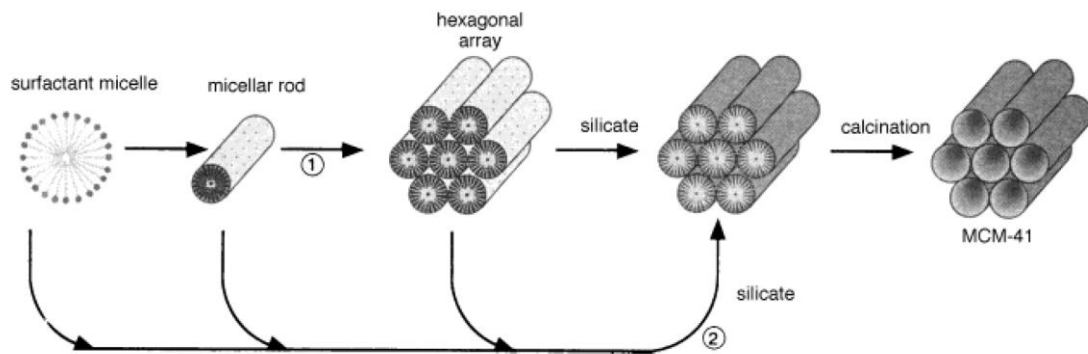


Figure 1.8 Two pathways for the LCT mechanism.¹³

1.3 Mesoporous Silica Nanoparticles (MSN) in Biomedical Applications

Mesoporous silica nanoparticles have drawn great attention in the past decade in the biomedical field for its highly unusual properties, including extremely high surface area in excess of $1000 \text{ m}^2\text{g}^{-1}$, tunable and uniform pore size of 1.5 - 10 nm, large pore volume, high biocompatibility and ease of surface functionalization. Through appropriate surface modification and nanoparticle design, these mesoporous silica materials could be applied for bio-imaging, controlled drug delivery, bio-sensing, and cell tracing.¹⁴

Bio-imaging

MSN could be used as a platform for optical imaging and magnetic resonance imaging (MRI) since it has high surface area and large pore volume which could provide the base for multiple imaging molecules.

Our group reported a magnetic-optical bi-functional MSN (Mag-Dye@ MSN) which simultaneously possess both fluorescence probe (FITC) and MRI probe (Fe_3O_4) and could be internalized by rat bone marrow stromal cells (rMSCs) as depicted in Figure 1.9.¹⁵ This report was the first to directly inject MSN into mice and to visualize the localization by MRI. From the T_2 -weighted MR images, Mag-Dye@MSN tended to accumulate in the mouse liver, kidneys, and spleen, especially in the liver and spleen

indicated by a longer recover time of signal-to-noise ratio (SNR). And the results also revealed that SNR in liver recovered after 90 days, thus Mag-Dye@MSN was demonstrated to be a potential candidate for long term liver and spleen MRI tracking. The studies of multi-functional Mag-Dye@MSN with fluorescent, magnetic and porous properties provided basic information for applying the MSN as diagnostic reagents.

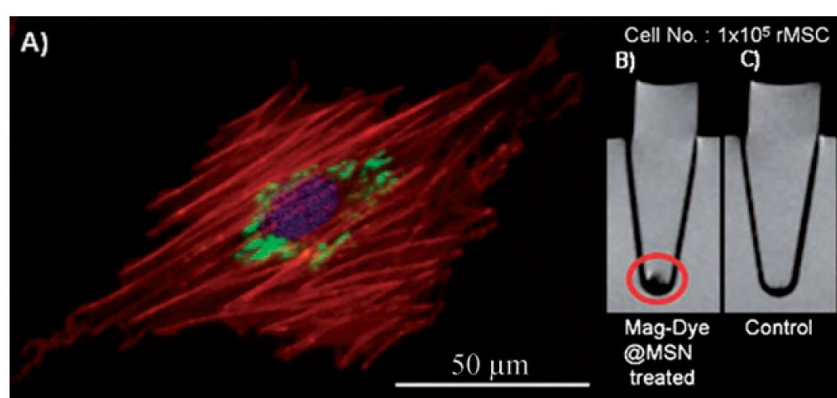


Figure 1.9 (A) Merged confocal image of rMSCs incubated with Mag-Dye@MSN for 1 hour. The cytoskeleton was stained with rhodamine phalloidin (red) and the cell nucleus with DAPI (blue). The T2-weighted MR images of: (B) labeled rMSCs after treatment with Mag-Dye@MSN for 1 h, and (C) unlabeled rMSCs.¹⁵

Bio-sensing and Cell Tracing

Because of the versatile surface chemistry and small particle size, MSN are believed to have great potential for biosensing applications. MSN with high porosity allows for the encapsulation or immobilization of large quantity of sensing molecules per particle to increase detection efficiency. Besides, MSN could be used as a

fluorescence cell tag since the mesopores offer great protection for embedded fluorophores from enzyme digestion and fluorescent cell-quenching and thus are good for long term cell tracking. Also, MSN functionalized with cell-recognition compounds could result in efficient specific targeting.

Professor Martínez and co-workers reported an anion sensor based on MSN grafted with aminomethylantracene groups since amino groups are the well-known anion coordination sites, and the anthracene moiety could be served as the signaling subunit.¹⁶ The interaction between targeted adenosine 5'-triphosphate (ATP) anions and amino receptors would result in quenching of the anthracene emission intensity denoted as the decrease in relative emission intensity ($I_{\text{receptor} + \text{ATP}}/I_{\text{receptor}}$ at $\lambda_{\text{em}} = 420 \text{ nm}$). The bulkiness of grafted amines plus the restricted ATP anion binding cavities resulted from the mesopore structures led to the stronger ATP-binding ability of MSN, compared to analogous molecular (aminoanthracene)-based receptor and silica fume matrix-based materials instead of MSN as shown in Figure 1.10. Furthermore, the material responded in different degrees to ATP, ADP (adenosine 5'-diphosphate) and AMP (adenosine 5'-monophosphate) due to the steric restrictions provided by the pore sizes of MSN. ATP was able to quench the fluorescence of the grafted material to the larger degree compared to the other two species; and small anions such chloride, bromide and phosphate didn't respond to the receptor significantly.

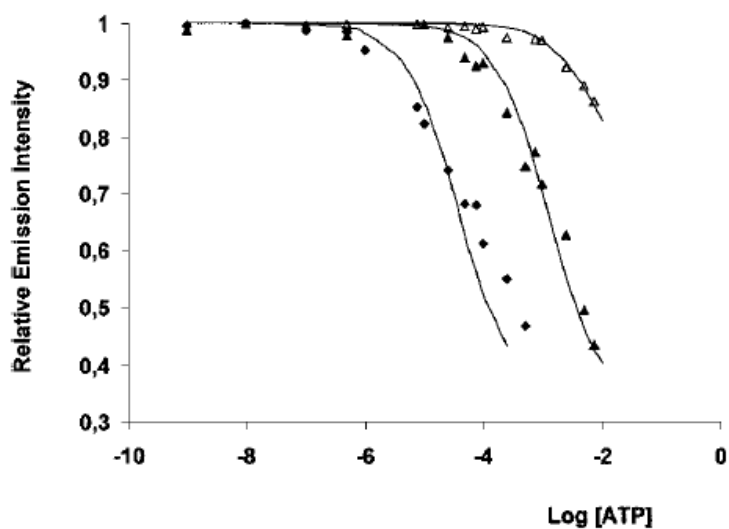


Figure 1.10 Fluorometric titration curves: relative fluorescence emission ($\lambda_{\text{ex}} = 370 \text{ nm}$, $\lambda_{\text{em}} = 420 \text{ nm}$) for analogous molecular (aminoanthracene)-based receptor (Δ), MSN-based sensor (\blacklozenge) and fumed silica-based sensor (\blacktriangle) in the presence of increasing amounts of ATP anion.¹⁶

Our group demonstrated the green light emitting fluorescein dye functionalized mesoporous silica nanoparticles (FITC-MSN) with great cell labeling efficiency.¹⁷ FITC-MSN with sizes around 110 nm could be internalized into 3T3-L1 fibroblast cells and to accumulate in cytoplasm as shown in Figure 1.11. Besides, the FITC-MSN exhibited no apparent cytotoxicity on the fibroblast cells. And the cellular internalization mechanism appears to be generic for other cell types. Thus, mesoporous silica nanoparticles are promising for further studies in biomedical applications.

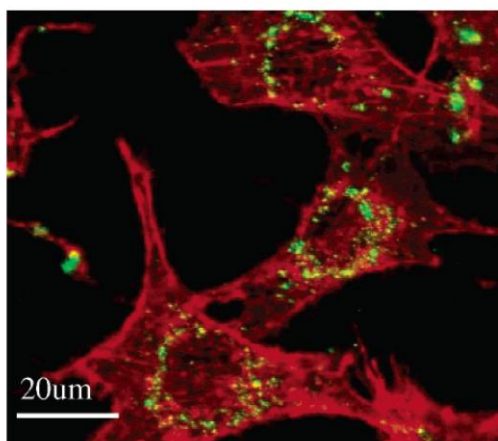


Figure 1.11 Confocal images of FITC-MSN (green) internalized by 3T3-L1 cells; cell skeleton was stained with rhodamine phalloidin dye (red).¹⁷

Controlled Drug Delivery

MSNs are assumed as convenient reservoirs for drugs and biomolecules since it possess porous property. And by using different kinds of pore-blocking caps and various stimuli-responsive strategies, several MSN-based controlled-release systems have been developed.

Professor C.-S. Yang and his team demonstrated a pH-responsive controllable oral drug delivery system by incorporating positive charges (trimethyl- ammonium, TA) into the framework of MSN (MSN-TA), and negative-charge carrying drugs, sulfasalazine, could be efficiently adsorbed inside the nanochannels by electrostatic attraction under acidic environments as depicted in Figure 1.12.¹⁸ At neutral pH value, the sustained drug release happened due to the deprotonation of surface silanol groups

which resulted in strong repulsion between negatively-charged drugs and deprotonated silanol groups. MSN-TA is believed as an efficient nanovehicle for pH-dependent loading and controlled release of anionic drugs for oral drug delivery system especially at intestine since the pH value of intestinal fluid is about 7.4.; and MSN-TA system further possess the advantage of trapping loaded drugs when passing through stomach's acid environment and starting to release drugs only in neutral intestine.

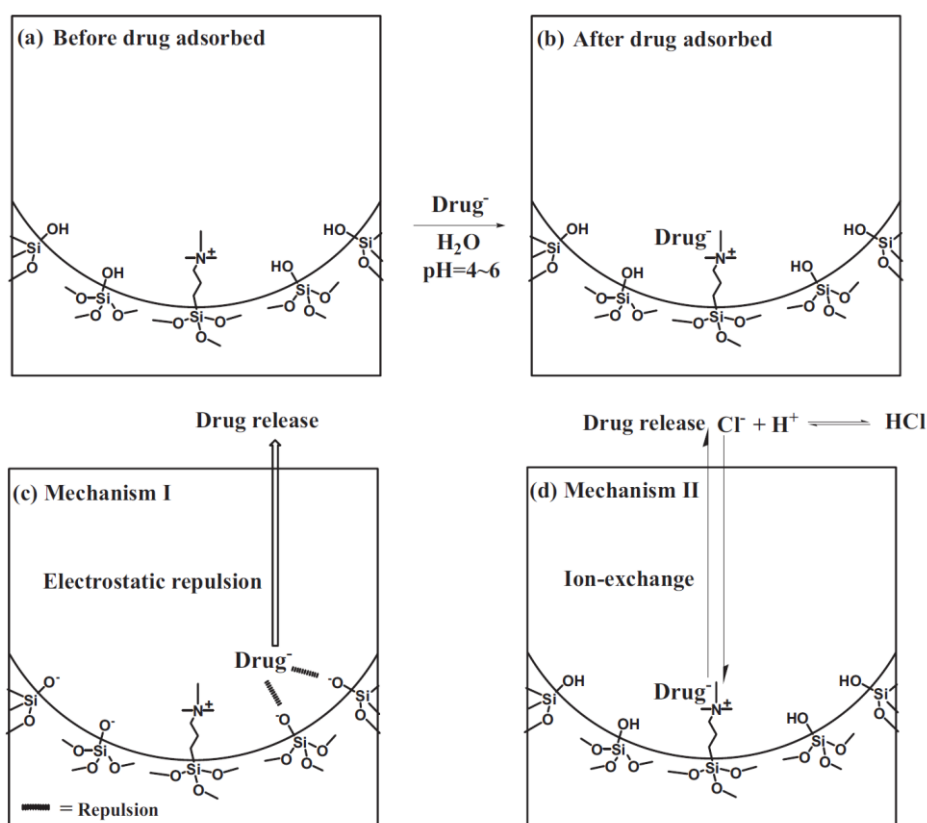


Figure 1.12 Schematic model of the sustained-release mechanism of MSN-TA loaded with anionic drugs. (a) Before drug adsorbed, (b) after drug adsorbed, (c) drugs released by electrostatic repulsion under neutral environment, and (d) drugs released by increasing ionic strength.¹⁸

Professor Victor S.-Y. Lin and his group used a gold nanoparticle-capped mesoporous silica nanosphere (AuNPs-MSN) for photoinduced intracellular controlled release of an anticancer drug, paclitaxel, in human cells as shown in Figure 1.13.¹⁹ The capping mechanism is based on the electrostatic interaction between positively charged AuNPs and negatively charged MSN materials. Upon UV irradiation, the photolabile linker covalently bonded on the AuNPs would be cleaved, altering the surface charge of AuNPs from positive to negative as the thioundecyltetraethyleneglycolcarboxylate (TUEC)-functionalized AuNPs forms. The charge repulsion between negatively charged MSN and AuNPs would uncap the mesopores and release anticancer drugs. The system was treated with paclitaxel which could be loaded inside the mesopores without undesired leaching out with AuNPs capping. Furthermore, the controlled release property of AuNPs-MSN was simply achieved by low-power photoirradiation.

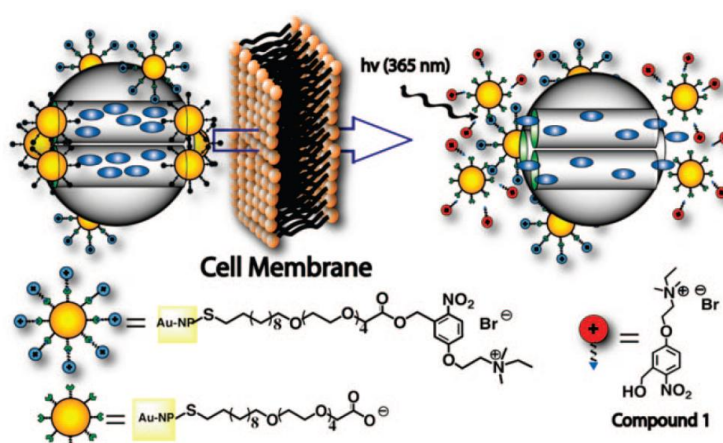


Figure 1.13 Schematic representation of the photoinduced intracellular controlled release of AuNPs-MSN carrying anticancer drug.¹⁹

Chapter Two Gadolinium-functionalized Mesoporous Silica

Nanoparticles as Magnetic Resonance Imaging Contrast Agents

2.1 Introduction

2.1.1 Biomedical Imaging Modalities

Multiple imaging modalities are available for biomedical and small-animal molecular imaging which are vital for disease diagnosis, such as cancer and neurodegenerative diseases, and could provide biological information and functions at preclinical stages.²⁰⁻²¹ Representative imaging platforms includes magnetic resonance imaging (MRI), positron emission tomography (PET), computed X-ray tomography (CT), and optical imaging as listed in Table 2.1.

Table 2.1 Comparison of several imaging modalities.²²

imaging technique	source of imaging	spatial resolution	tissue penetrating depth	sensitivity ^a	types of probe
MRI	radiowave	25 – 100 μm	no limit	mM to μM	Gd^{3+} , Fe_3O_4
PET	γ -ray	1 -2 mm	no limit	pM	^{18}F , ^{11}C , ^{13}N , ^{15}O , ^{124}I , ^{64}Cu
CT	X-ray	50 – 200 μm	no limit	not well characterized	iodine, barium sulfate
Optical imaging	visible light or near-infrared (NIR) light	in vivo: 2-3 mm; in vitro: sub- μm	< 1 cm	nM to pM	organic dye, quantum dots

^a Sensitivity of detecting probe is relative to background

Magnetic Resonance Imaging (MRI)

Based on the interaction of protons with the surrounding molecules of tissues, MRI is now one of the most powerful and non-invasive diagnosis tools in medical field. Since MRI offers higher spatial resolution and is capable to obtain physiological and anatomical information simultaneously, it could be used for cell trafficking and living organisms imaging.

Positron Emission Tomography (PET)

PET is a commonly used tomographic nuclear imaging tool due to its relatively high sensitivity. Biologically active molecules labeled with positron- emitting radionuclides, such as ^{15}O , ^{13}N , ^{11}C , and ^{18}F , can be introduced into the subject of interest, and the high-energy γ -rays emitted from the subject are recorded by PET. The distribution and concentration of the injected molecules could be used to obtain PET images by analyzing the decay of emitted γ -rays. The widespread use of PET is limited by the high costs of cyclotrons needed for producing short-lived radionuclides for scanning, safety considerations generated by the radiation exposure and relatively low spatial resolution.

Computed X-ray Tomography (CT)

Computed tomography (CT) images are obtained when tissues differentially absorb X-ray as they pass through the body. CT is a noninvasive technique for *in vivo* imaging and is a three-dimensional tomography as MRI, but its use is limited by relatively low target sensitivity and poor soft tissue contrast.

Optical Imaging

Among all of the modalities in biomedical imaging, optical imaging has been a versatile and ease of use approach due to the availability of numerous imaging probes, such as fluorescence dye and quantum dots, avoidance of radiation exposure, and relatively low cost of instrumentation. However, its image information is surface-weighted which implies targets closer to the surface appear brighter compared to those in the deeper structure, and it usually suffers from poor signal-to-noise ratio because of the tissue autofluorescence. Recently, near-infrared contrast agents are used for *in vivo* optical imaging to minimize intrinsic background interference.²⁴

2.1.2 Introduction of Magnetic Resonance Imaging (MRI)

Brief Introduction of Theory

MRI is a commonly used diagnostic tool in modern clinical medicine for its high spatial resolution, non-invasiveness, avoidance of radiation and superb soft tissue contrast. The basic principle of MRI is based on nuclear magnetic resonance (NMR), mainly on the relaxation of hydrogen proton spins under magnetic field. When a strong magnetic force acts on the nucleus of protons and tries to alter the orientation of their rotational axes, the proton spins begins to wobble, a process called precession, and align either parallel or anti-parallel.^{21, 25} During their alignment, the spins precess under a specific frequency ω_0 which is called Larmour frequency as depicted in Figure 2.1 (A).²¹ While the spin system relaxes and settles into a stable state, longitudinal magnetization (M_z) is building up in the z direction. When a resonance frequency in the radio-frequency (RF) range is introduced to the stable nuclei system which is known as excitation of the spin system, the magnetization rotates into the xy- plane called transverse magnetization (M_{xy}) as shown in Figure 2.1 (B). After the removal of the RF pulse, the excited nucleus return to the stable, lower-energy state by reducing transverse magnetization due to two independent processes, named as T_1 relaxation and T_2 relaxation, respectively.

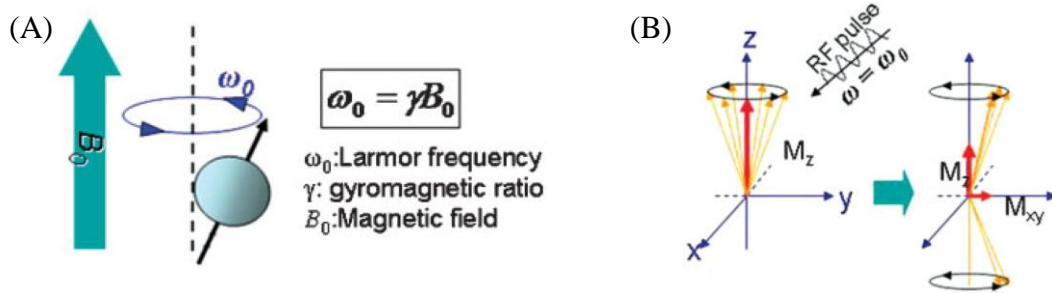


Figure 2.1 (A) Spins align to magnetic field B_0 and precess under Larmor frequency ω_0 .

(B) Magnetization of spins change after introducing RF pulse.²¹

T₁ relaxation (Longitudinal or spin-lattice relaxation): As transverse magnetization decays, the magnetic moments gradually realign with the z-axis of the main magnetic field B_0 . The process of M_z regrowth is known as T_1 relaxation or longitudinal relaxation as shown in Figure 2.2 (A).²⁵ During the relaxation process, M_z exponentially rises to the net magnetization (M_0) and the value of M_z at time t is expressed as $M_z(t) = M_0(1 - e^{-t/T_1})$. T_1 represents the time needed for the intensity recovery of M_z to 67% of M_0 as denoted in Figure 2.2 (B).²¹ Nuclei dissipate the excess energy to the surrounding lattice for returning to the ground state, so the T_1 relaxation is also called spin-lattice relaxation.

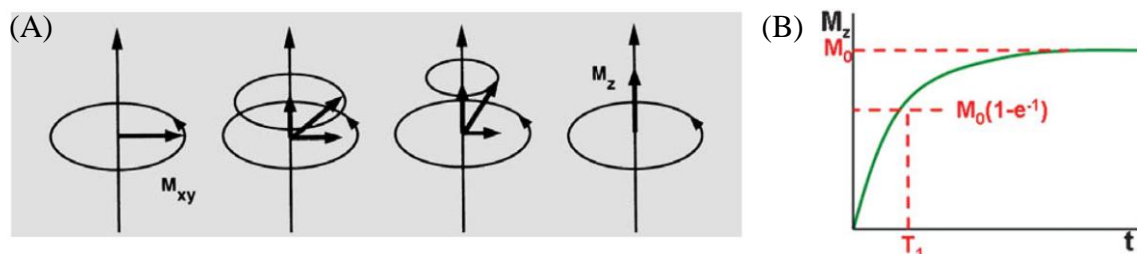


Figure 2.2 (A) Schematic representation of T_1 relaxation.²⁵ (B) Plot of M_z versus time

after RF pulse.²¹

T₂ relaxation (Transverse or spin-spin relaxation): T₂ relaxation known as transverse relaxation is due to the decay of transverse magnetization resulted from dephasing, the process spin loses phase coherence as depicted in Figure 2.3 (A).²⁵ The signal of M_{xy} exponentially decreases to zero due to the lost of coherence in the transverse plane. The value of M_{xy} at time t is expressed as $M_{xy}(t) = M_0 (e^{-t/T_2})$ and T₂ is the time where M_{xy} decays to 37% of its initial value as shown in Figure 2.3 (B).²¹ Spins in the transverse relaxation process exchange energy with each other instead of dissipating the energy to surroundings, thus T₂ relaxation is also known as spin-spin relaxation.

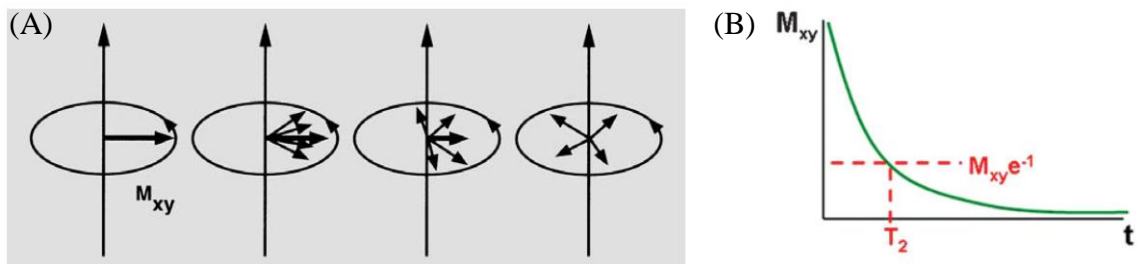


Figure 2.3 (A) Schematic representation of T₂ relaxation.²⁵ (B) Plot of M_{xy} versus time after RF pulse.²¹

Classification of MRI contrast agents

The development of a new class of pharmacological products, called contrast agents, has been prompted for enhancing the contrast with background tissues in MRI imaging.²⁶ All contrast agents shorten the relaxation time of nearby water molecules,

which means they shorten both T_1 and T_2 . Contrast agents increase both $1/T_1$ and $1/T_2$ to varying degrees by their nature and applied pulse sequences; pulse sequence aiming at changing $1/T_1$ is referred as T_1 -weighted and the opposite is T_2 -weighted scans. MRI agents have been classified into two groups as T_1 and T_2 contrast agents.

T₁ contrast agents: The first category is referred as T_1 agents, which alter $1/T_1$ of tissue more than $1/T_2$ using T_1 - weighted sequences and results in the increase in signal intensity; these are positive contrast agents.²⁷⁻²⁸ Most common T_1 contrast agents are paramagnetic ions, transition and lanthanide metal ions with a large number of unpaired electrons, such as Gd^{3+} , Mn^{2+} and Fe^{3+} as shown in Figure 2.4.²¹ Most T_1 contrast agents are gadolinium-based agents since Gd^{3+} possesses seven unpaired electrons with a large magnetic moment.²¹ T_1 contrast agents are usually evaluated based on the longitudinal relaxivity value, r_1 , which refers to the slope plotting concentration of contrast agent (mM) versus the relaxation rate ($1/T_1$).^{27, 29} And the contrast is enhanced more as the relaxivity is higher.

	Ion	Configuration		Magnetic moment
		3d	4f	
Transition metal ion	$^{24}Cr^{3+}$	↑ ↑ ↑ — —		3.88
	$^{25}Mn^{2+}$	↑ ↑ ↑ ↑ ↑		5.92
	$^{26}Fe^{3+}$	↑ ↑ ↑ ↑ ↑		5.92
	$^{29}Cu^{2+}$	↑ ↓ ↑ ↓ ↑ ↑		1.73
lanthanide metal ion	$^{63}Eu^{3+}$		↑ ↓ ↑ ↑ ↑ ↑ ↑ ↑	3.4
	$^{64}Gd^{3+}$		↑ ↑ ↑ ↑ ↑ ↑ ↑	7.94
	$^{66}Dy^{3+}$		↑ ↓ ↑ ↓ ↑ ↑ ↑ ↑	10.65

Figure 2.4 Electron configuration and magnetic moment of metal ions.²¹

T₂ contrast agents: T₂ agents increase 1/T₂ of tissues to a much greater extent and cause a reduction in signal intensity; hence, these are negative contrast agents.²⁷⁻²⁸ Commercially, T₂ contrast agents based on iron oxide nanoparticles are the most representative ones. However, their extensive applications are limited by its signal-decreasing effect. The dark signals enhanced by T₂ contrast agents could be confused with other pathogenic conditions such as bleeding and is subject to artifacts on MR imaging; thus, T₂ contrast agent is less reliable than T₁ contrast agent.²¹ The transverse relaxivity value, r₂, refers to the amount of increase in 1/T₂ per millimolar (mM) of T₂ contrast agent, which is the slope of plotting relaxation rate (1/T₂) versus the concentration of contrast agent.²⁷

Gadolinium-based T₁ contrast agents

More than 10 million of MRI studies are performed with gadolinium complexes since it has great image-enhancing capability. Although some manganese- and iron-based contrast agents are approved for clinical use, commercial contrast agents have been adopted by gadolinium-based complexes owing to its long electronic relaxation time and highly paramagnetic property.^{26,28} There are several parameters that influence the relaxivity of gadolinium-based contrast agents as depicted in Figure 2.5.²⁶ Strategies for enhancing the relaxivity of a Gd contrast agent include increasing the

number of inner-sphere water molecule (q), optimally shortening water residence time (τ_m), and slow tumbling rate ($1/\tau_r$) or increase rotational correlation time (τ_R).^{26, 29} And rotation is perhaps the most critical variable among all the parameters.²⁷

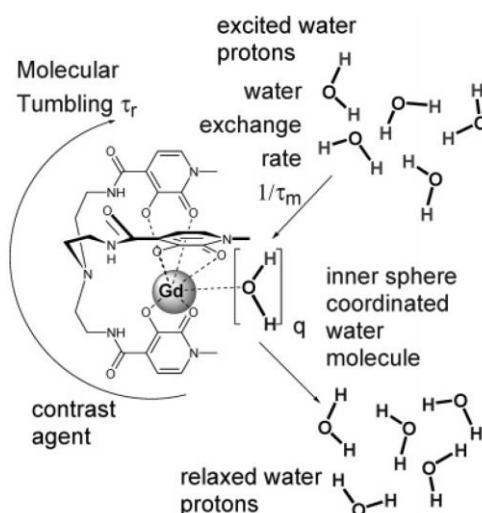


Figure 2.5 Parameters influencing relaxivity.²⁶

Recently, macromolecules and nanoparticles have been developed as platforms for the presentation of Gd^{3+} complexes with several potential advantages: 1. Relaxivity per gadolinium is enhanced by reducing the tumbling rate because of the overall molecular weight increase; 2. Macromolecules or nanoparticles could provide space for large number of Gd complexes in a confined volume, enhancing total molar relaxivity; 3. Macromolecules or nanoparticles have the potential for simultaneously incorporating targeting probes or other molecular imaging agents which are vital for further biomedical applications.³⁰

2.2 Experiments

2.2.1 Materials

All chemicals were used without further purification. Hexadecyltrimethylammonium bromide (CTAB, 99+%), fluorescein isothiocyanate isomer I (FITC, 90% pure), tetraethyl orthosilicate (TEOS, 98%), 3-aminopropyl-trimethoxysilane (APTMS, 95%), citric acid, trisodium salt dihydrate (99%), ammonium hydroxide (NH₄OH, 28-30% as NH₃), hydrofluoric acid (HF, 48-51%), and ammonium nitrate were obtained from Acros Organics. Gadolinium (III) chloride hexahydrate (99.9%) was obtained from Alfa Aesar. Nitric acid (HNO₃, 65%) and dimethyl sulphoxide (99.5%) were purchased from Panreac. Trypan blue solution (0.4%) was purchased from Sigma.

2.2.2 Synthesis of Gd(OH)₃@MSN

The gadolinium citrate stock solution was first prepared by mixing 0.1mL of 1M aqueous GdCl₃·6H₂O and 0.2mL of 1M aqueous sodium citrate, and precipitate formed immediately which redissolved when 0.3mL of 15.52M NH₄OH was added forming a clear stock solution. In a typical synthetic procedure for gadolinium (III)-incorporated mesoporous silica nanoparticles, 1.6 mmol of hexadecyltrimethylammonium bromide, CTAB, was dissolved in 300g of 0.17M NH₄OH and 5mL of 0.226M TEOS ethanolic solution was added with stirring. The

resulting solution was vigorously stirred at 40°C for 5 hours. Then, 5mL of 1.13M TEOS ethanolic solution was added. After 1 minute, 600µL gadolinium stock solution was added sequentially to the reaction solution under continuously stirring and the solution was allowed to stir for another 1 hour. The solution was then aged at 40°C for 24 hours. Adding the 1.13M TEOS ethanolic solution and gadolinium stock solution in opposite order, one could obtain Gd(OH)₃@MSN materials of different morphology. Besides, by adding 300µL, 600µL, 1200µL, and 2400µL of Gd stock solution in the synthesis procedure could result in various Gd loaded mesoporous silica nanoparticles. The as-synthesized Gd(OH)₃@MSN product was collected by centrifugation at 15000rpm for 20 minutes and washed and redispersed in 50mL of ethanol 2 times. To avoid Gd(OH)₃ dissolution which might occur under strongly acidic condition, the surfactants were extracted by a fast and effective ion exchange method, where as-synthesized Gd(OH)₃@MSN was transferred to 50mL of ethanol solution containing 1g of NH₄NO₃ and kept under 60°C for 1 hour. In order to completely remove the surfactants, the extraction step was repeated three times with fresh 1g of NH₄OH each time. After the extraction, the Gd(OH)₃@MSN were washed with ethanol and nanopure water 5 and 2 times, respectively, and then redispersed and stored in 99.5% ethanol.

2.2.3 Synthesis of Gd(OH)₃-FITC@MSN

The preconjugated N-1-(3-trimethoxy-silylpropyl)-N-fluoresceyl thiourea (APTMS-FITC) was prepared by stirring 5 μ L of APTMS and 5mL of 0.51mM FITC ethanolic solution in the dark at room temperature for 24 hours. The citrate protected Gd(OH)₃ stock solution was prepared by mixing 0.1mL of 1M aqueous GdCl₃·6H₂O and 0.2mL of 1M aqueous sodium citrate, and precipitate formed immediately which redissolved when 0.3mL of 15.52M NH₄OH was added forming a clear stock solution. In a synthetic procedure for Gd(OH)₃-FITC@MSN, 1.6 mmol of CTAB, was dissolved in 300g of 0.17M NH₄OH and 5mL of 0.226M TEOS ethanolic solution was added with stirring. The resulting solution was vigorously stirred at 40°C for 5 hours. Then, 5mL of 1.13M TEOS ethanolic solution was added. After 1 minute, 600 μ L gadolinium stock solution and 5mL APTMS-FITC were added sequentially to the reaction solution under continuously stirring and the solution was allowed to stir for another 1 hour. The solution was then aged at 40°C for 24 hours. The as-synthesized Gd(OH)₃-FITC@MSN product was collected by centrifugation at 15000rpm for 20 minutes and washed and redispersed in 50mL of ethanol 2 times. The surfactants were extracted by a fast and effective ion exchange method, where as-synthesized Gd(OH)₃-FITC@MSN was transferred to 50mL of ethanol solution containing 1g of NH₄NO₃ and kept under 60°C for 1 hour. In order to completely remove the surfactants, the extraction step was

repeated three times with fresh 1g of NH_4OH each time. After the extraction, the $\text{Gd}(\text{OH})_3\text{-FITC@MSN}$ were washed with ethanol and nanopure water 5 and 2 times, respectively, and then redispersed and stored in 99.5% ethanol. The solid samples for X-ray diffraction (XRD) and N_2 adsorption-desorption isotherms were obtained by centrifugation followed by drying at 60 °C for 24 hours.

2.2.4 Cell culture and Assays

Cell Uptake (NIH3T3 Mouse Fibroblast Cell & Mouse Embryonic Stem Cell)

NIH3T3 Mouse Fibroblast Cell: 2.5×10^5 NIH-3T3 mouse fibroblast cells were seeded in high glucose Dulbecco's modified Eagle's medium (DMEM) supplemented with 10% fetal bovine serum (FBS), 10% penicillin, and 10% streptomycin per well in a 6 well plate. The culture was kept at 37°C in an atmosphere of 5% CO₂ and 95% air. After 24 hours of cell attachment, the cells were incubated with 0µg, 50µg, 100 µg, 200µg and 400µg of Gd(OH)₃-FITC@MSN particles in 2mL serum-free medium for 4 hours, and then washed with serum-free medium twice. And the cell uptake was observed by fluorescence microscopy or analyzed by other methods.

Mouse Embryonic Stem Cell: Mouse embryonic stem cells were seeded at 10^6 cells per well in a 6 well plate. Then the cells were incubated with 0µg, 50µg, 100µg, 200µg, 400µg and 800µg of Gd(OH)₃-FITC@MSN particles in 2mL per cell in culture medium at 37°C in an atmosphere of 5% CO₂ and 95% air for 24 hours. It was then collected in the falcon tube and washed with phosphate-buffered saline (PBS solution: 137 mM NaCl, 2.68 mM KCl, 10 mM Na₂HPO₄, 1.76mM KH₂PO₄, pH 7.4). Cell counting for further MRI experiment was done by well suspending the cells to separate the pellets to single cell and the mixture was filtered through a 40µm filter. For DAPI staining, 10^5 cells were fixed with 4% paraformaldehyde and rinsed twice with PBS.

Then, the nucleus was stained with DAPI for 15 minutes and mounted by prolong gold.

MTT Assay

5×10^4 cells of NIH-3T3 mouse fibroblast cells were seeded in high glucose DMEM supplemented with 10% FBS in a 24 well plate. The culture was kept at 37°C in an atmosphere of 5% CO₂ and 95% air. After 24 hours of cell attachment, the cells were incubated with 0µg, 20µg, 50µg, 100µg, 150µg and 200µg of Gd(OH)₃-FITC@MSN particles in 0.5 mL serum-free medium for 4 hours. 50µL of serum-free medium and 450µL of 3-(4,5-Dimethylthiazol-2-yl)-2,5-diphenyl- tetrazolium bromide (MTT) PBS solution (5mg/mL) were added followed by further incubation for 12 hours. Then, 400µL of dimethyl sulphoxide (DMSO) was added to dissolve purple formazan crystals which formed from the reduction of MTT in the mitochondria of living cells. After that, 100µL of the above solution was placed in a 96-well plate, and the absorbance at 570nm was measured by ELISA reader from Bio-Rad.

Flow Cytometry for Cell Labeling & Effect of Dosage

2.5×10^5 cells of NIH3T3 mouse fibroblast cells per well were seeded in a 6-well plate and were allowed to attach for 24 hours. In order to determine the extent of Gd(OH)₃-FITC@MSN uptake, the cells were incubated with Gd(OH)₃-FITC@MSN of

various concentration from 0 μ g to 200 μ g in 2mL per cell in serum-free medium for 4 hours. Treated cells were then washed with PBS twice and then harvested by trypsinization. About 7.5×10^5 cells were collected and centrifuged at 3000 rpm for 5 minutes, and the cell pellets were well dispersed in 400 μ L of phosphate-buffered saline (PBS) solution. The green emitting fluorescein (FITC) dye, which was excited at 488 nm with an Argon Laser and detected at wavelength in the 510 to 540 nm range, incorporated in the Gd(OH)₃-FITC@MSN could serve as a cellular uptake indicator. Hence, fluorescence was quantitatively measured by FACSCalibur flow cytometry and CellQuest Pro software, was used to analyze the data, and the percentage of Gd(OH)₃-FITC@MSN labeled cells versus treated concentration was plotted.

Cell Preparation for MRI

After treatment with Gd(OH)₃-FITC@MSN particles, 6×10^5 viable cells were collected in a cell centrifuge tube and centrifuged at 1000-1500 rpm for 5 minutes. The supernatant was then removed and the cell pellet was resuspended in 200 μ L of PBS solution. Then 200 μ L of 1% melted agarose were added and the mixture was well resuspended with the PBS solution, followed by transferring to a home-made syringe tube without generating any bubbles. Finally seal the syringe with parafilm, stored at 4 $^{\circ}$ C, and analyzed by 4.7 T Biospec spectrometer from Bruker.

2.2.5 Physical and Chemical Characterization

Transmission Electron Microscopy (TEM)

JOEL JEM-1230 electron microscope instrument was used to take TEM images under the voltage of 100 kV. Samples were first well dispersed in ethanol at a very low concentration (0.2 mg / mL) and 10 μ L of the suspension was dropped onto a microgrid and dried at room temperature.

Powder X-ray diffraction (XRD)

XRD patterns were collected by using a PANanalytical X'Pert PRO instrument with Cu K α ($\lambda = 1.5406\text{\AA}$) radiation in the 2θ range from 0.5° to 8° . The operating voltage and current were 45kV and 40mA, respectively.

Nitrogen adsorption-desorption isotherms

N₂ adsorption-desorption isotherms were obtained from a Micromeritics ASAP 2010 apparatus. The sample was first degassed at 100°C under 10^{-3} torr for 8 hours. Data was collected at liquid N₂ temperature, -77K. Then, the surface area was calculated by Brunauer-Emmett-Teller (BET) method and the pore size distribution was analyzed by Barrett-Joyner-Halenda (BJH) method.

Inductively Coupled Plasma-Mass Spectrometry (ICP-MS)

Gadolinium amount was quantitatively measured by ICP-MS with a Perkin-Elmer Alan-6000 instrument. The calibration curve was obtained by measuring the standard metal ion solution with concentration between 10 ppb to 100 ppb. 5 mg of Gd(OH)₃-FITC@MSN samples were first dried at 60°C for 24 hours and then dissolved sequentially in 0.5 mL of HF and 1.5 mL of HNO₃ solution. The solution was finally diluted to 1/2500 for the measurement.

Dynamic Light Scattering (DLS)

Size distribution and zeta potential were determined by MALVEN Nano-ZS at room temperature. One milligram of Gd(OH)₃-FITC@MSN was dispersed in 2.5mL of nanopure water in advance. Zeta potentials measured under different pH values ranging from 3 to 9 were obtained by titrating the sample dispersion with commercial 0.1N HCl (aq) and 0.1N NaOH (aq) solution.

2.2.6 Magnetic Resonance Characterization

Relaxivities of the Nanoparticles at 0.47 T and 1.41T

0.47 T (20MHz) and 1.41 T (60MHz) Minispec spectrometer made from Bruker were used to measure longitudinal (T_1) proton relaxation by inversion recovery sequence and to obtain transverse (T_2) proton relaxation with spin-echo sequence. Gd(OH)₃-FITC@MSN samples were dissolved in nanopure water and prepared in four concentrations by serial dilution. Slopes of plots of [Gd] (mM) versus $1/T_1$ (s^{-1}) and $1/T_2$ (s^{-1}) are relaxivities, r_1 and r_2 , respectively.

Phantom Images of the Nanoparticles at 4.7 T

4.7 T Biospec spectrometer from Bruker was used to take T_1 -map and T_2 -map. T_1 -map was determined by inversion recovery sequence with FOV = 8x8 cm, ST = 1.5 mm, NEX = 2, Matrix = 256x256, T_E = 7.8 ms, and T_R = 50 ms to 6000 ms, while FOV = field of view, ST = slice thickness, NEX = number of excitation, T_E = echo time, and T_R = repetition time. Spin-echo sequence was used to obtain T_2 -map by FOV = 8x8 cm, ST = 1.5 mm, NEX = 2, Matrix = 256x256, T_R = 5000 ms, and T_E = 10 ms to 200 ms.

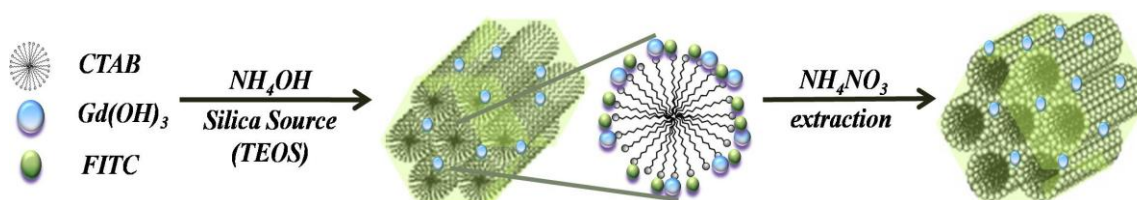
Phantom Images of Cells at 4.7T

Cells were labeled with Gd(OH)₃-FITC@MSN for 4 hours, centrifuged and

resuspended with 200 μL of PBS solution plus 200 μL of 1% melted agarose in home-made syringe tube. The tubes were analyzed by 4.7 T Biospec spectrometer from Bruker for taking cell MR images. RARE (rapid acquisition with relaxation enhancement) with variable T_R was used for T_1 mapping while MSME (multi echos multi slices) was used for T_2 mapping. And the parameters of T_1 mapping were FOV = 5x5 cm, ST = 1.5 mm, NEX = 2, Matrix = 256x256, T_E = 8.3 ms, and T_R = 70 ms to 6000 ms. On the other hand, the parameters for T_2 mapping were FOV = 5x5 cm, ST = 1.5 mm, NEX = 8, Matrix = 256x256, T_R = 8000 ms, and T_E = 10 ms to 200 ms.

2.3 Results and Discussion

High surface area, large pore volume, uniform particle size and high biocompatibility make MSN a very powerful tool platform for biomedical applications. Besides, owing to size and porous nature, MSN could serve as a great platform for enhancing the MR contrast ability of Gd-complex by slowing down the tumbling rate of gadolinium metals and by increasing the total molar relaxivity with the excess space for gadolinium metals. Hence in this work, we report a multifunctional mesoporous silica nanoparticle with gadolinium hydroxide, $Gd(OH)_3$, as active MRI contrast agent, a fluorescence dye, FITC, for optical imaging and porous property from MSN support. The synthesis of the uniform multifunctional mesoporous silica nanoparticle, $Gd(OH)_3$ -FITC@MSN, is illustrated in Scheme 2.1.

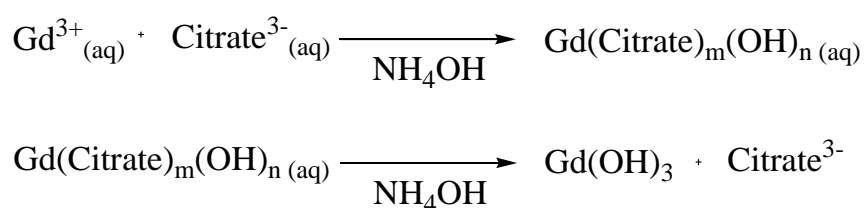


Scheme 2.1 Synthetic procedure of $Gd(OH)_3$ -FITC@MSN.

Mesoporous silica nanoparticles are synthesized by using dilute tetraethyl orthosilicate (TEOS) precursor and low surfactant concentration condition with ammonia solution as catalyst.¹¹⁻¹³ However, attempts to synthesize lanthanide doped silica under basic condition such as adding lanthanide salts to the ammonia solution during MSN synthesis, lanthanide hydroxide formed instantly and precipitated out from

the solution; consequently uniform lanthanide doped silica materials could not be obtained through simple base synthesis.³¹ Hence, it is critical to protect metal ion from forming insoluble precipitates of hydroxide before the formation of MSN. It is well known that citric acid could act as a great protecting agent for nanoparticles since it is a multidentate ligand with three of its carboxylate groups having strong affinity to metal ions;³²⁻³³ therefore, citrate is chosen to protect gadolinium (Gd) ion for synthesizing Gd-incorporated mesoporous silica nanoparticles.

Hence, FITC was attached to APTMS through a nucleophilic reaction to form FITC-APTMS. The formation of Gd(OH)₃ is depicted in the following proposed equations shown in scheme 2.2.³⁰ In the typical synthesis process of Gd(OH)₃-FITC@MSN, surfactants formed micelles in the basic solution, dilute TEOS hydrolyzed to attach to the micelles forming seeds, then preformed Gd(OH)₃, FITC-APTMS and more TEOS were added to complete the condensation.

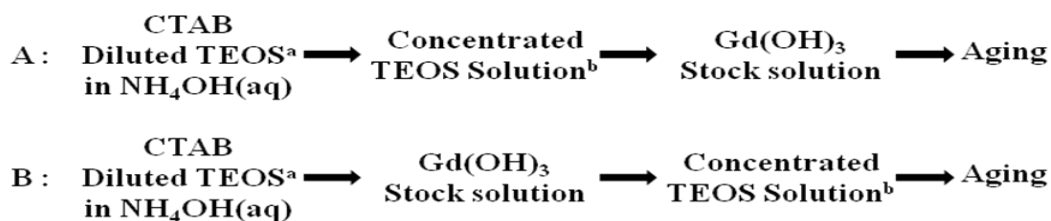


Scheme 2.2 Proposed equations of the formation of Gd(OH)₃.³⁰

Precipitate formed immediately as GdCl₃·6H₂O and sodium citrate dihydrate were mixed together, and the precipitate redissolved when concentrated ammonia was added to obtain a transparent solution containing the gadolinium citrate hydroxide

complex, $\text{Gd}(\text{Citrate})_m(\text{OH})_n$ (aq). With the presence of large excess of hydroxide provided by the ammonia solution, citrate was replaced from the coordination sites and gadolinium hydroxide, $\text{Gd}(\text{OH})_3$, formed in the stock solution. Later, the hydroxyl groups of $\text{Gd}(\text{OH})_3$ served as the condensation bridges with TEOS. Finally, the template-serving surfactant was acid extracted by ammonium nitrate.

We have employed two different methods via the adding order of concentrated TEOS and $\text{Gd}(\text{OH})_3$ stock solution as illustrated in Scheme 2.3. In process A, concentrated TEOS was added first, then one minute later, $\text{Gd}(\text{OH})_3$ stock solution was added; while in process B, concentrated TEOS was added immediately after $\text{Gd}(\text{OH})_3$ stock solution.



^aDiluted TEOS is 0.2 M TEOS / ethanol precursor

^bConcentrated TEOS solution is 0.875M TEOS / ethanol solution.

Scheme 2.3 Two different synthetic procedures for $\text{Gd}(\text{OH})_3$ @MSN.

2.3.1 Properties of Two Different Synthetic Procedures

Transmission electron microscopy (TEM) characterization: TEM images (Figure 2.6) show that the two $\text{Gd}(\text{OH})_3@ \text{MSN}$ products with different synthesizing methods have diverse morphologies.

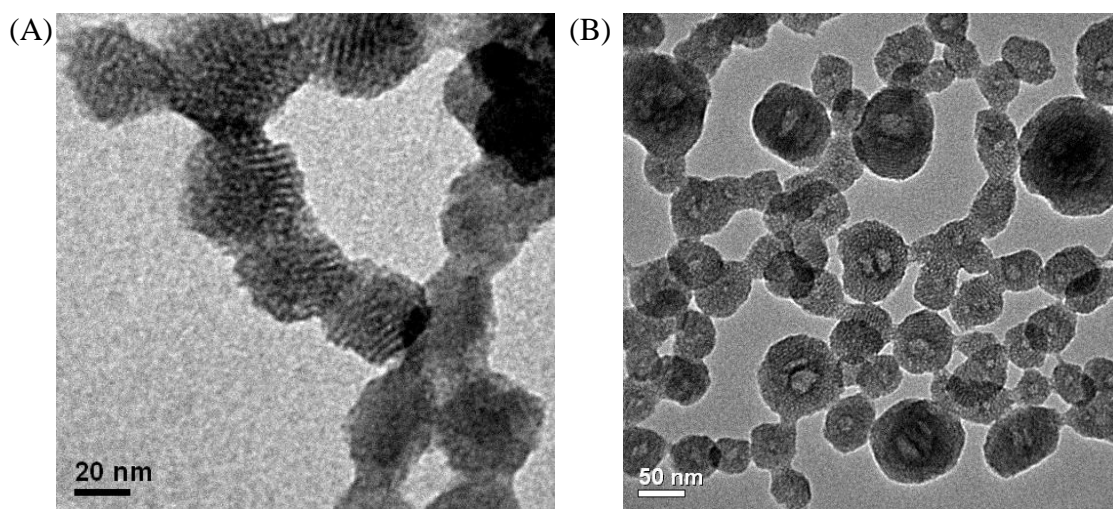


Figure 2.6 TEM images of (A) $\text{Gd}(\text{OH})_3@ \text{MSN-A}$ and (B) $\text{Gd}(\text{OH})_3@ \text{MSN-B}$.

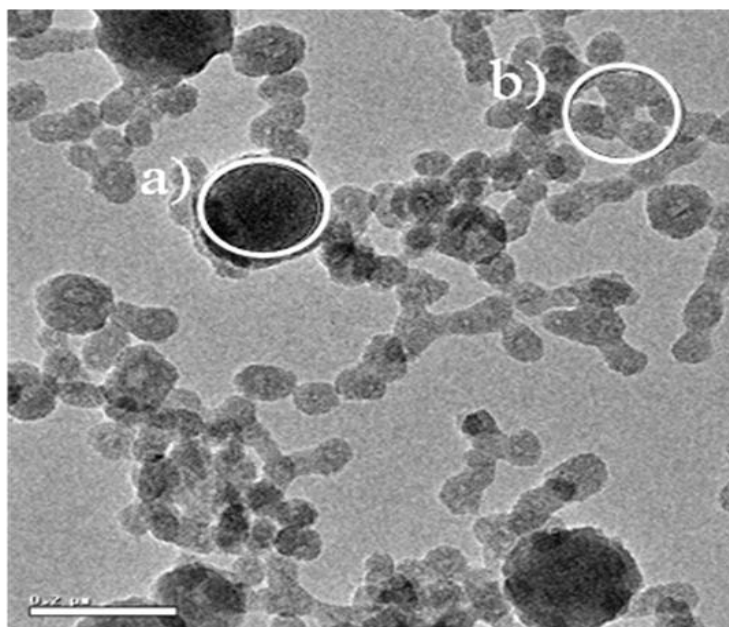
Figure 2.6 (A) in the TEM for the nanoparticles synthesized through process A, $\text{Gd}(\text{OH})_3@ \text{MSN-A}$, showing well-defined hexagonal edges and uniform porous structure with particle size around 50 nm. During the synthetic process, when low surfactant (CTAB) concentration aqueous ammonia solution and ethanol diluted TEOS precursor were mixed, the silicate / surfactant rod-like silicate micelles (SSMs) were formed. Later the concentrated TEOS was added to lead the self-assembling and deposition of SSMs which resulted in the hexagonal crystal-like mesoporous nanoparticles.³⁰ Finally, $\text{Gd}(\text{OH})_3$ stock solution was introduced to the system and Gd

was incorporated into the framework of mesoporous silica nanoparticles by condensation without affecting the hexagonal and well-ordered pore structures.

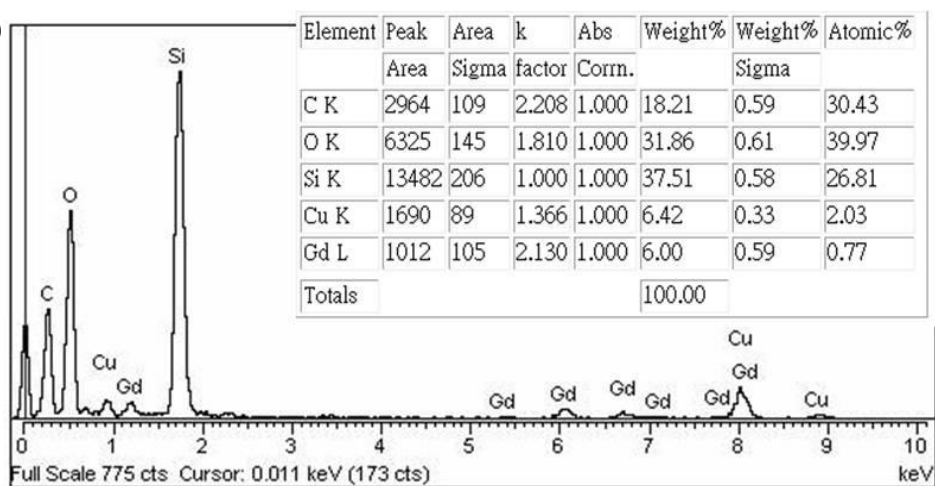
Figure 2.6 (B) is the silica nanoparticles via synthetic process B, $\text{Gd}(\text{OH})_3\text{@MSN-B}$, which displayed approximately two different structures including large aggregation complexes and hollow sphere cores with porous surroundings. The large aggregation complexes were believed to be an assembly of $\text{Gd}(\text{OH})_3$ evidenced by the results of transmission electron microscopy - energy dispersive spectrometer (TEM-EDS) mapping from Figure 2.7. We propose a plausible explanation for the formation of these two structures as the following: as the same as in process A, low surfactant (CTAB) concentration aqueous ammonia solution and ethanol diluted TEOS precursor were mixed and the SSMs were formed. Then, the addition of $\text{Gd}(\text{OH})_3$ stock solution resulted in two different morphologies. Some $\text{Gd}(\text{OH})_3$ aggregated immediately to form the aggregation complexes while the others served as seeding cores as they conjugated directly with the SSMs. Since it is well-known that OH^- could dissolve silica by weakening Si-O bonds, we believe the hollow silica cores were formed because of the basic synthesis condition offered by ammonium hydroxide which acted as the etchant for silica particles.³⁴⁻³⁵ Because silica condensation rate was fast in basic solution, it was not possible to remove all of the core silica materials by dissolving all the silanol. After adding concentrated TEOS solution, the Gd-containing SSMs cores

would self-aggregate and deposited to form the mesoporous nanoparticles with both hollow sphere cores and mesoporous structure.

(A)



(B)



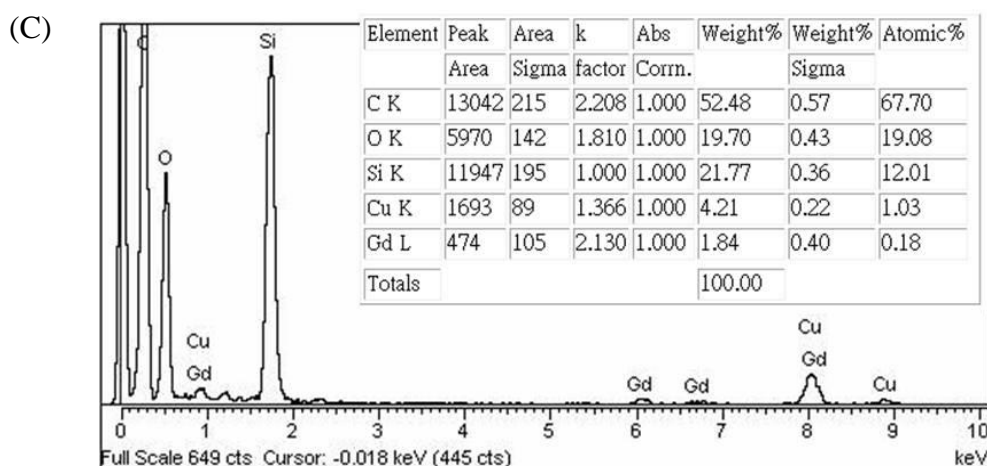


Figure 2.7 (A) TEM image of $\text{Gd}(\text{OH})_3@\text{MSN-B}$, where a) is referred to the large aggregation complex and b) represents hollow sphere cores with porous surrounding. EDS results of a) and b) are shown in (B) and (C), respectively. The scale bar is $0.2 \mu\text{m}$.

Powder X-ray diffraction (XRD) analysis: Low angle XRD patterns of extracted $\text{Gd}(\text{OH})_3@\text{MSN}$ synthesized through process A and B are shown in Figure 2.8 (A) and (B), respectively. The diffraction peaks at $2\theta = 2.2^\circ$, 3.8° and 4.4° could be indexed to typical well-ordered 2D hexagonal mesoporous characteristic reflection peaks as (100), (110) and (200). Whether $\text{Gd}(\text{OH})_3@\text{MSN}$ was synthesized through process A or B, both of the synthetic procedures could result in the well-ordered hexagonal mesopores.

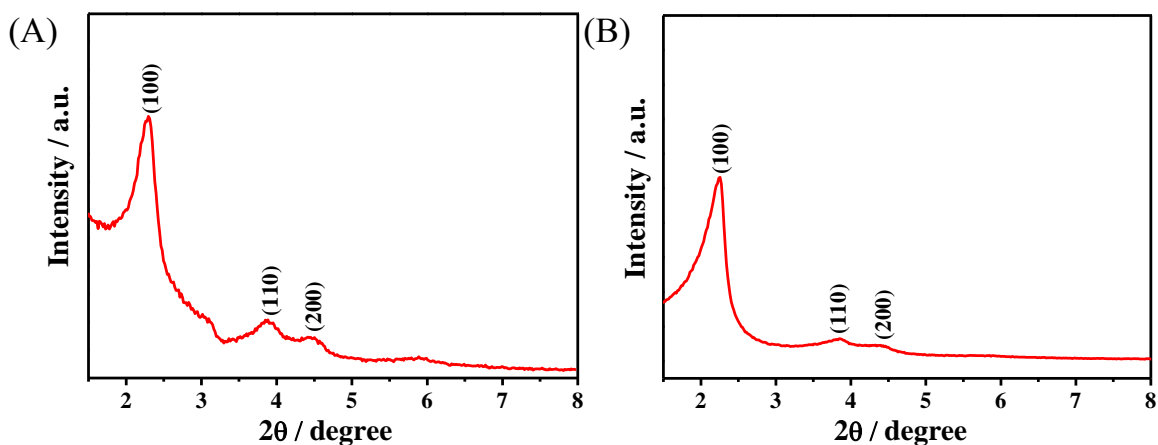


Figure 2.8 Low angle XRD patterns of surfactant-free (A) $\text{Gd}(\text{OH})_3@MSN\text{-A}$ and (B) $\text{Gd}(\text{OH})_3@MSN\text{-B}$.

Other chemical and physical characterizations: Amount of gadolinium was incorporated amount analyzed by inductively coupled plasma-mass spectrometry (ICP-MS) and hydrodynamic sizes were obtained from dynamic light scattering (DLS). Results of $\text{Gd}(\text{OH})_3@MSN\text{-A}$, B were shown in Table 2.2. $\text{Gd}(\text{OH})_3@MSNs$ with different synthetic processes possess similar Gd-incorporated amounts, near 3 % to 4 % and hydrophilic sizes about 250 nm to 350 nm.

Table 2.2 Gd-incorporated amount analyzed by ICP-MS and hydrodynamic sizes obtained from DLS of $\text{Gd}(\text{OH})_3@MSN\text{-A}$ and -B.

$\text{Gd}(\text{OH})_3@MSN$ Samples	Gd%(w.t)	Particle Size (nm)
$\text{Gd}(\text{OH})_3@MSN\text{-A}$	3.5%	282.1
$\text{Gd}(\text{OH})_3@MSN\text{-B}$	4.2%	256.1

Relaxivity measurements (0.54T), T₁- and T₂- Maps (4.7T): In this section, APTMS-FITC was added immediately after adding concentrated TEOS solution and Gd(OH)₃ stock solution in process A. However, since the addition of organic dyes doesn't affect the morphologies and relaxivities and for easier comparison, we still differentiate process A and B merely by the orders of adding concentrated TEOS and Gd(OH)₃ stock solution without noticing the adding of fluorescence dyes. Gd(OH)₃@MSN nanoparticles could be dispersed well in water and the relaxivities could be directly measured. By plotting concentration of Gd versus 1/T₁, the relaxivities r_1 of Gd(OH)₃@MSN synthesized through process A and B were found to be 12.6 mM⁻¹s⁻¹ and 13.4 mM⁻¹s⁻¹, respectively at 0.54T as shown in Figure 2.9 (A). Figure 2.9 (B) shows the relaxivities r_2 of Gd(OH)₃@MSN with synthetic processes A and B under 0.54T, which were 13.9 mM⁻¹s⁻¹ and 14.8 mM⁻¹s⁻¹, respectively. As shown in the figure, Gd(OH)₃@MSN synthesized through both procedures show greater T₁ enhancing capabilities than commercial T₁ contrast agent, MultiHance®, whose relaxivity r_1 is only 4.7 mM⁻¹s⁻¹; besides, both Gd(OH)₃@MSN-A and -B possessed significantly low r_2 / r_1 ratio compared to other nanoparticle contrast agent which indicated strong positive-contrast effects.²¹

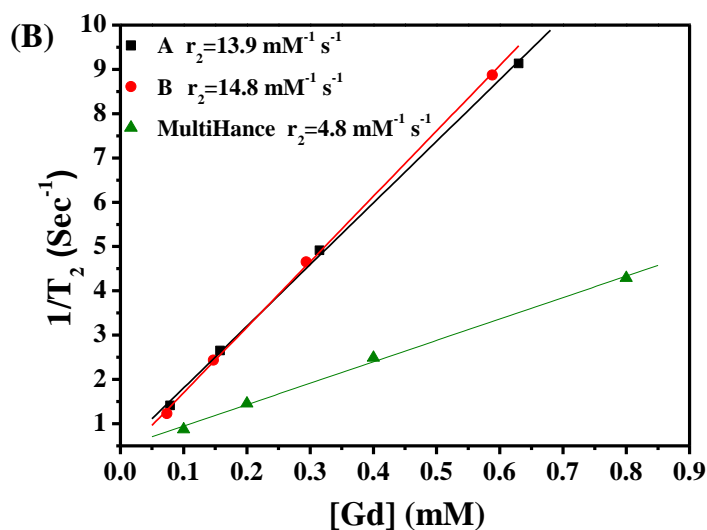
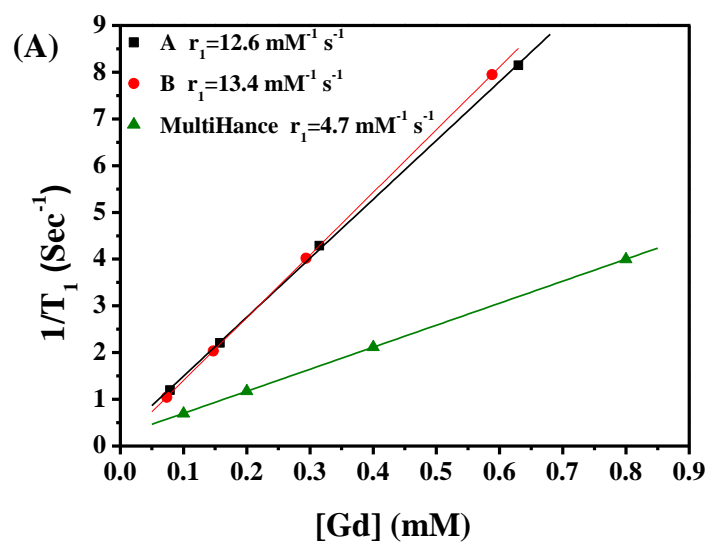


Figure 2.9 Relaxivities measurements of Gd(OH)₃@MSN synthesized via process A (designated as A) and B (designated as B) and MultiHance® at 0.54 T. Relaxivity is the slope of the plot of concentration versus 1/T_n, n=1 or 2.

T₁ maps of Gd(OH)₃@MSN-FITC synthesized by process A and MultiHance® were carried out with a 4.7T MRI system for comparison as shown in Figure 2.10 (A) and (B), where Figure 2.10 (B) is a color display of the same data as in

Figure 2.10 (A) and the difference is better distinguished. Compare Figure 2.10 (C) and (D), T_1 maps of $Gd(OH)_3@MSN$ synthesized by process B and MultiHance® again (D) having the same T_1 values as in (C). From the figures, we could easily see that all T_1 relaxation time, $Gd(OH)_3@MSN$ synthesized by process A or B and MultiHance®, decreased as Gd concentration increased, which indicate more Gd contents would result in better relaxivities, r_1 . Besides, from the T_1 -maps, we notice that $Gd(OH)_3@MSN$ synthesized by either process A or B are better T_1 contrast agents than commercial MultiHance®.

Both $Gd(OH)_3@MSN$ synthesized by process A or B possess similar Gd amounts incorporated, and excellent relaxivities, r_1 , a potential great T_1 contrast agent. However, $Gd(OH)_3@MSN$ with synthetic procedure A showed more uniform and controllable hexagonal mesoporous structures. Hence, we concentrate on $Gd(OH)_3@MSN$ -A for further modifications and applications.

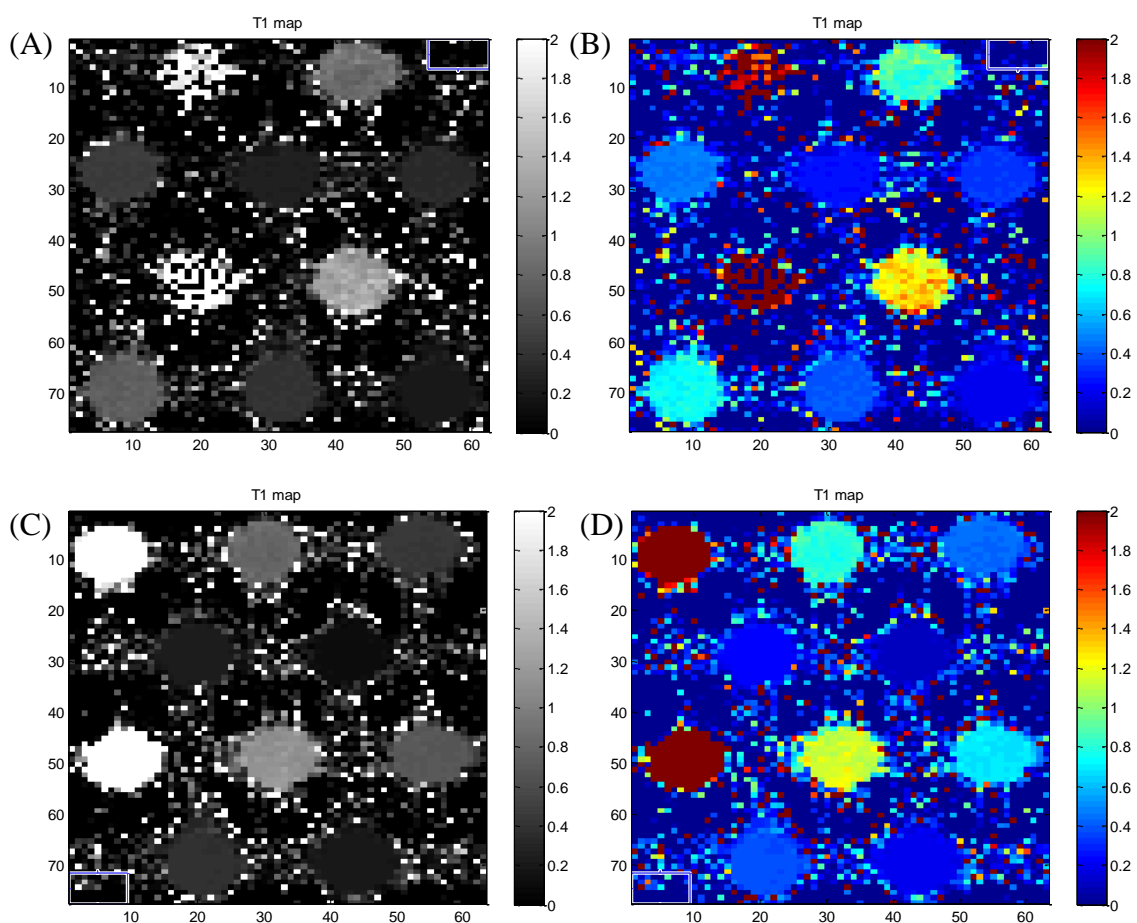


Figure 2.10 (A) T_1 - maps of $Gd(OH)_3@MSN-FITC$ synthesized by process A (upper two panels) and MultiHance[®] (3rd and 4th panels). For both sets, the spots were H_2O , $[Gd] = 0.1M$ (1st row), 0.2M, 0.4M and 0.8M (2nd row) sequentially from left to right. (B) The same T_1 data as (A) but with colors to better differentiate T_1 variations. (C) T_1 -maps of $Gd(OH)_3@MSN$ synthesized by process B (upper two panels) and MultiHance[®] (3rd and 4th panels). For both sets, the spots were H_2O , $[Gd] = 0.1M$ (1st row), 0.2M, 0.4M and 0.8M (2nd row) sequentially from left to right. (D) The same T_1 -map data as (A) but with colors to better differentiate the T_1 variations. For (A) to (D), scale bars represent the T_1 values, larger numbers are longer T_1 .

2.3.2 Characterization of Various Gadolinium-Loaded MSNs

Varying the amount of Gd stock solution from 300 μL to 2400 μL , we can obtain $\text{Gd}(\text{OH})_3@ \text{MSN}$ with various $\text{Gd}(\text{OH})_3$ from 1.9 w.t.% to 7.2 w.t.% incorporated into silica frame work while maintain the hexagonal crystal-like mesoporous structures.

Physical and chemical characterizations: TEM images of different amount of Gd-incorporated mesoporous silica nanoparticles are shown in Figure 2.11. As the amount of Gd incorporation increased, the particles became largely aggregated and tended to show the worm-like structures.

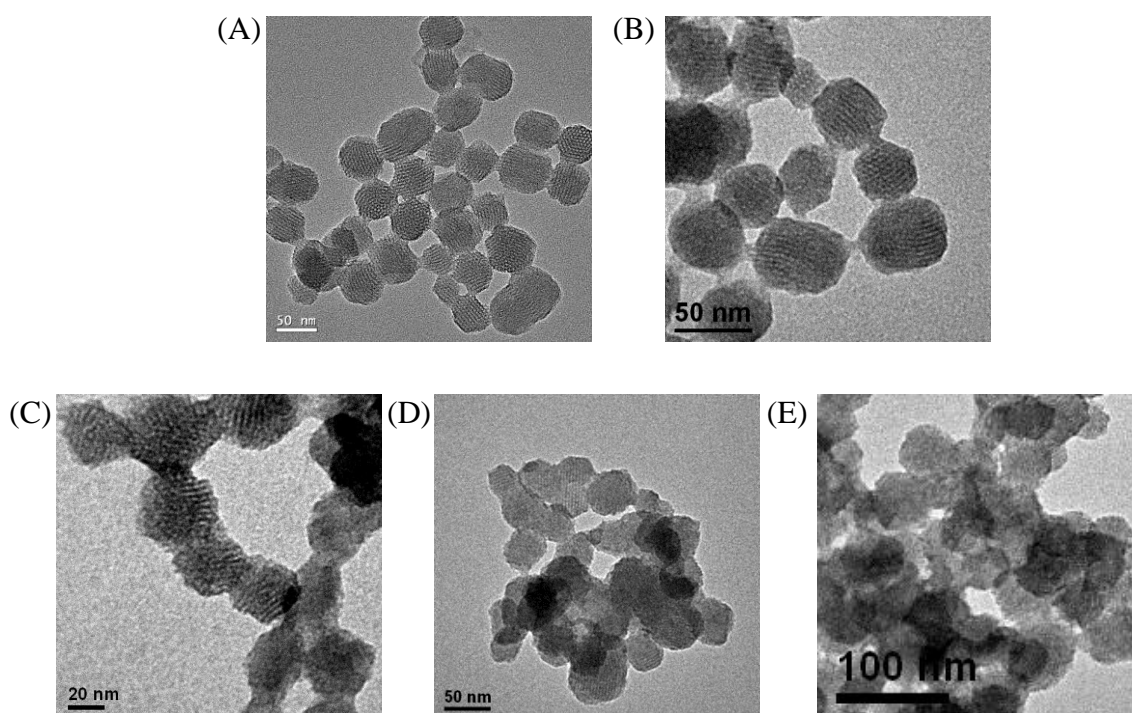


Figure 2.11 TEM images of $\text{Gd}(\text{OH})_3@ \text{MSN}$ with different Gd loading (A) 0 %, (B) 1.9%, (C) 3.5%, (D) 7.2% and (E) 13.2% obtained from ICP-MS.

Besides, the XRD patterns of different amount of Gd-doped MSNs shown in Figure 2.12 revealed the fact that the structure ordering decreased as the loading of Gd increased indicated by the gradual broadening of peaks. Results from both TEM images and XRD patterns pointed out that pore structures would change from 2D hexagonal well-ordered pores to worm-like pores as Gd loadings get higher.

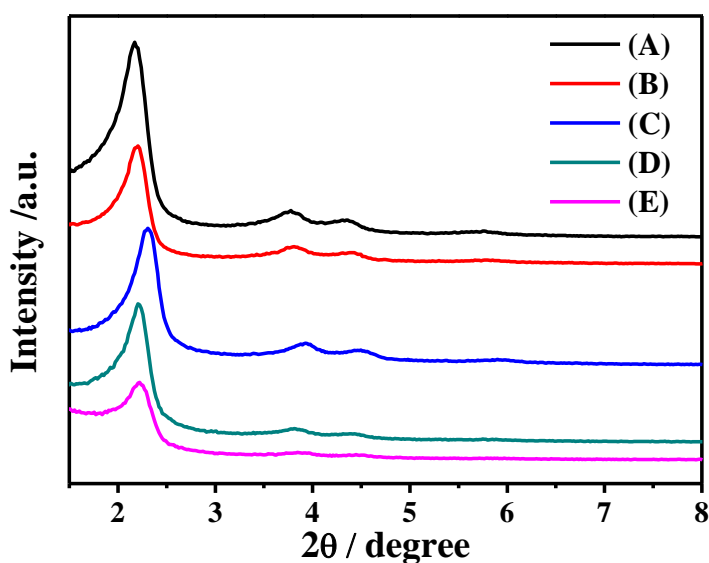


Figure 2.12 XRD patterns of Gd(OH)₃@MSN with different Gd loading (A) 0 %, (B) 1.9%, (C) 3.5%, (D) 7.2% and (E) 13.2%.

Typical N₂ adsorption-desorption isotherms of Gd(OH)₃@MSNs with different Gd amount are shown in Figure 2.13, they exhibited characteristic type IV isotherms and no hysteresis loop was observed. All of the samples possessed a sharp capillary condensation at P/P₀ of 0.2 to 0.4. Also, the sharp climb near P/P₀ of 0.8 to 1.0 was due to the textural porosity resulted from the inter-particle nanospace which was attributed to the assembling of nanoparticles. The surface area and BJH pore size of

different Gd-loaded MSN are listed in Table 2.3. All of the Gd(OH)₃@MSNs possessed high surface area near 1000 m²g⁻¹ except the one with 13.2 % Gd loadings, where some of the pores were collapsed due to the disruption by Gd(OH)₃ and forming worm-like structures. The pore sizes obtained by BJH calculation also revealed that pore sizes decreased as Gd amounts of MSNs increased which indicate the incorporation of Gd into silica framework.

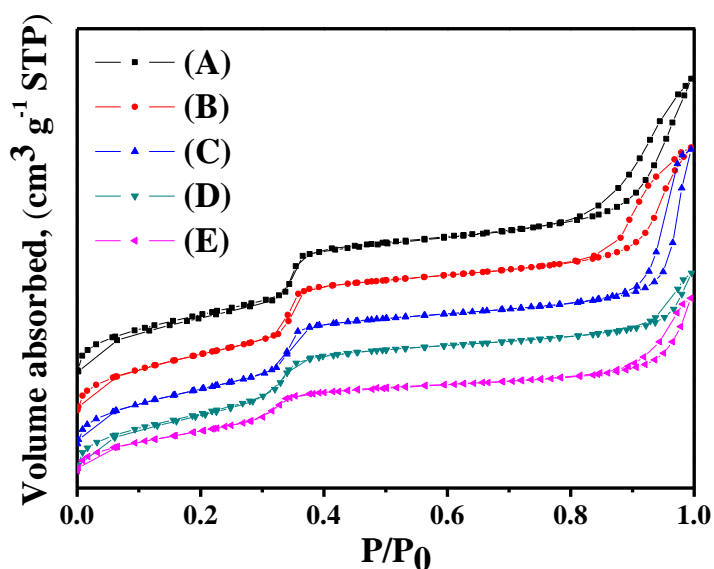


Figure 2.13 N₂ adsorption-desorption isotherms of Gd(OH)₃@MSN with different Gd loading (A) 0 %, (B) 1.9%, (C) 3.5%, (D) 7.2% and (E) 13.2%.

Table 2.3 Structural and textural data of Gd(OH)₃@MSN with different Gd loading.

Sample with Different Gd Loading (% =w.t.)	S _{BET} (m ² /g) ^a	W _{BJH} (nm) ^b
0% Gd(OH) ₃ @MSN	1081	2.53
1.9% Gd(OH) ₃ @MSN	1062	2.47
3.5% Gd(OH) ₃ @MSN	1022	2.42
7.2% Gd(OH) ₃ @MSN	1022	2.37
13.2% Gd(OH) ₃ @MSN	782	2.32

^a BET specific surface area. ^b Pore sizes calculated with BJH method.

Relaxivity measurements, T₁- and T₂- Maps: The relaxivities, r_1 and r_2 of Gd(OH)₃@MSN were determined under 1.41T. Inversion-recovery method was used for T₁ measurements while the spin-echo sequence was used for T₂ measurements. Relaxivity data of various Gd-loaded Gd(OH)₃@MSN under 1.41T and 4.7T were listed in Table 2.4 and Table 2.5, respectively. The r_1 values of different Gd-loaded Gd(OH)₃@MSN gradually decreased as the Gd loading increased at both 1.41T and 4.7T. This change of relaxivity to the Gd loading was related to the dipole-dipole interactions among the Gd metals. Higher Gd loading could shorten the electronic relaxation by the significant interactions between neighboring Gd metals within the same particle.³⁶⁻³⁷ Relaxivity r_2 also showed the similar trend as r_1 ; however, r_2 appeared to be less sensitive to the Gd-loading amount, it did not decrease much as the Gd-loading increased.

Besides, both r_1 and r_2 were highly sensitive to the magnetic field; r_1 at 4.7T was lower than r_1 at 1.41 T almost half the value while the r_2 was higher at 4.7T than that at 1.41T. The obvious change in field dependence of r_1 and r_2 matched the previous reports,³⁸⁻³⁹ which may be attributed to the magnetic susceptibility, especially the Curie spin relaxation mechanism.^{31, 40-41}

From Table 2.5, we could also find out that Gd(OH)₃@MSN exhibit higher relaxivity, r_1 than the commercial contrast agent Magnevist®. There were two plausible

explanations for these phenomena. First, Magnevist®, so-called Gd-DTPA, is dimeglumine salt of a gadolinium complex of diethylenetriamine pentaacetic acid and is classified as ionic gadolinium contrast agent. Compared with Magnevist®, Gd(OH)₃@MSN with MSN serving as a nanoparticle platform could slow down the tumbling rate of the whole particle and hence enhance the relaxivity, r_1 . And the second reason was related with the more coordination to H₂O provided by Gd(OH)₃@MSN compared to commercial contrast agents.

Table 2.4 Relaxivity of Gd(OH)₃@MSN with different Gd loading at 1.41T.

Sample with Different Gd Loading (% =w.t.)	$r_1(\text{mM}^{-1}\text{s}^{-1})$	$r_2(\text{mM}^{-1}\text{s}^{-1})$
1.9% Gd(OH) ₃ @MSN	18.8	27
3.5% Gd(OH) ₃ @MSN	15	21.7
7.2% Gd(OH) ₃ @MSN	11.3	17.8
13.2% Gd(OH) ₃ @MSN	8.6	14.8

Table 2.5 Relaxivity of Gd(OH)₃@MSN with different Gd loading and commercial contrast agent Magnevist® at 4.7T.

Samples	$r_1(\text{mM}^{-1}\text{s}^{-1})$	$r_2(\text{mM}^{-1}\text{s}^{-1})$
3.5% Gd(OH) ₃ @MSN ^{a,b}	8.8	38.1
7.2% Gd(OH) ₃ @MSN ^a	5.8	38.7
13.2% Gd(OH) ₃ @MSN ^a	4.4	36.8
Magnevist®	3.8	5.4

^a Gd(OH)₃@MSN with different Gd Loading (% =w.t.) ^b Both Gd and organic dye,

FITC, incorporated MSN.

The T_1 -weighted and T_2 -weighted phantom images of various Gd-loaded MSN were obtained with a 4.7T Biospec spectrometer as shown in Figure 2.14 and Figure 2.15. From Figure 2.14, we could easily find out that 1) as the concentration of the nanoparticles and Gd increased, the T_1 images lightened up gradually, 2) among different Gd-loaded $Gd(OH)_3@MSN$, the one with 3.5w.t.% Gd loadings showed the fastest lightening up images as the Gd amount increased, 3) comparing 3.5 w.t.% Gd-loaded MSN with commercial contrast agent Magnevist[®], the former showed much brighter image with the same Gd concentration which indicated 3.5 w.t.%- $Gd(OH)_3@MSN$ is a better T_1 shortening enhancer and also a greater T_1 contrast agent. On the other hand, the T_2 -weighted images of Figure 2.15 presented the opposite results, where the images darkened as the Gd concentration increased. Besides, $Gd(OH)_3@MSN$ with all Gd amounts showed more significant darkening effect than that of Magnevist[®]. This also revealed that $Gd(OH)_3@MSN$ could serve as T_2 -enhancing MRI contrast agents under high magnetic field.

To sum up, we've seen that $Gd(OH)_3@MSN$ with higher Gd-loading possessing poor pore structures and less T_1 -enhancing ability. However, the Gd-loading amount is still a very important factor when designing contrast agent. Because contrast agent with less Gd amount means less sensitivity⁴² and also higher dose must be injected to provide sufficient contrast, which may be a burden to human bodies. For

further applications, we decided to use $\text{Gd}(\text{OH})_3@MSN$ with 3.5 w.t. Gd loading amounts which possessed the most moderate properties among all the aspects.

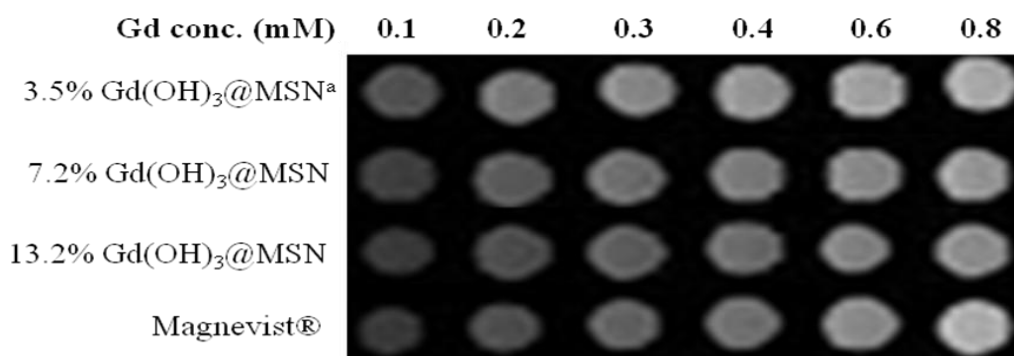


Figure 2.14 T_1 -weighted phantom MR images of $\text{Gd}(\text{OH})_3@MSN$ with different Gd loading (3.5%, 7.2%, and 13.2%) and Magnevist® with a 4.7T Biospec spectrometer using inversion recovery sequence; images were taken at $T_R = 400$ ms.

^aBoth Gd and organic dye incorporated MSN, $\text{Gd}(\text{OH})_3\text{-FITC}@MSN$.

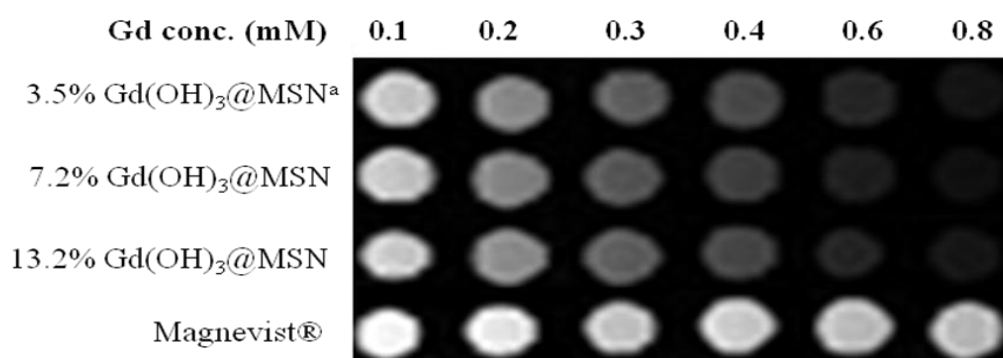


Figure 2.15 T_2 -weighted phantom MR images of $\text{Gd}(\text{OH})_3@MSN$ with different Gd loading (3.5%, 7.2%, and 13.2%) and Magnevist® with a 4.7T Biospec spectrometer using spin-echo sequence; images were taken at $T_E = 80$ ms.

^aBoth Gd and organic dye incorporated MSN, $\text{Gd}(\text{OH})_3\text{-FITC}@MSN$.

2.3.3 Characterization of Gd(OH)₃-FITC@MSN

We used the co-condensation method to covalently incorporate dye molecules (FITC) into the silica framework of 3.5 w.t.% Gd-loaded mesoporous silica nanoparticles (as section 2.3.2 reported) to form Gd(OH)₃-FITC@MSN.

Physical, Chemical and Biological Properties

Transmission electron microscopy (TEM): TEM images of Figure 2.16 showed that both Gd and organic dye functionalized mesoporous silica nanoparticles also displayed the hexagonal crystal-like morphology as the typical as-synthesized mesoporous silica nanoparticles.

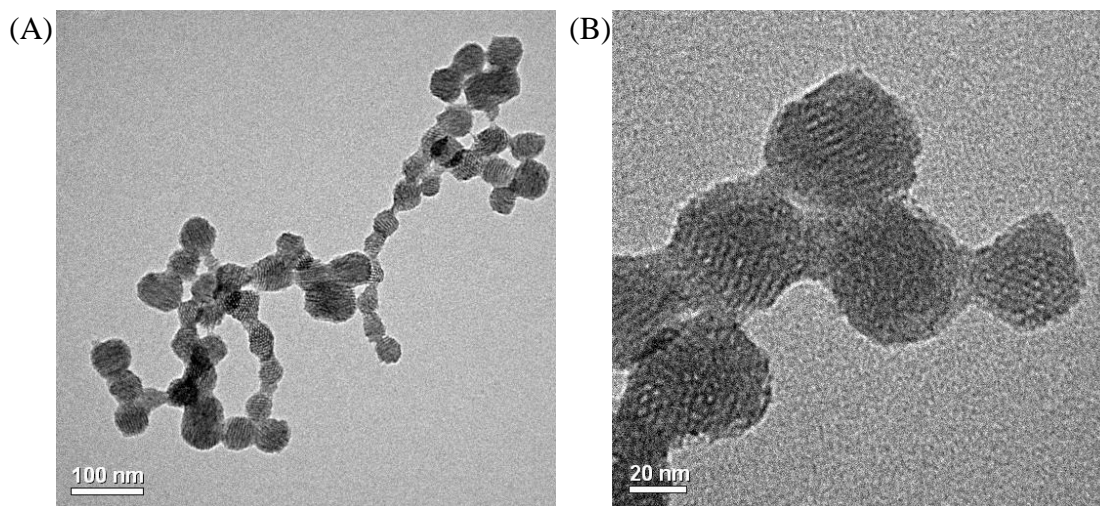


Figure 2.16 TEM images of as-synthesized Gd(OH)₃-FITC@MSN, (A) and (B) were taken under different magnifications.

Powder X-ray diffraction (XRD): The mesostructure of Gd(OH)₃-FITC@MSN

after template removal by extraction was examined by XRD as shown in Figure 2.17.

XRD pattern exhibited three hexagonal characteristic reflection peaks (100), (210) and (200) which indicated the well-ordered 2-D hexagonal mesoporous characteristic.

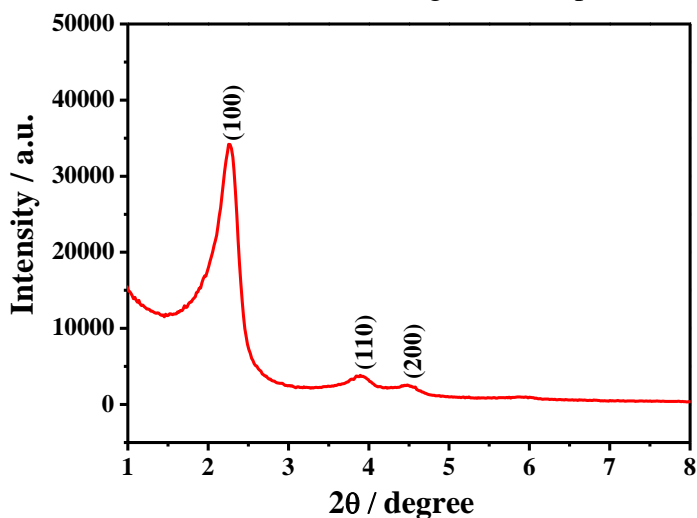


Figure 2.17 XRD patterns of extracted Gd(OH)₃-FITC@MSN.

Dynamic light scattering (DLS): Dynamic light scattering (DLS)

measurements from Figure 2.18 gave an average size of 247 nm confirming that

Gd(OH)₃-FITC@MSN was well-dispersed in water.

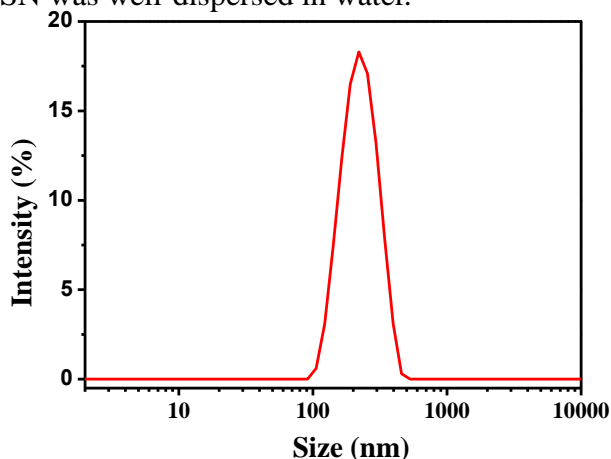


Figure 2.18 Dynamic light scattering (DLS) measurements of Gd(OH)₃-FITC@MSN.

Inductively coupled plasma-mass spectrometry (ICP-MS): Gd-loading amount

of Gd(OH)₃-FITC@MSN was about 3.5 w.t.% analyzed by ICP-MS.

Magnetic Resonance Properties

Relaxivities measurements (1.41T and 4.7T): Since Gd(OH)₃-FITC@MSN nanoparticles were well-dispersed in water, the T₁ and T₂ enhancing capabilities, r_1 and r_2 could be measured directly. The relaxivities, r_1 or r_2 is the slope obtained by plotting $1/T_1$ or $1/T_2$ versus [Gd] content, respectively. The relaxivity r_1 was found out to be 15.4 mM⁻¹s⁻¹ from Figure 2.19, and r_2 was 22.7 mM⁻¹s⁻¹ from Figure 2.20. Both figures were with $R^2 = 0.999$ which indicated the high quality of the data. We also listed the relaxivities, r_1 and r_2 of Gd(OH)₃-FITC@MSN and commercial contrast agent, Magnevist® under two different magnetic field in Table 2.6 for comparison. We observed that 1) under higher magnetic field, relaxivity, r_1 of Gd(OH)₃-FITC@MSN increased as r_2 increased because of the magnetic susceptibility, and 2) Gd(OH)₃-FITC@MSN possessed both better T₁ and T₂ enhancing abilities compared to Magnevist® which indicated that Gd(OH)₃-FITC@MSN could serve as not only a powerful T₁ contrast agent but also a T₂ contrast agent.

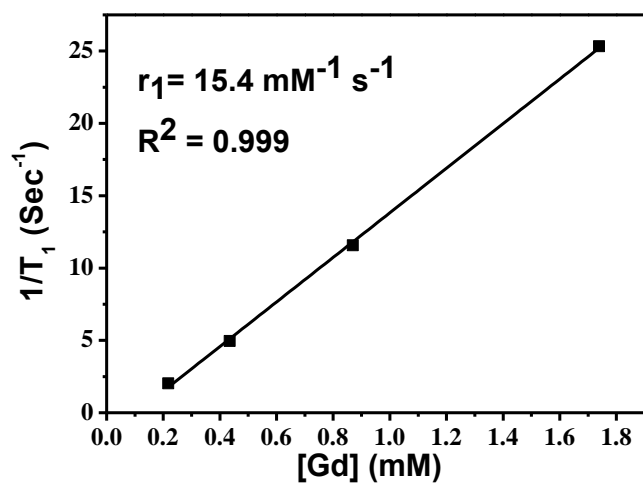


Figure 2.19 T₁ relaxivity plot of Gd(OH)₃-FITC@MSN taken under 1.41T.

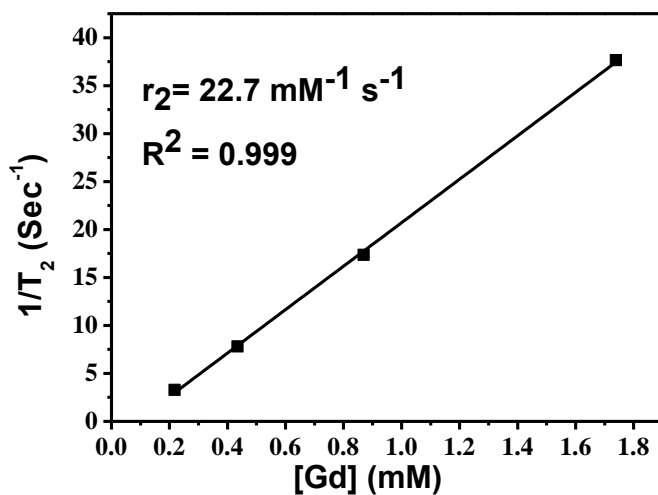


Figure 2.20 T₂ relaxivity plot of Gd(OH)₃-FITC@MSN taken under 1.41T.

Table 2.6 Relaxivities, r_1 and r_2 of Gd(OH)₃-FITC@MSN and commercial contrast agent, Magnevist® under 1.41T and 4.7T

samples	1.41T		4.7T	
	r_1	r_2	r_1	r_2
Gd(OH) ₃ -FITC@MSN	15.4	22.7	8.8	38.1
Magnevist®	--	--	3.8	5.4

T₁- and T₂- weighted MR phantom images under 4.7T: T₁- and T₂-weighted MR phantom images of Gd(OH)₃-FITC@MSN were carried out at 4.7T MR system as shown in Figure 2.14 and Figure 2.15, respectively. We could tell that the image lightens up faster than the corresponding Magnevist® , indicating Gd(OH)₃-FITC@MSN is a good T₁ contrast agent. On the other hand, T₂-weighted image also darkens faster than Magnevist® . To sum up, Gd(OH)₃-FITC@MSN could be used as a good dual contrast agent for both T₁- and T₂-weighted MR imaging.

2.3.4 Biological Applications of Gd(OH)₃-FITC@MSN

Cell-based therapy combined with molecular imaging has emerged as a powerful therapeutic tool for tracking the *in vivo* bio-distributions of the transplanted cells and the effects of the cell-based therapy.⁴³⁻⁴⁴ Besides, transporting contrast agents into the body through transplanted cells would be more biocompatible and cause less harm than directly injection. Hence, *in vitro* cell MR imaging with Gd(OH)₃-FITC@MSN nanoparticles was examined. We first did some cell uptake examinations, including uptake efficiency, cytotoxicity and biocompatibility. After that, two cell types including NIH3T3 cells which are embryo-derived fibroblasts maintaining a stem cell-like differentiation flexibility,⁴⁵ and mouse embryonic stem cells which could differentiate into most cell types and offer unprecedented therapeutic potential⁴³ were labeled with multifunctional contrast agent, Gd(OH)₃-FITC@MSN for *in vitro* MR studies.

Gd(OH)₃-FITC@MSN for NIH3T3 Cell Labeling

Cell-uptake analysis of Gd(OH)₃-FITC@MSN: In the cell-uptake experiments, NIH 3T3 cells were incubated with different concentration of Gd(OH)₃-FITC@MSN suspension in a serum-free low-glucose Dulbecco's modified Eagle's medium (DMEM) to avoid the non-specifically binding of serum in a regular medium. The incubation time

lasted for 4 hours because the previous report⁴⁶ showed that 3T3 cell-labeling efficiency reached 99% for an incubation time of 2 hours with mesoporous silica nanoparticles, a longer incubation time won't affect the labeling efficiency either. The flow cytometry data was collected in the Figure 2.21. The vertical coordinate represents the percentage of particle-labeled cells versus total counting cells. It was found that an increase in the concentration of Gd(OH)₃-FITC@MSN resulted in a higher amount of particle engulfed. Results from flow cytometry analysis showed that Gd(OH)₃-FITC@MSN had actually been taken into cells.

Fluorescence images from Figure 2.22 (the white circle indicates individual cell) also provided another evidence to prove that Gd(OH)₃-FITC@MSN was internalized into cells by the green fluorescent spots in cytoplasm. Since no nanoparticles were observed in the nuclei, we could eliminate the possibility that Gd(OH)₃-FITC@MSN were only attached on the cell surface instead of being taken into the cells. Besides, in the previous work from our group, it had been demonstrated that the non-phagocytic cell internalization of fluorescent mesoporous silica nanoparticles (FITC-MSN)⁴⁷ and multifunctional nanorods (GD-Dye@MSN-R)⁴⁶ were involved in a clathrin-dependent endocytosis.

The effect of Gd(OH)₃-FITC@MSN on NIH 3T3 viability was also examined. MTT assay from Figure 2.23 showed that there was no strong effect on cell viability

even at very high concentration such as 200 $\mu\text{g}/\text{mL}$, indicating $\text{Gd}(\text{OH})_3\text{-FITC@MSN}$ is not toxic to fibroblast cells and could be bio-safe for further biomedical applications.

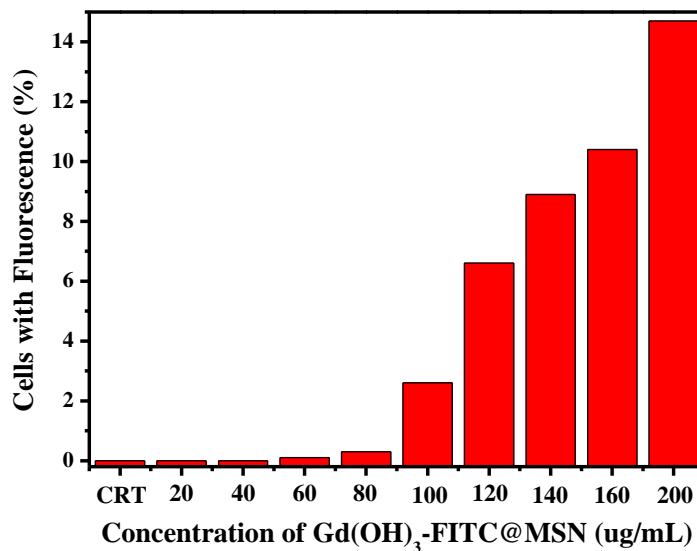


Figure 2.21 Flow cytometry study on NIH3T3 cell-uptake of $\text{Gd}(\text{OH})_3\text{-FITC@MSN}$ with different concentration.

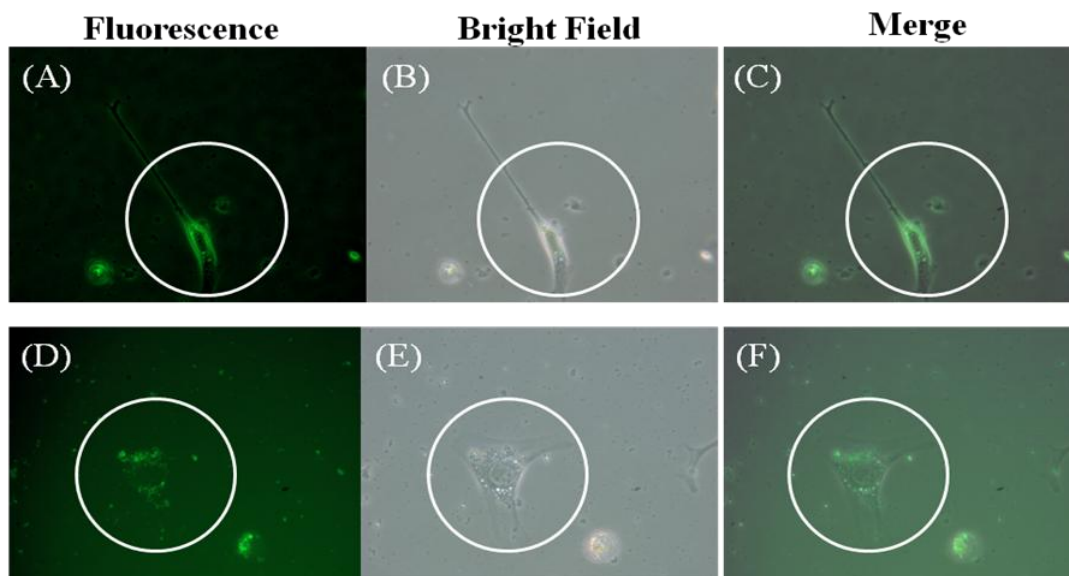


Figure 2.22 (A) and (D) Fluorescence, (B) and (E) optical and (C) and (F) fluorescence- and optical-merged images of NIH3T3 cells after incubated with 200 $\mu\text{g} / \text{mL}$ $\text{Gd}(\text{OH})_3\text{-FITC@MSN}$ for 4 hours.

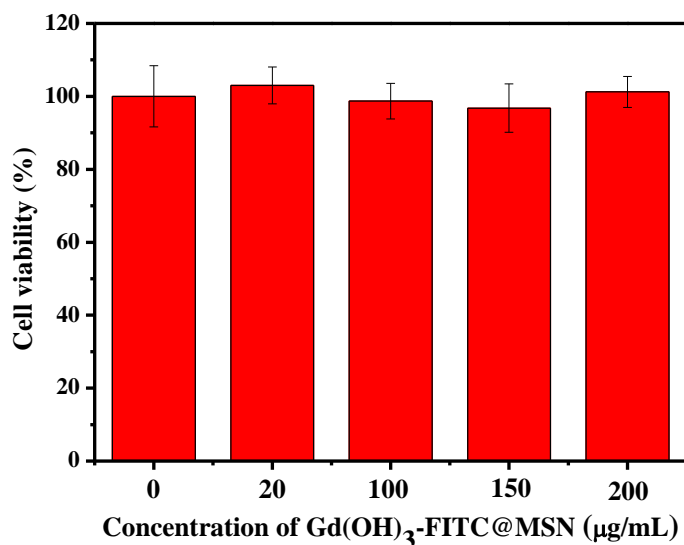


Figure 2.23 MTT assay of NIH3T3 cells incubated with different amount of Gd(OH)₃-FITC@MSN for 4 hours.

MR phantom images of NIH3T3 cells treated with Gd(OH)₃-FITC@MSN: We used two MR system with different magnetic field (4.7 T & 7T) to obtain T₁- and T₂-weighted images of NIH3T3 cells. The cells for MR images were prepared by incubating 2.5x10⁵ cells with different concentrations from 0, 50, 100, 200, to 400 µg / mL of Gd(OH)₃-FITC@MSN for 4 hours followed by trypsinization and centrifugation to form cell pellets. Cell pellets composed of 6x10⁵ viable cells were then resuspended in 1% melted agarose for obtaining MR images with a 4.7 T MR system as shown in Figure 2.24. T₁-weighted image of the cells treated with Gd(OH)₃-FITC@MSN exhibited brighter MR image compared to the untreated cells denoted as control, and the images were significantly brighter when the treated concentration was 100 µg / mL or higher (Figure 2.24 (A)). On the other hand, in T₂-weighted MR images, the cells

treated with Gd(OH)₃-FITC@MSN exhibited significantly darker images compared to the untreated one (Figure 2.24 (B)).

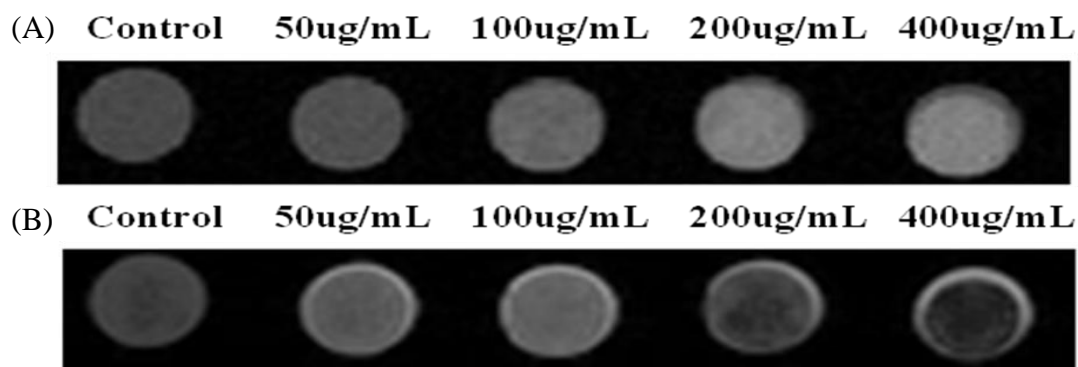


Figure 2.24 (A) T₁-weighted and (B) T₂-weighted MR images of NIH3T3 cells treated with Gd(OH)₃-FITC@MSN for 4 hours using 4.7 T MR instrument.

T₁ relaxation time of NIH3T3 cells treated with various amount of Gd(OH)₃-FITC@MSN obtained at 4.7 T were listed in Table 2.7. As the amount of Gd(OH)₃-FITC@MSN increased, cell T₁ relaxation time decreased and the bright contrast of T₁-weighted image enhanced as depicted in Figure 2.24. Since T₁ values of human brain at 4.7 T which is 1630 ms for grey matters,⁴⁹ one may be able to differentiate the transplanted cells and surrounding normal tissues using cells treated with 200 µg / mL or higher dosage of Gd(OH)₃-FITC@MSN. From this and the previous MTT assay results which show the biocompatibility of Gd(OH)₃-FITC@MSN at the concentration of 200 µg / mL, we believe Gd(OH)₃-FITC@MSN as a contrast agent could be effectively combined with cell-based therapy for future applications.

Table 2.7 T₁ relaxation time of NIH3T3 cells treated with Gd(OH)₃-FITC@MSN

Gd(OH) ₃ -FITC@MSN concentration (μg / mL)	0 (Control)	50	100	200	400
T ₁ relaxation time (ms) at 4.7T	2630	2470	2057	1160	947

Pellets formed with 1.2×10^6 viable cells were also scanned under a 7T MRI system. From Figure 2.25, we observed strong MR image enhancement of the labeled cells when compared with unlabeled NIH3T3 cells as a control. Significant positive signal enhancement of T₁-weighted image and negative signal enhancement of T₂-weighted image were detected for the Gd(OH)₃-FITC@MSN treated cells. And the great T₁ enhancement could be observed even at 7T indicating the great potential of Gd(OH)₃-FITC@MSN to be a T₁ contrast agent.

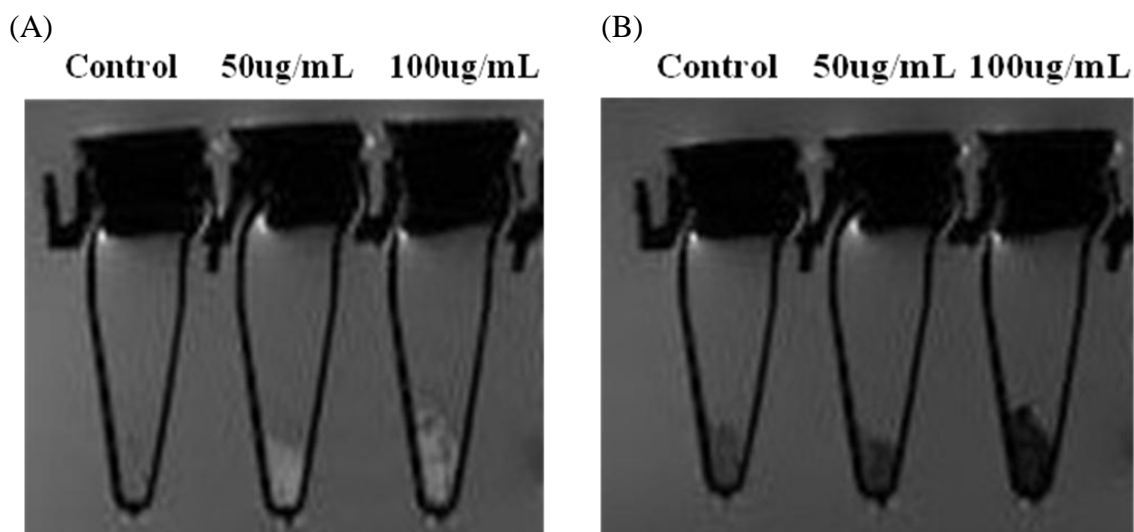


Figure 2.25 (A) T₁-weighted and (B) T₂-weighted MR images of cells treated with Gd(OH)₃-FITC@MSN for 4 hours using 7 T MR instrument.

Gd(OH)₃-FITC@MSN for Embryonic Stem Cell Labeling

We also labeled the mouse embryonic stem cells with Gd(OH)₃-FITC@MSN for MR imaging study. To prepare the cells for MR imaging, we incubated 10⁶ cells in media containing Gd(OH)₃-FITC@MSN with different concentration for 24 hours. The cells were isolated, washed with PBS solution and 6x10⁵ viable cells were redispersed in 1% melted agarose. As shown in Figure 2.26 (A) and (B), T₁- and T₂- weighted enhancement are clearly visible for the labeled cells. And the enhanced contrast became significantly obvious when nanoparticle treated concentration was 200 µg / mL or higher. However, the DAPI staining of Figure 2.27 pointed out the fact that when Gd(OH)₃-FITC@MSN was 200 µg / mL as in Figure 2.27 (D), the cell morphology lost the spherical shape and tended to aggregate indicating the cells lost viability. It is not too surprising because embryonic stem cells are more fragile and difficult to culture in the laboratory,⁴⁹ not to mention its endurance to uptake foreign nanoparticles. We also believe NIH3T3 fibroblast cells incubated with Gd(OH)₃-FITC@MSN contrast agents seem to be more promising for future cell-based therapy by comparing the MR study results and cell viability tests of NIH3T3 fibroblast cells and embryonic stem cells.

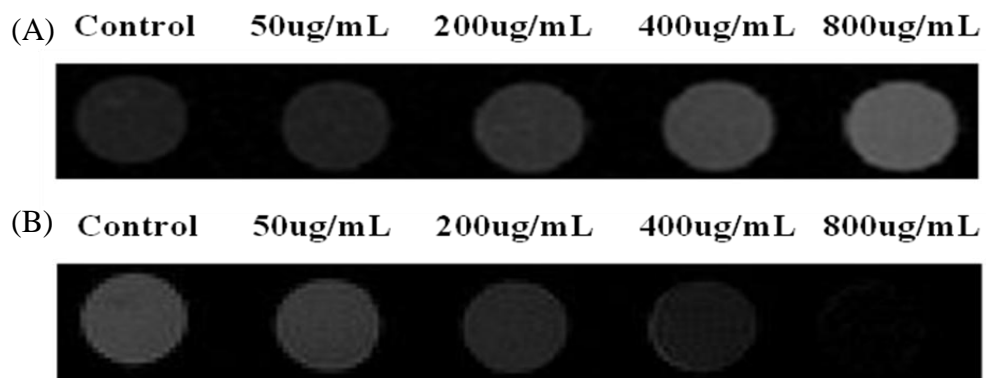


Figure 2.26 (A) T₁-weighted and (B) T₂-weighted MR images of embryonic stem cells treated with Gd(OH)₃-FITC@MSN for 4 hours using 4.7 T MR instrument.

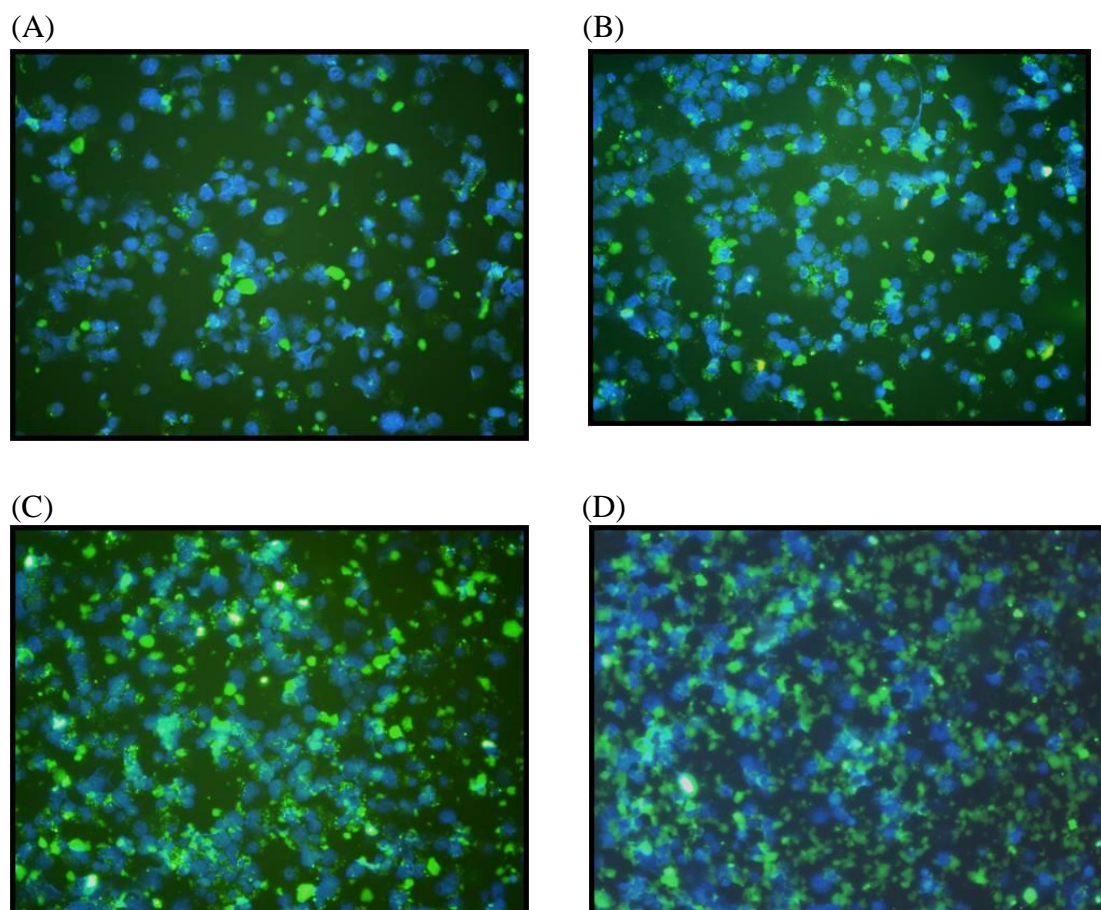


Figure 2.27 Fluorescence images of embryonic cells labeled with (A) 25 µg / mL (B) 50 µg / mL (C) 100 µg / mL and (D) 200 µg / mL of Gd(OH)₃-FITC@MSN. The nuclei were stained by DAPI.

2.4 Conclusion

In summary, a facile and one pot synthesis of multimodal mesoporous silica nanoparticle, Gd(OH)₃-FITC@MSN, with extraordinary capability to enhance MR contrast images has been developed for the first time. Its utility as contrast agents for optical and MR images has been clearly shown *in vitro*. Gd(OH)₃-FITC@MSN exhibit much higher relaxivities than those of commercial contrast agents, MultiHance® and Magnevist® ; this is probably because of the much decrease of the Gd metal rotational motion imposed by the porous framework and more than one water could be coordinated to metal other than only one water molecule coordination in MultiHance® and Magnevist® . Besides, NIH3T3 cells treated with Gd(OH)₃-FITC@MSN show the high sensitivity even at high magnetic fields (4.7 T and 7 T) indicating it could serve as a highly efficient T₁ or T₂ contrast agent for efficient cell-based therapy in future applications. Together with the retained uniform porosity, well-ordered hexagonal array, powerful dual contrast capabilities and further surface functionalization, Gd(OH)₃-FITC@MSN can serve as a platform in targeted drug delivery with multimodal imaging.

Chapter Three Controlled PEGylation of Mesoporous Silica

Nanoparticles for Reducing Non-specific Uptake by Macrophage Cells

3.1 Introduction

3.1.1 Brief Introduction of Reticuloendothelial system (RES)

The reticuloendothelial system (RES)-mediated clearance is a critical issue for *in vivo* active targeting and systemic delivery. RES, alternatively known as the mononuclear phagocyte system (MPS), is defined as the cells comprising blood monocytes, bone marrow progenitors, and macrophage cells (such as Kupffer cells from the liver).⁵⁰ These specialized cells are widely distributed and placed in the connective tissue framework of the liver, spleen and lymph nodes to recognize and clear invading particles.⁵⁰⁻⁵¹ The first step of the clearance process is called opsonization which is functioning the nanoparticles with the circulating plasma proteins, opsonins, thereby making it more visible for phagocytic cells.⁵² Opsonins could actively be adsorbed on the surface of any invading nanoparticles, and be recognized by blood monocytes and macrophage cells due to their plasma membrane receptor.⁵⁰ And it would lead to complex aggregation and rapid clearance from the blood stream.⁵³ The next step involves either endocytosis or phagocytosis route to remove the nanoparticles from the blood circulation^{50, 54} and its fate following the intravenous injection is depicted in Figure 3.1.⁵¹

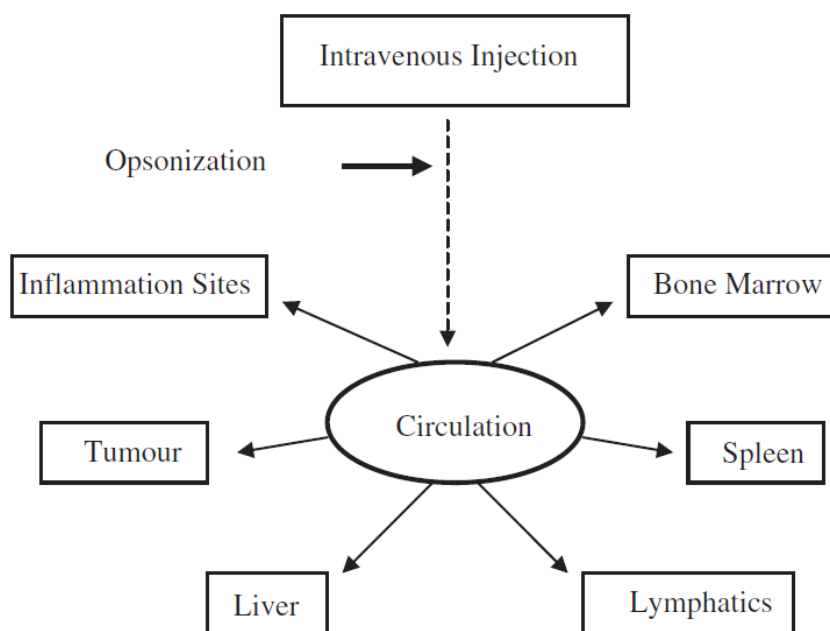


Figure 3.1 The fate of nanoparticles after the intravenous injection.⁵¹

As a result, in order to help the nanoparticles escaping from RES for further *in vivo* and *ex vivo* applications, numerous approaches including appropriate surface modification and particle size reduction to improving nanoparticle blood residence and accumulation in specific tissues have been widely studied over the past twenty years.^{50-51, 53} Besides, the surface modification through polymers and macromolecules becomes the most common method for its ease of further functionalization and bio-compatibility.⁵³

3.1.2 Commonly Used Polymers for Escaping from RES

Recently, to inhibit the plasma proteins coating and evading from the RES for longer circulation times, nanoparticles are usually coated with a layer of hydrophilic and biocompatible polymer chains.^{51,55} It has been demonstrated the more hydrophilic the nanoparticle surface, the longer blood circulation times because of less interaction with opsonins.⁵⁰ The most common coatings are derivatives of dextran, poloxamer, poloxamine, and polyethylene glycol (PEG) as shown in Figure 3.2.⁵⁰ The role of these polymers is to inhibit opsonization, hence allowing longer circulation times.⁵¹

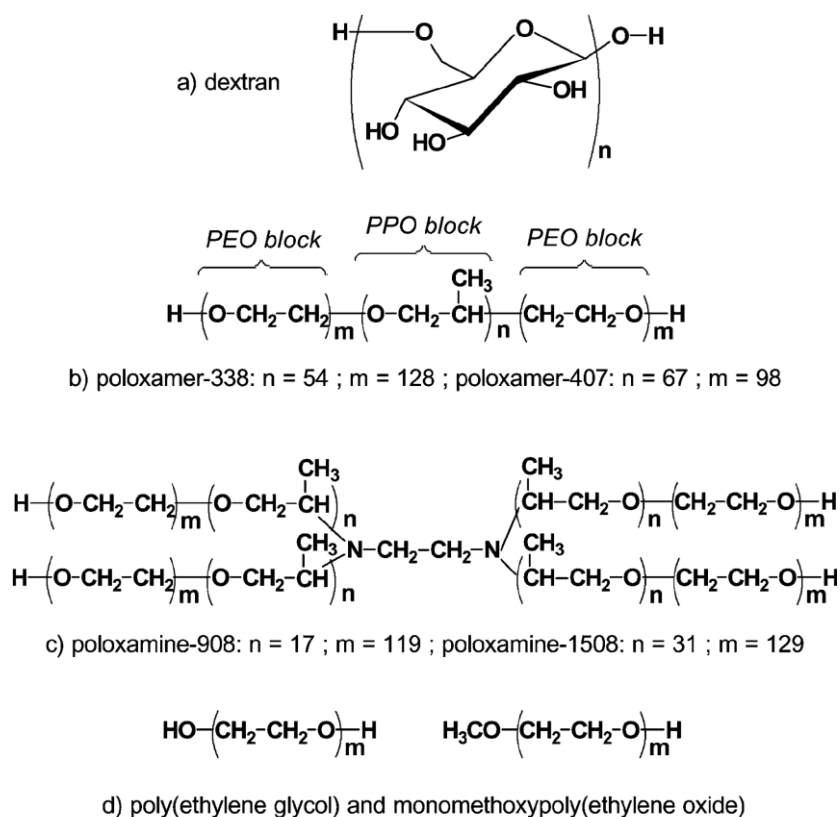


Figure 3.2 Typical polymers used as hydrophilic coating for RES-evading nanoparticles.⁵⁰

It has been demonstrated that particles coated with dextran could remain in the bloodstream for longer periods of time. And as the average molecular weight and surface coating density of dextran molecules are higher, the clearance rate is slower.⁵⁰

Poloxamer and poloxamine are the amphiphilic block-copolymers consisting of blocks of ethylene oxide (EO) and propylene oxide (PO) monomer units.^{50,52} Poloxamers are composed of a central hydrophobic poly (propylene oxide) (PPO) block and two hydrophilic chains of poly(ethylene oxide) (PEO) are on the both sides. On the other hand, poloxamines are tetrafunctional with four PPO/PEO blocks connected together via the central ethylenediamine bridge.⁵⁰ Such copolymers which contain the hydrophobic PPO blocks could be used for adsorbing organic molecules, such as surfactants to the surface of the nanoparticle. And the hydrophilic PEO blocks can extend into aqueous solution and shield the surface to avoid RES.⁵²

The inert and biocompatible polymer PEG is actually the α,ω -dihydroxyl derivative of PEO and has become the most popular materials to modify the nanoparticle surface in order to evade from the RES.⁵⁶ PEG could help nanoparticles reducing the interactions with opsonin proteins by its hydrophilicity and steric repulsion effect.⁵³ Besides, PEG-end groups could also be functionalized with other ligands for specific targeting and delivery.⁵⁷ All these advantages have made PEG the most commonly used material for nanoparticles surface modification.

3.1.3 Polyethylene Glycol (PEG) for Surface Modification - PEGylation

Polyethylene glycol (PEG) is commonly used to modify the nanoparticle surfaces for reducing systemic clearance rates, prolonging circulation half-life *in vivo*, and enhancing permeability and retention (EPR) effect.⁵⁷⁻⁵⁸ It is believed that the chain length, shape, and density of PEG are the critical factors influencing the hydrophilicity of nanoparticle surfaces and phagocytosis.⁵³ Hence, there have been a few reports providing design parameters for engineering nanoparticles for optimized conditions to avoid RES or target the tumors.

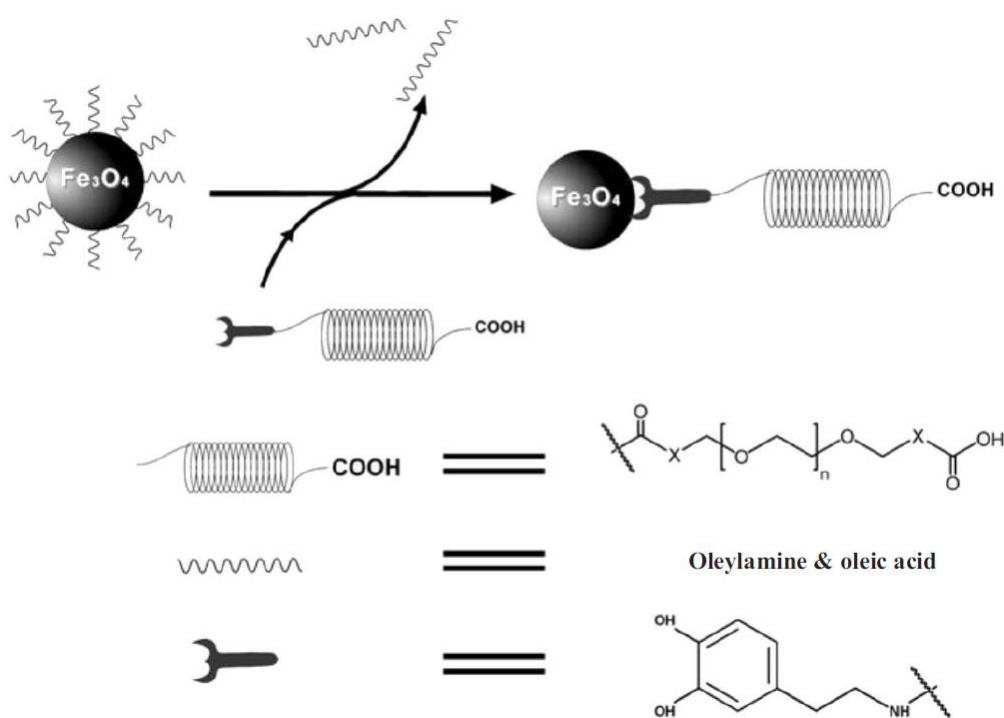
In 2009, C. W. Chan et al. examined the effect of gold nanoparticle size (10-100 nm) and surface modification of poly(ethylene glycol) on efficient tumor targeting as indicated in Table 3.1.⁵⁹ Particle set A is an array of 5 particle size and 3 different thiol-terminated mPEG molecular weight layers used for mapping blood compartment pharmacokinetics (PK). Particles with smaller particle diameters and coated with larger mPEG possessed longer blood half-life in circulation. Besides, blood half-life also increased for each particle size as the molecular weights of mPEG increased. The results from particle set A were then used to design particle set B of sub-100 nm for determining how size affected tumor accumulation and permeation. The accumulation in the tumor of particles having hydrodynamic diameters of approximately 20, 40, 60, 80 and 100 nm were calculated as the area-under-the curve

(AUC), both by particle mass/g over time and % ID/g over time. As the tumor accumulation was examined by particle mass, accumulation enhanced as the size of particles increased. Since this was a measure of how potential payload can be delivered, particles with larger sizes would no doubt deliver most total mass to the tumor owing to its larger volumes. However, it was discovered that total tumor accumulation (% ID·h/g) of the five mPEG-GNP designs is a function of blood half-time and of size. The accumulation of particles having size of 20-60 nm is only dependent on the blood-half time, whereas the accumulation of particles with diameter over 60 nm range depends on both half-time and size. These results provided a basis for gold nanoparticle design parameters, such as the size and surface chemistry, for longer blood circulation time and optimized tumor targeting.

Table 3.1 Methoxy-poly(ethylene glycol) coated gold nanoparticles (mPEG-GNP) characteristic and *in vivo* behavior⁵⁹

	core diameter (nm) (±SD)	mPEG weight (Da)	hydrodynamic diameter (nm)	blood half-Life (h)	tumor AUC (particle mass (ug)·h/g)	tumor AUC (% ID·h/g)
particle set A	17.72 (1.47)	2000	25.2	4.0		
		5000	34.8	29.7		
		10000	63.5	51.1		
	31.28 (4.83)	2000	42.8	2.4		
		5000	62.6	19.3		
		10000	77.5	22.7		
	45.03 (4.83)	2000	53.8	0.4		
		5000	60.4	14.1		
		10000	83.9	16.1		
	66.54 (5.69)	2000	75.7	1.0		
		5000	85.6	9.2		
		10000	105.8	11.3		
86.73 (7.74)	5000	105.4	3.3			
	10000	118.9	6.6			
particle set B	16.6 (1.80)	2000	22.4	2.5	0.45	0.3
	22.6 (2.68)	2000	39.6	4.0	18.89	15.8
	32.5 (5.16)	5000	61.3	16.5	39.05	26.5
	43.3 (5.08)	10000	82.6	11.6	39.33	20.4
	83.5 (8.29)	10000	99.4	7.2	170.42	17.9

A systematic study of controlled PEGylation of Fe_3O_4 nanoparticles was also reported by S. Sun et. al in 2007 as shown in Scheme 3.1.⁵⁵ The 9 nm of Fe_3O_4 nanoparticles coated with PEG of different molecular weights resulted in various hydrodynamic sizes of the particles, the size increased as the molecular weight was higher. However, nanoparticles coated with any length of PEG polymers were stable in both water and physiological environment without detectable agglomeration even after incubated for 24 hours. Furthermore, these PEG coated Fe_3O_4 nanoparticles showed much less uptake by macrophage cells compared with the uncoated ones, indicating the higher possibility to escape from the RES. This also provided the basis for the choice of PEGylated Fe_3O_4 nanoparticles in further biomedical applications.



Scheme 3.1 PEG modification of Fe_3O_4 nanoparticles through DPA-PEG-COOH.

The particle size stability and the potential to avoid the RES appear to be very

important for target-specific cell recognition, cell entry and other biomedical applications of mesoporous silica nanoparticles (MSN) with size less than 100 nm, which is small enough to pass through the body and also is possible to enter cells efficiently.³⁶ However, up to now, a systematic study of the PEGylated 50 nm MSN to show stability of the particles in physiology environment in terms of evading from aggregation and the phagocytosis of RAW 264.7 macrophage cells have not been addressed as far as we know. In this work, red light emitting dye modified MSNs were PEGylated though covalently conjugating PEG-maleimide of different molecular weights and different concentration on the outer surfaces of 50 nm MSNs. We then investigated the influences of molecular weights and chain densities of PEG on the hydrodynamic size stability of PEGylated MSN in cell culture or physiology environment, and the optimized values of the two factors were achieved. Also, MSNs modified with the optimal molecular weights and chain densities of PEG showed significant reduction of non-specific uptake by RAW 264.7 macrophage cells compared to the ones without PEG coating or PEGylated with lighter molecular weight and thinner densities. And we believed the results of this MCM-41 type MSN system, possessing fluorescence imaging probe and potential for further coupling with other desired biomolecules, could provide optimized particle design parameters for future biomedical applications.

3.2 Experiments

3.2.1 Materials

Hexadecyltrimethyl- ammonium bromide (CTAB, 99+%), tetraethyl orthosilicate (TEOS, 98%), 3-aminopropyl-trimethoxysilane (APTMS, 95%), ammonium hydroxide (NH₄OH, 28-30% as NH₃), tris(2-carboxyethyl)phosphine hydrochloride (TCEP, 98%), sodium chloride (NaCl, 99.5%), sodium phosphate dibasic (NaPO₃·2H₂O) and sodium hydroxide standard solution (1N) were obtained from Acros Organics. Rhodamine B isothiocyanate (RITC, mixed isomers) were purchased from Sigma. Hydrochloric acid (HCl, 36%) was obtained from Fisher Scientific. (3-Mercaptopropyl)-trimethoxysilane (MPTMS, 95%) was purchased from Aldrich. PEG maleimide (mPEG-Mal, MW10000, 20000 and 30000) were obtained from Nanocs. All chemicals were used without further purification.

3.2.2 Synthesis of Thiol Group Modified Mesoporous Silica Nanoparticles

SH@MSN with Different Amounts of Thiol Groups

1.6 mmol of hexadecyltrimethylammonium bromide, C₁₆TAB, was dissolved in 300g of 0.17M NH₄OH and 5mL of 0.226M TEOS ethanolic solution was added under stirring. The resulting solution was vigorously stirred at 40°C for 5 hours. Then, 5mL of 1.13M TEOS ethanolic solution was added and the solution was allowed to stir for another 1 hour. The solution was then aged at 40°C for 24 hours. The as-synthesized MSN solution was centrifuged at 15000rpm for 20 minutes and washed and redispersed in 50mL of ethanol. And 1mL of MSN / ethanol solution was transferred into a cell centrifuge tube, the supernatant was removed and the precipitates were dried at 60 °C for 24 hours to obtain the MSN (mg) amount per mL. 100mg of MSN was dispersed in 20mL of ethanol solution and various amount of (3-Mercaptopropyl)-trimethoxysilane (MPTMS) (100μL, 200μL, and 250μL) were added with stirring. The mixture was kept at 85 °C for 24 hours and then centrifuged, washed and redispersed in ethanol solution, obtaining thiol group conjugated MSN (SH@MSN). In order to extract the surfactants via a fast and effective ion exchange method, as-synthesized SH@MSN was transferred to 25mL of ethanol solution containing 0.5g of HCl and heated under 60°C with stirring for 24 hours. After the extraction, the SH@MSN were washed with ethanol and then redispersed and stored in 99.5% ethanol. Solid samples for Elemental Analyzer (EA)

characterizations were obtained by centrifugation followed by drying at 60 °C for 24 hours.

Synthesis of SH-RITC@MSN for further PEG Modification

The preconjugated APTMS-RITC was prepared by combining 200uL of APTMS and 5mL of 0.42 mM RITC ethanolic solution under continuous stirring and dark conditions at room temperature for 24 hours. In a typical synthetic procedure for both thiol group and RITC dye modified mesoporous silica nanoparticles (MSN), 1.6 mmol of hexadecyltrimethylammonium bromide, C₁₆TAB, was dissolved in 300g of 0.17M NH₄OH and 5mL of 0.226M TEOS ethanolic solution was added under stirring. The resulting solution was vigorously stirred at 40°C for 5 hours. Then, 5mL of APTMS-RITC and 5mL of 1.13M TEOS ethanolic solution was added sequentially, and the solution was allowed to stir for another 1 hour. The solution was then aged at 40°C for 24 hours. The as-synthesized RITC@MSN solution was centrifuged at 15000rpm for 20 minutes and washed and redispersed in 50mL of ethanol. And 1mL of RITC@MSN / ethanol solution was transferred into a cell centrifuge tube, the supernatant was removed and the precipitate was dried at 60 °C for 24 hours to obtain the RITC@MSN (mg) amount per mL. 100mg RITC@MSN was dispersed in 20mL of ethanol solution and 250μL of (3-Mercaptopropyl)-trimethoxysilane (MPTMS) was

added with stirring. The solution was kept at 85 °C for 24 hours and then centrifuged, washed and redispersed in ethanol solution obtaining both thiol group and RITC conjugated MSN (SH-RITC@MSN). In order to extract the surfactants, as-synthesized SH-RITC@MSN was transferred to 25mL of ethanol solution containing 0.5g of HCl and heated under 60°C for 24 hours. After extraction, SH-RITC@MSN was washed with ethanol and then redispersed and stored in 99.5% ethanol.

3.2.3 Procedure of Polyethylene Glycol Modification (SH-RITC@MSN-PEG)

Preparation of PEG solution

The sodium chloride-phosphate buffer solution constituted of 150 mM aqueous sodium chloride solution and 50 mM aqueous sodium phosphate aqueous solution was prepared by adding 0.8766g NaCl and 0.69g NaPO₃·2H₂O in 100ml H₂O. And then 1N sodium hydroxide solution was added to tune the pH value to 7.2. A series of PEG solutions with different mole ratio of thiol groups to PEG (including 1:1, 2:1 and 4:1) and PEG molecular weights (M.W. = 10, 20 and 30 kDa) was prepared by dissolving X mg of PEG as illustrated in Table 3.2 in 6mL previous described sodium chloride-phosphate buffer solution containing 5mM tris(2-carboxyethyl)phosphine hydrochloride (TCEP) solution.

Table 3.2 Nine conditions for coating SH-RITC@MSN with PEG

M.W. \ Ratio^a	1:1	2:1	4:1
PEG M.W. = 10 kDa	112.5mg	56.4mg	28.2mg
PEG M.W. = 20 kDa	225mg	112.5mg	56.4mg
PEG M.W. = 30 kDa	337.5mg	169.2mg	84.6mg

^aRatio represents the mole ratio of “thiol groups modified on the surface of RITC@MSN” to “PEG” ; thiol group of MPTMS was quantified by elementary analysis

Different PEG Molecular Weights and Molar Ratios to Thiol Group

To modify SH-RITC@MSN with PEG, 6mg of SH-RITC@MSN was first

dispersed in 3mL of 5mM tris(2-carboxyethyl)phosphine hydrochloride (TCEP) aqueous solution. The solution was sonicated for 10 minutes and centrifuged at 16000 rpm for 10 minutes. The supernatant was then removed and the precipitates resuspended by in a series of PEG solutions follow by stirring at room temperature for 24 hours. The as-synthesized SH-RITC@MSN-PEG solution was centrifuged, washed with ethanol and then redispersed and stored in 6mL 99.5% ethanol.

3.2.4 Cell Culture and Assays

Cell Uptake (RAW264.7 macrophage)

2.5 x 10⁵ RAW264.7 (monocyte / macrophage) cells were cultured in regular growth medium, high glucose Dulbecco's modified Eagle's medium (DMEM) supplemented with 10% fetal bovine serum (FBS), 100 U/mL penicillin, and 100 mg/mL streptomycin per well in a 6 well plate. The culture was kept at 37°C in an atmosphere of 5% CO₂ and 95% air. After 24 hours of cell attachment, the cells were incubated with 40 µg of SH-RITC@MSN-PEG particles in 2mL serum-free medium for 4 hours.

Flow Cytometry for Cell Uptake Quantification

Treated cells were washed twice with serum-free medium, and then harvested by trypsinization. About 7.5x10⁵ cells were collected and centrifuged at 3000 rpm for 5 minutes. And the cell pellets were well dispersed in 400 µL phosphate-buffered saline (PBS) solution. The red emitting rhodamine B (RITC) dye, which was excited at 488 nm with an Argon Laser and detected at wavelength in the 560 to 590 nm range, incorporated in mesoporous silica nanoparticles could serve as a marker to quantitatively determine their cell uptake results by FACSCalibur flow cytometry and programmed by CellQuest Pro software.

3.2.5 Characterization

Elemental Analysis (EA)

To determine the amounts of thiol groups on SH@MSN, we used elemental analyzer to analyze the sulfur element. SH@MSN containing different amount of thiol groups by adding various MPTMS in the synthetic process was first dried at 60°C for 24 hours and well grounded. And about 4 mg of SH@MSN powder samples were prepared for EA analysis with no MPTMS modified MSN as the reference. The experiment was performed by Instrumentation Center National Taiwan University with Heraeus varioEL-III (for NCSH).

Transmission Electron Microscopy (TEM)

JOEL JEM-1230 electron microscope instrument was used to take TEM images under the voltage of 100 kV. Samples were first well dispersed in ethanol at a very low concentration (0.2 mg / mL) and 10 μ L of the suspension was dropped onto a microgrid and dried at room temperature.

Dynamic Light Scattering (DLS)

1mL of the SH-RITC@MSN-PEG ethanol solution (1mg/mL) was centrifuged at 16000 for 30 minutes and resuspended in 3mL of PBS, regular growth

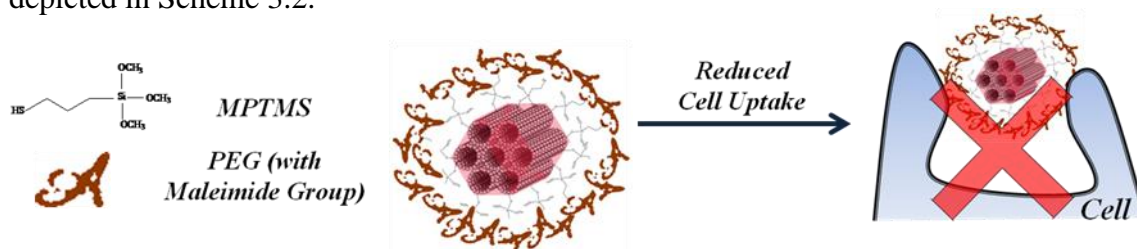
medium (high glucose DMEM supplemented with 10% FBS, 100 U/mL penicillin, and 100 mg/mL streptomycin), or serum free medium. The hydrodynamic sizes of SH-RITC@MSN-PEG dispersed in various solutions were obtained after incubated for 30 minutes, 6 hours, 12 hours or 2 weeks with MALVEN Nano-ZS. For incubation time longer than 30 minutes, all the samples were kept under 4 °C to avoid the propagation of bacterium and recover to room temperature before the measurement.

Zeta Potential

Zeta potential measurements were achieved by dispersing 1mg SH-RITC@MSN or SH-RITC@MSN-PEG in 3mL of nanopure water followed by detecting with MALVEN Nano-ZS at room temperature.

3.3 Results and Discussion

Mesoporous silica nanoparticles (MSN) are emerging as promising candidates for target-specific delivery and biomedical imaging due to its large pore volume, high surface area, uniform particle size, high biocompatibility and ease of surface functionalization. However, the destabilization due to the adsorption of plasma proteins in cell-culture medium⁵⁵ and tendency to aggregate upon exposure to physiological conditions⁶⁰, and non-specific uptake by macrophage cells from reticular-endothelial system (RES) are the most encountered problems when applying MSN for *in vivo* applications. In either case mentioned above, MSN materials would be rapidly removed from the blood circulation system and lose the chance to enter targeting places. Hence in the present work, we successfully demonstrated a systematic study of PEG functionalized 50 nm red-emitting dye conjugated MSN (SH-RITC@MSN-PEG) on the stability of the nanoparticles in the physiological conditions. The resulted nanoparticles possess high stability in physiological environment and under cell culture conditions, and significantly reduced non-specific uptake by RAW 264.7 macrophage cells as depicted in Scheme 3.2.



Scheme 3.2 The formation and application of SH-RITC@MSN-PEG.

3.3.1 Quantification of Thiol Group

In our work, mesoporous silica nanoparticles (MSNs) modified with thiol groups (SH@MSN) offered by (3-Mercaptopropyl)-trimethoxysilane (MPTMS) were covalently conjugated with the PEG-maleimide through maleimide / thiol chemistry. In order to quantify the amounts of PEG on the surface of MSN, we first had to determine the amounts of thiol groups from SH@MSN with elemental analyzer by analyzing the sulfur element from the thiol group.

We reasoned that the PEGylation of MSN should be only on the surfaces of MSN instead of inside the pores since this could most possibly make PEG chains extend far away from the surfaces of MSN enhancing their repulsion against opsonin proteins.^{52,58} Besides, the loading efficiency of the mesopores won't be affected if the pores were not occupied by PEG chains. Hence, MSNs were conjugated with MPTMS before surfactant extraction. MSNs without extracting surfactants were then modified with various amounts of thiol group (-SH) containing silane, MPTMS, by heating different volumes of MPTMS and MSN in ethanol for 6 hours to obtain SH@MSN with various sulfur elements as shown in Table 3.3. It was found that an increase in the MPTMS added during the synthetic process resulted in a higher weight percentage of sulfur element, indicating more thiol groups had been conjugated to MSN. The amount of sulfur was increased from 2.95 % to 5.9 % with the amount of MPTMS from 100 μ L

to 250 μL .

Though the saturated sulfur amount was not achieved by our MPTMS adding conditions, it pointed out the potential for further chemical functionalization with excess amounts of silane retained on the surface of MSN. These remained free silanol groups are able to do other functionalization increasing its capability for further applications. Besides, surface covered with too many PEG chains would limit their mobility resulting in the decrease of steric hindrance property⁵². Therefore, we decided to add 250 μL of MPTMS in latter synthetic process since it possessed the large but not too much amount of MPTMS and still provided the free silanol groups.

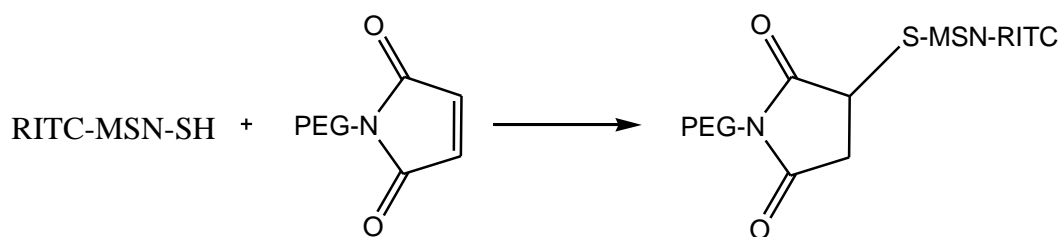
Table 3.3 Quantification of sulfur elements (w.t.%) from thiol groups on SH@MSN by adding different amounts of MPTMS

Sample with different MPTMS(μL)	N%	C%	S%	H%
0	0.133	3.860	0.000	2.859
100	0.175	8.983	2.952	2.810
200	0.193	10.145	4.100	2.755
250	0.180	11.772	5.909	3.032

3.3.2 Systematic Study of PEGylation of Rhodamine B Dye Conjugated MSN

(SH-RITC@MSN-PEG)

Mesoporous silica nanoparticle (MSN) was first conjugated with rhodamine B dye (RITC) via one-pot co-condensation method by adding organic dyes to an ammonia solution containing dilute tetraethyl orthosilicate (TEOS) and low surfactant concentration. The resulting product, RITC@MSN, possessed the red-light emitting property which could be served for later flow cytometry analysis to investigate the RAW 264.7 macrophage cells uptake. Then as-synthesized RITC@MSN was modified with (3-Mercaptopropyl)-trimethoxysilane (MPTMS) to generate nanoparticles with both organic dye and thiol functional group (SH-RITC@MSN) on its surface since the surfactants remained unextracted. The attached amounts of MPTMS were shown in Table 3.3. The structure directing surfactant was acid extracted to form the surfactant free SH-RITC@MSN before conjugated with PEG-maleimide. The PEG was covalently anchored on the surface of SH-RITC@MSN by maleimide thiol reaction to yield a thioether.⁶¹



Scheme 3.3 Mechanism of thiol PEGylation.

Conjugation with PEG

The surface chain density (or the thickness of PEG layer) and molecular weights of PEG chains would directly influence the flexibility and hydrophilicity of nanoparticles⁵⁸, and consequently their stability in cell culture and physiology environment. Moreover, their steric repulsion against serum proteins and macrophage cells would also be affected by PEG molecular weight and surface chain thickness. Hence, we carried a systematic study to find out the optimal PEG molecular weight and surface chain density of SH-RITC@MSN-PEG for both stability in cell culture and minimum non-specific uptake by macrophage cells. Series of PEG solutions with different molar ratio of thiol groups to PEG (including 1:1, 2:1 and 4:1), which would result in various surface chain density, and PEG molecular weights (M.W. = 10, 20 and 30 kDa) were prepared the study as depicted in Table 3.4 where A to I are the codes representing for the specific condition.

Table 3.4 SH-RITC@MSN-PEG_{A-I} with nine combinations of mole ratio of thiol groups to PEG and PEG molecular weights.

M.W. \ Ratio^a	1:1	2:1	4:1
PEG M.W. = 10 kDa	A	D	G
PEG M.W. = 20 kDa	B	E	H
PEG M.W. = 30 kDa	C	F	I

^aRatio represents the molar ratio of “thiol groups modified on the surface of SH-RITC@MSN” to “PEG”

The Morphology and Mesostucture of MSNs (SH-RITC@MSN) and PEGylated MSNs (SH-RITC@MSN-PEG)

Transmission electron microscopy (TEM) measurements from Figure 3.3 showed that both MSN without PEG (SH-RITC@MSN) and PEGylated MSN (SH-RITC@MSN-PEG_{A-I}) had uniform size about 50 nm and all showed highly ordered mesoporous channels in [001] and [110] directions. Besides, well-defined hexagonal edges and single crystal morphology indicated that PEGylated MSNs from Figure 3.3 (A) to (I) maintained the completeness of hexagonal pore structures and retained the similar sizes around 50 nm compared to MSN without PEG from Figure 3.3 (O).

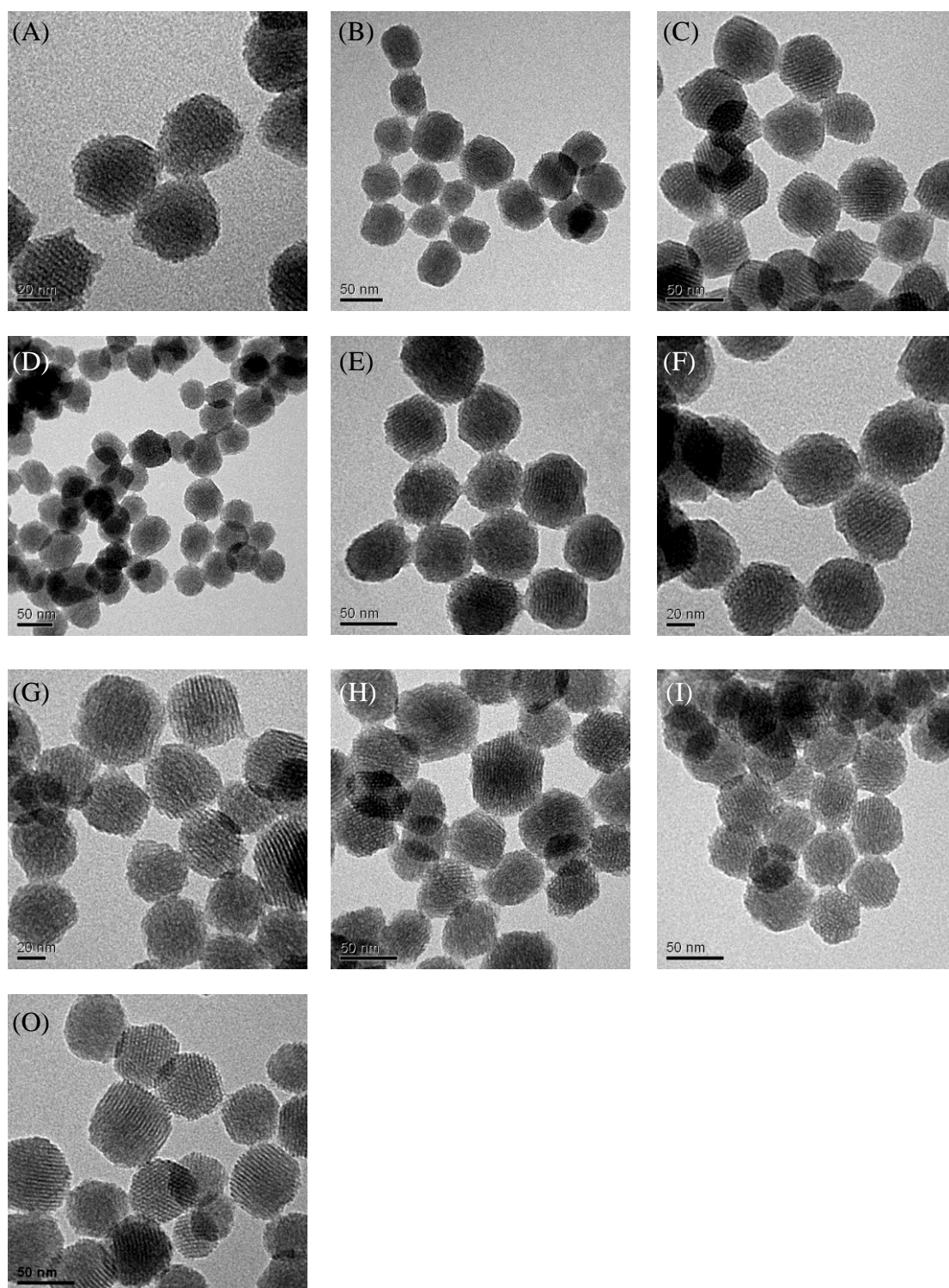


Figure 3.3 TEM images of (A) to (I) SH-RITC@MSN-PEG_{A-I} and (O) SH-RITC@MSN.

Stability of the SH-RITC@MSN-PEG measured by Dynamic Light Scattering

The size stability of the particles in physiology environment is very important for *in vivo* application since particles with larger hydrodynamic sizes typically exhibit more rapid clearance rate and short blood circulation time.⁵² However it is a significant challenge to retain the stability of nanoparticles in application-associated environments.

⁶² Aiming at efficient biomedical applications, such as target-specific delivery, we demonstrated the stability of SH-RITC@MSN-PEG by suspending the nanoparticles in three commonly used biological media: phosphate-buffered solution (PBS), Dulbecco's modified Eagle's medium (DMEM), and Dulbecco's modified Eagle's medium with 10% of fetal bovine serum (DMEM-FBS). And dynamic light scattering (DLS) was used to track the size change of the nanoparticles during the incubation.

Figures 3.4 and 3.5 show the hydrodynamic diameters of the nanoparticles coated with various PEGs (SH-RITC@MSN-PEG_{A-1}) in PBS and DMEM, respectively, with nanoparticles without PEG coating (SH-RITC@MSN) as the control. With the increase of PEG molecular weights and surface chain densities, the size stability became more and more remarkable. And SH-RITC@MSN-PEG_C, the one conjugated with highest molecular weight of PEG 30k and molar ratio of thiol groups to PEG (1:1) appeared to be the optimal one for nanoparticle hydrodynamic stability. It showed negligible aggregation even during an incubation period of 2 weeks. Apparently, the

extended nanoparticle stability in biological media may be attributed to the highly stable and dense PEG coatings.⁶² The steric hindrance of hydrophilic PEG chains made the significant contribution to preventing the nanoparticle agglomeration. Higher molecular weight and higher surface density would result in stronger hydrophilicity and repulsion toward aggregation.

Besides, the electrostatic interaction of the surface charges also played an important role in affecting the size changes of nanoparticles. Nanoparticles are typically electrically charged to achieve the stability in various solutions by electrostatic repulsion. However, those electrostatically stabilized nanoparticles are easy to aggregate in biological environments due to the neutralization of the surface charges resulted from salts, electrolytes and other ionic species in the media.⁶²⁻⁶³ From Table 3.5, the SH-RITC@MSN samples possessed highly negative zeta potential of about -27mV in pure water whereas PEGylated MSNs had much lower absolute value in zeta potentials around -5mV to -17mV. Besides, absolute values of PEGylated MSNs decreased as the molecular weight of PEG chains increased possibly due to the shielding effect resulted from the PEG layers surrounding nanoparticle cores.⁶⁴ Hence, the decrease of absolute zeta potential values resulted in the charge shielding effect to help PEGylated particles evading from ionic species and stabilized in biological media.

Furthermore, we also discovered another phenomenon which hasn't been

reported before: PEGylated MSN (SH-RITC@MSN) without the optimized PEG molecular weight and surface chain density would perform worse stability compared to normal MSNs (SH-RITC@MSN-PEG) by exhibiting apparent size increase and particle precipitation as shown in Figures 3.4 and 3.5. A plausible explanation is proposed as the following. The steric hindrance effect and surface negative charge shielding could make only few contributions to the stabilization of nanoparticle sizes when the coated molecular weights and surface density of PEG chains are not optimal. Besides, the molecular weight of PEG chain would bring the nanoparticles to higher mass which may facilitate its precipitation rate and result in undispersible agglomeration and large hydrodynamic sizes.

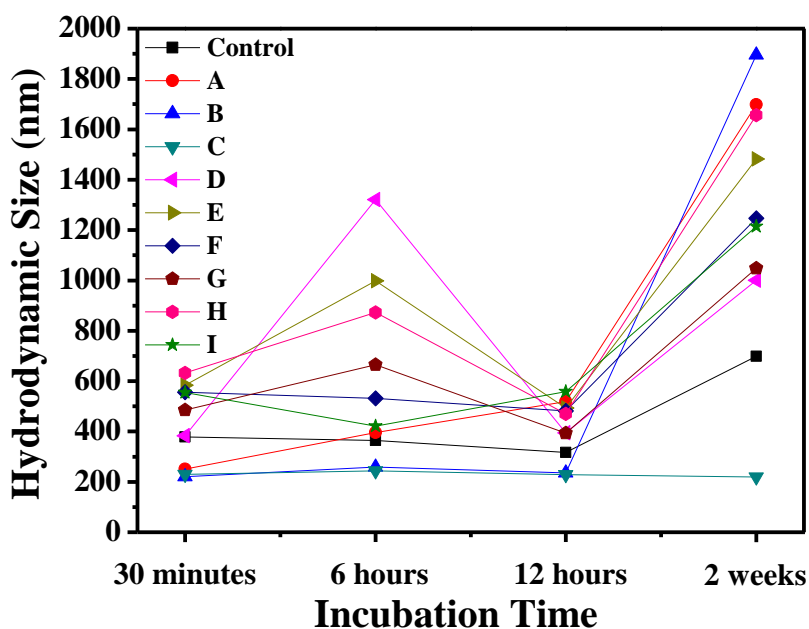


Figure 3.4 Hydrodynamic size changes in PBS for various incubation periods. Control is SH-RITC@MSN whereas A to I corresponds to PEGylated MSNs in Table 3.4.

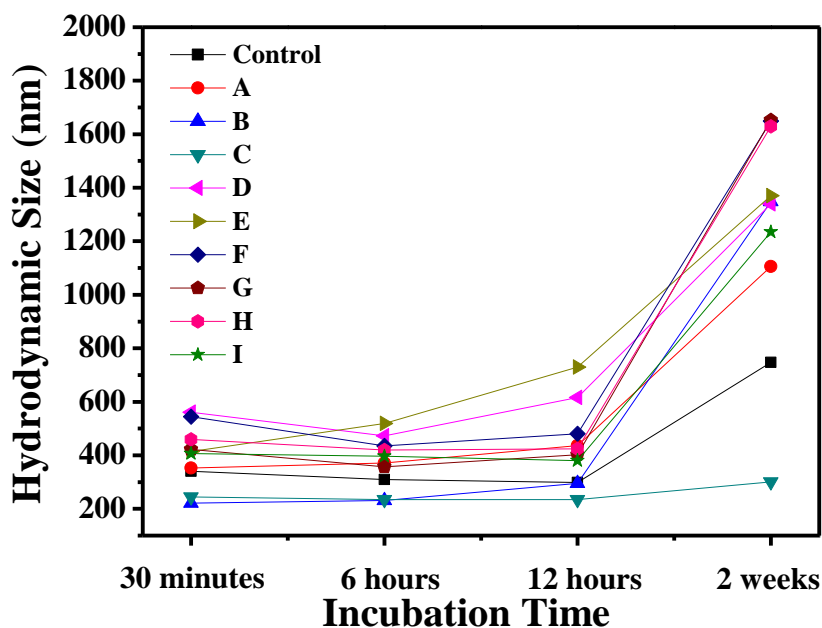


Figure 3.5 Hydrodynamic size changes in DMEM for various incubation periods.

Control is SH-RITC@MSN whereas A to I corresponds to PEGylated MSNs in Table 3.4.

Table 3.5 The comparison of zeta potentials of MSNs (SH-RITC@MSN) and PEGylated MSNs (SH-RITC@MSN-PEG) with PEG=xk;1:1 chains of different molecular weights (x=10, 20 and 30) at the mole ratio of thiol groups to PEG (1:1) in water

Sample	Zeta Potential (mV)
Control (SH-RITC@MSN)	-27.4
SH-RITC@MSN-PEG _{A=10k} ;1:1	-17.5
SH-RITC@MSN-PEG _{B=20k} ;1:1	-13.4
SH-RITC@MSN-PEG _{C=30k} ;1:1	-5.08

Figure 3.6 demonstrates the hydrodynamic size change of the nanoparticles coated with PEG chains (SH-RITC@MSN-PEG_{A-I}) in DMEM plus 10% FBS (DMEM-FBS) with MSN materials without PEG coating (SH-RITC@MSN) as the control. Insignificant size change was observed after incubation of nanoparticles in the DMEM-FBS medium even after 2 weeks, demonstrating excellent stability of both PEGylated MSN and MSN without PEG coating in protein containing medium.

For PEGylated MSNs, the steric repulsion and hydrophilicity of PEG chains against FBS could prevent the FBS adsorption and hence cause no obvious agglomeration. Besides the hydrophilicity and steric hindrance of PEG chains, it is believed that ionic interaction might be another factor for serum adhesion. It has been found that strong negative charge would attract more proteins compared to those neutral and positively charged ones.⁶² Thus, MSN coated with PEG chains possessed decreased absolute value of zeta potential as shown in Table 3.5 would help the nanoparticles evading from serum adsorption and size increase. Also, the proteins dispersed in the culture media would also provide the steric hindrance for nanoparticle aggregation.

On the other hand, SH-RITC@MSN without repulsive hindrance from PEG and bearing the highly negative zeta potential are believed contributing to the increased protein adhesion. However, the protein adhesion here might help stabilize the nanoparticles due to the protein block effect which avoided the interferences from the

ionic species in the media and offered steric hindrance against agglomeration.

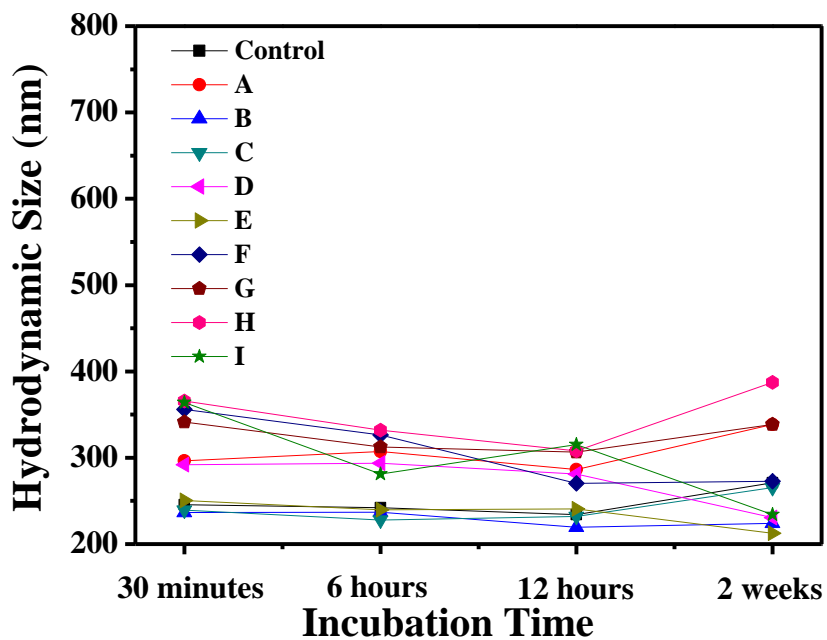


Figure 3.6 Hydrodynamic size changes in DMEM plus 10% FBS for various incubation periods. Control is SH-RITC@MSN whereas A to I corresponds to PEGylated MSNs in Table 3.4.

Macrophage Uptake Assay of SH-RITC@MSN-PEG

In order to study the uptake of the PEGylated MSN materials by the innate immune system, we incubated SH-RITC@MSN and SH-RITC@MSN-PEG_{B,C,E,H} with RAW 264.7 which is one kind of macrophage cell lines. The PEGylated MSNs used here are B, C, E, and H (responding to Table 3.5) since the PEGylation conditions of C contributed to the most stable and prolonged particle stability; besides, B could also sustained the particle stability from the culture media for 12 hours, and E and H were prepared for the systematic comparison with B. We planned to find out the optimized condition which could both significantly reduce the uptake by macrophage cells and evade from the particle aggregation.

Cell Uptake Assay under DMEM: RAW 264.7 cells were isolated, expanded and then incubated with 40 µg / mL of MSN without PEG coating (SH-RITC@MSN) and nanoparticles coated with PEG chains (SH-RITC@MSN-PEG_{B,C,E,H}) in serum-free low glucose Dulbecco's modified Eagle's medium (DMEM) for 4 hours. In the flow cytometry data (Figure 3.7), typical histograms of fluorescence intensity of RAW 264.7 that were incubated with different MSN nanoparticles were displayed. And the data showed 1) MSN without PEG conjugation (Figure 3.7 (B)) gave the highest uptake, followed by PEG_{B,E,H=20k}-coated nanoparticles (Figure 3.7 (D)-(F)), of which the uptake is about 60% -70% of that from the non-PEGylated MSN; 2) the uptake of PEG_{C=30k}

coated MSNs (Figure 3.7 (C)) is negligible compared with the background (Figure 3.7 (A)); 3) interestingly, the uptake efficiency of three PEG_{B,E,H=20k}-coated nanoparticles didn't show much difference and apparent trend among each other. The analyses on the percentage of nanoparticles-labeled cells as illustrated in Figure 3.8 also supported the previous observation.

It was reported the cell adhesion and phagocytosis are dependent on the surface free energy which is positively related to the surface, indicating the phagocytosis increases as the negative zeta potential increases.⁵⁸ Hence the high phagocytosis percentage of non-PEGylated MSN could mainly due to its high negative value of zeta potential as depicted in Table 3.6. And the phagocytosis of PEGylated MSNs was hindered because of the shielding of negative charges by PEG chains. Their phagocytosis percentage decreased greatly as the molecular weight of PEG chain increased from 20k Dalton to 30k Dalton. Besides, the similar uptake results of three PEG_{B,E,H=20k}-coated MSN nanoparticles could also probably be resulted from their similar negative value of zeta potential as shown in Table 3.6.

The enhanced hydrophilicity of PEG chains would be another important factor contributed to the reduction of macrophage cell uptake. Since PEG chains of larger molecular weights are more hydrophilic, PEG_{C=30k}-coated MSN showed about only 2% - 3% of uptake of that from PEG_{B,E,H=20k}-coated nanoparticles.

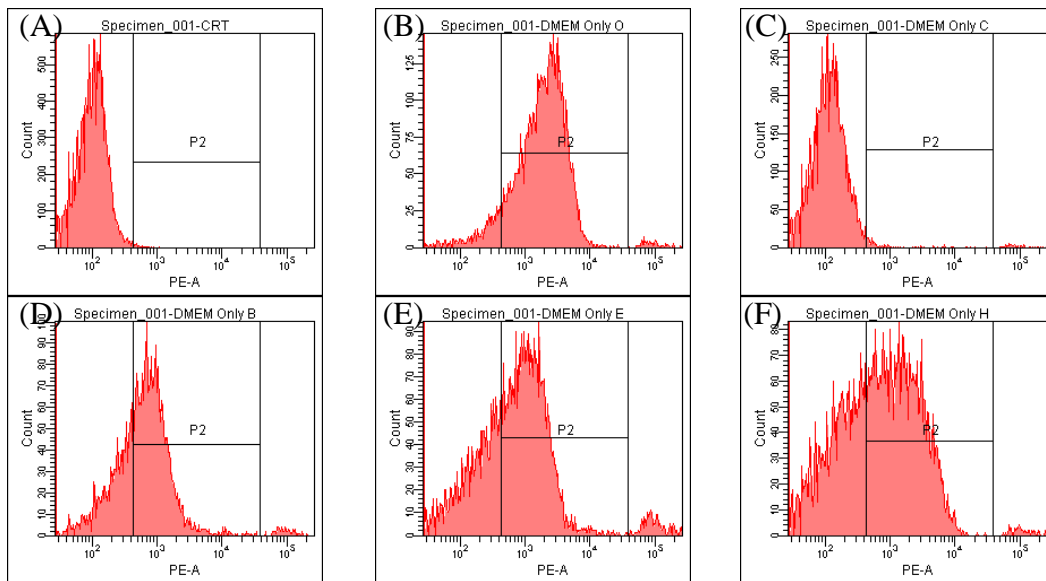


Figure 3.7 Cellular uptake of SH-RITC@MSN and SH-RITC@MSN-PEG_{B,C,E,H} in RAW 264.7 in DMEM using flow cytometry. (A) RAW 264.7 without treatment. RAW264.7 treated with (B) SH-RITC@MSN, (C) SH-RITC@MSN-PEG_C, (D) SH-RITC@MSN-PEG_B, (E) SH-RITC@MSN-PEG_E and (H) SH-RITC@MSN-PEG_H.

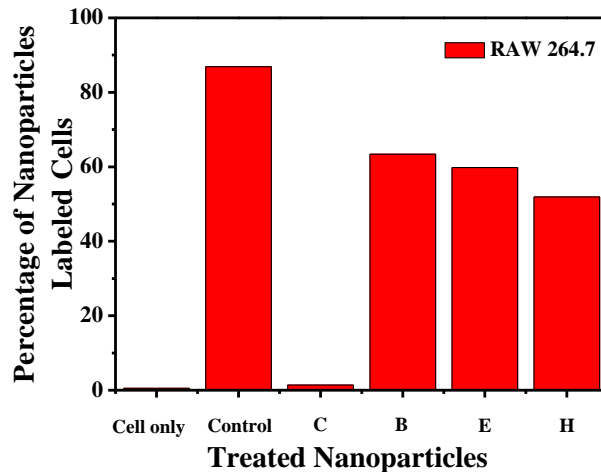


Figure 3.8 Flow cytometry determination of SH-RITC@MSN and SH-RITC@MSN-PEG_{B,C,E,H} uptake RAW 264.7 under DMEM, analyzed by the percentage of nanoparticle labeled cells. Cell only is RAW 264.7 without treatment. Cells treated with SH-RITC@MSN are control. C to H is treated with SH-RITC@MSN-PEG_{C,B,E,H}.

Table 3.6 The zeta potentials of MSNs (SH-RITC@MSN) and PEGylated MSNs (SH-RITC@MSN-PEG) by PEG=xk;y:z chains of different molecular weights (x=20 and 30) with various mole ratios of thiol groups to PEG (y:z) in water.

Sample	Zeta Potential (mV)
Control (SH-RITC@MSN)	-27.4
SH-RITC@MSN-PEG _{C=30k;1:1}	-5.08
SH-RITC@MSN-PEG _{B=20k;1:1}	-13.4
SH-RITC@MSN-PEG _{E=20k;2:1}	-18.1
SH-RITC@MSN-PEG _{H=20k;4:1}	-16

Cell Uptake Assay under DMEM-FBS: We also incubated RAW 264.7 cells with 40 µg / mL of MSN without PEG coating (SH-RITC@MSN) and nanoparticles coated with PEG chains (SH-RITC@MSN-PEG_{B,C,E,H}) in low glucose Dulbecco's modified Eagle's medium supplemented with 10% FBS (DMEM-FBS) for 4 hours. Typical histograms of fluorescence intensity of RAW 264.7 that were incubated with different MSN nanoparticles analyzed by flow cytometry (Figure 3.9) were displayed. Also, the quantitative analyses of cells expressing red fluorescence by converting the cell populations in flow cytometry data to percentage were shown in Figure 3.10. RAW 264.7 cells incubated with nanoparticle in DMEM-FBS showed significantly reduced cellular uptake no matter MSNs were PEGylated or not as compared to the uptake behaviors with nanoparticles treatment in serum free DMEM as presented in Figures 3.7 and 3.8. This was because proteins of FBS in the media blocked the nanoparticles from

contacting with the macrophage cells and thus reduced the uptake possibilities.

However, MSN without PEG coating (SH-RITC@MSN) still possessed much higher uptake efficiency compared to the PEGylated MSNs as presented in Figure 3.9 and 3.10. It may be resulted from the nonspecific adsorption of serum proteins onto the MSN surface; these adhered proteins induced the MSN to enter into cells via the receptor-mediated endocytosis⁶⁵ resulting in the higher cellular uptake. The relatively higher uptake efficiency of SH-RITC@MSN-PEG_{H=20k;4:1} was also likely caused by their less covered particle surfaces and resulted in higher protein adsorption. The overall results indicated that PEG modified MSN, SH-RITC@MSN-PEG, showed much less uptake by macrophage cells, meaning that these nanoparticles can escape from the reticular-endothelial system (RES) and have longer blood circulation time.

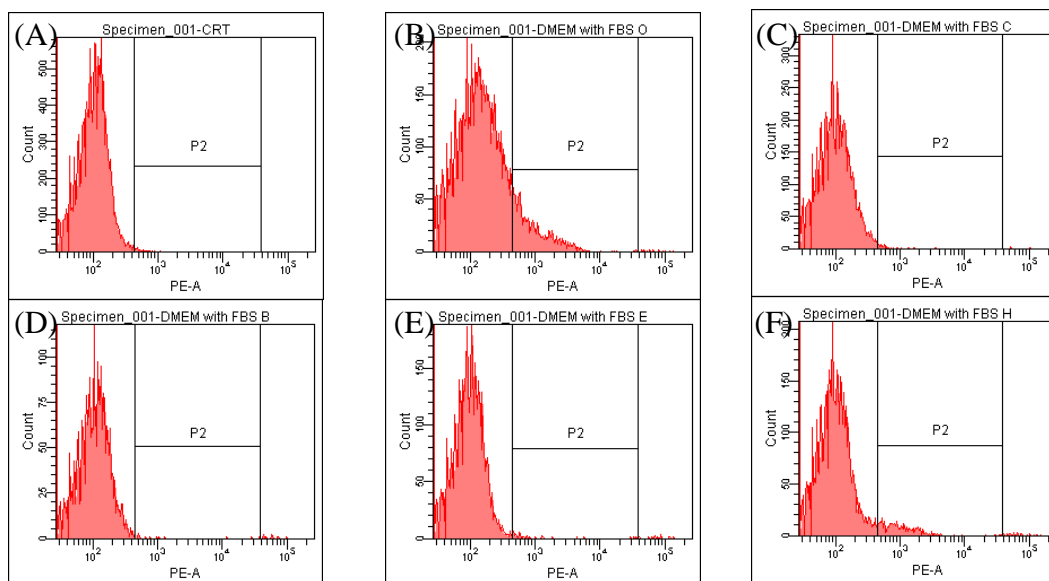


Figure 3.9 Cellular uptake of SH-RITC@MSN and SH-RITC@MSN-PEG_{B,C,E,H} in RAW 264.7 in DMEM-FBS using flow cytometry. (A) RAW 264.7 without treatment. RAW264.7 treated with (B) SH-RITC@MSN, (C) SH-RITC@MSN-PEG_C, (D) SH-RITC@MSN-PEG_B, (E) SH-RITC@MSN-PEG_E and (H) SH-RITC@MSN-PEG_H.

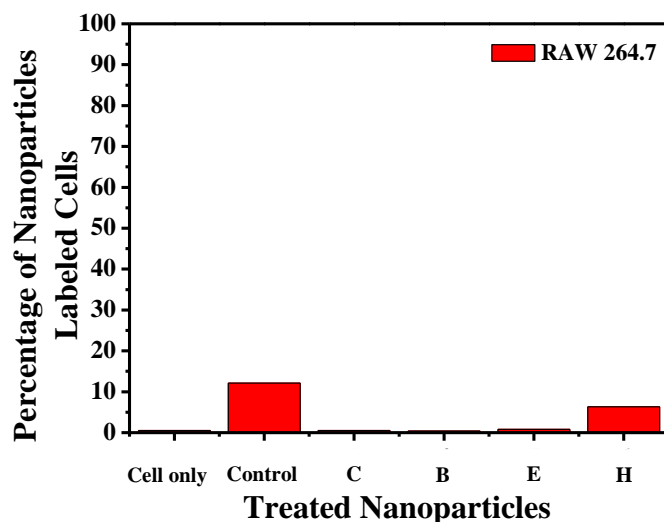


Figure 3.10 Flow cytometry determination uptake of SH-RITC@MSN and SH-RITC@MSN-PEG_{B,C,E,H} by RAW 264.7 in DMEM-FBS, analyzed by the percentage of nanoparticle labeled cells. Cell only is RAW 264.7 without treatment. Cells treated with SH-RITC@MSN is denoted as control. And C to H is SH-RITC@MSN-PEG_{C,B,E,H} treated.

3.4 Conclusion

To sum up, MSNs with particle size of 50 nm were PEGylated by covalently conjugating mPEG_{xk;y:z}-maleimide with differently molecular weights ($x = 10, 20, 30$) and mole ratio of thiol groups to PEG (1:1, 2:1, 4:1) on the outer surfaces of MSNs. Both molecular weight and conjugation ratio significantly affected the hydrodynamic size stability in culture media and the phagocytosis of RAW 264.7 macrophage cells. The most optimal molecular weight was PEG_{=30k}-MSN and the highest surface chain density achieved was 1:1 by mole ratio of thiol groups to PEG, with that configuration, particles showed excellent stability without obvious size increase during an incubation period of 2 weeks. Besides, it also showed much reduced non-specific uptake by RAW 264.7 macrophage cells, far lower than that of MSNs without PEGylation. More importantly, the size stability under physiology environments which helped PEGylated MSNs avoiding agglomeration and much less macrophage uptake suggest their high chance to escape from reticular-endothelial system (RES). Besides, the free silanol groups on the particle surface allow other chemical functionalization and unoccupied pores remained for further cargo loadings make these PEGylated MSNs ideal candidates for the enhancement of target-specific efficiency in drug delivery and other biomedical applications.

Reference:

- [1] M. De, P. S. Ghosh, V. M. Rotello, *Adv. Mater.* **2008**, 20, 4225-4241.
- [2] Y. Piao, A. Burns, J. Kim, U. Wiesner, T. Hyeon, *Adv. Funct. Mater.* **2008**, 18, 3745-3758.
- [3] W. Stöber, A. Fink, E. Bohn, *J. Colloid Interface Sci.* **1968**, 26, 62.
- [4] K. Osseo-Asare, F. J. Arriagada, *Colloids Surf.* **1990**, 50, 321.
- [5] J. Kim, S. Park, J. E. Lee, S. M. Jin, J. H. Lee, I. S. Lee, I. Yang, J.-S. Kim, S. K. Kim, M.-H. Cho, T. Hyeon, *Angew. Chem. Int. Ed.* **2006**, 45, 7754.
- [6] X. Michalet, F. F. Pinaud, L. A. Bentolila, J. M. Tsay, S. Doose, J. J. Li, G. Sundaresan, A. M. Wu, S. S. Gambhir, S. Weiss, *Science* **2005**, 307, 538-544.
- [7] A. K. Gupta, M. Gupta, *Biomaterials* **2005**, 26, 3995-4021.
- [8] T. K. Jain, M. K. Reddy, M. A. Morales, D. L. Leslie-Pelecky, V. Labhasetwar, *Mol. Pharm.* **2008**, 5, 316-327 ; T. K. Jain, M. A. Morales, S. K. Sahoo, D. L. Leslie-Pelecky, V. Labhasetwar, *Mol. Pharm.* **2005**, 2, 194-205.
- [9] M.-C. Daniel, D. Astruc, *Chem. Rev.* **2004**, 104, 293-346.
- [10] R. A. Sperling, P. R. Gil, F. Zhang, M. Zanella, W. J. Parak, *Chem. Soc. Rev.* **2008**, 37, 1896-1908.
- [11] C. T. Kresge, M. E. Leonowicz, W. J. Roth, J. C. Vartuli, J. S. Beck, *Nature* **1992**, 359, 710-712.
- [12] U. Ciesla, F. Schüth, *Microporous and Mesoporous Material* **1999**, 131-149.
- [13] J. Y. Ying, C. P. Mehnert, M. S. Wong, *Angew. Chem. Int. Ed.* **1999**, 38, 56-77.
- [14] I. I. Slowing, B. G. Trewyn, S. Giri, Victor S.-Y. Lin, *Adv. Func. Mater.* **2007**, 17, 1225-1236.
- [15] S.-H. Wu, Y.-S. Lin, Y. Hung, Y.-H. Chou, Y.-H. Hsu, C. Chang, C.-Y. Mou, *ChemBioChem* **2008**, 9, 53-57.
- [16] A. B. Descalzo, D. Jimenez, M. D. Marcos, R. Martínez-Máñez, J. Soto, J. E.

- Haskouri, C. Guillém, D. Beltrán, P. Amorós, M. V. Borrachero, *Adv. Mater.* **2002**, 14, 966-969.
- [17] Y.-S. Lin, C.-P. Tsai, H.-Y. Huang, C.-T. Kuo, Y. Hung, D.-M. Huang, Y.-C. Chen, C.-Y. Mou, *Chem. Mater.* **2005**, 17, 4570-4573.
- [18] C.-H. Lee, L.-W. Lo, C.-Y. Mou, C.-S. Yang, *Adv. Funct. Mater.* **2008**, 18, 3283-3292.
- [19] J. L. Vivero-Escoto, I. I. Slowing, C.-W. Wu, Victor S.-Y. Lin, *J. Am. Chem. Soc.* **2009**, 131, 3462-3463.
- [20] T. F. Massoud, S. S. Gambhir, *Genes Dev.* **2003**, 17, 545-580.
- [21] H. B. Na, I. C. Song, T. Hyeon, *Adv. Mater.* **2009**, 21, 2133-2148.
- [22] J. Cheon, J.-H. Lee, *Acc. Chem. Res.* **2008**, 41, 1630-1640.
- [23] J. Kim, Y. Piao, T. Hyeon, *Chem. Soc. Rev.* **2009**, 38, 372-390.
- [24] C.-H. Lee, S.-H. Cheng, Y.-J. Wang, Y.-C. Chen, N.-T. Chen, J. Souris, C.-T. Chen, C.-Y. Mou, C.-S. Yang, L.-W. Lo, *Adv. Func. Mat.* **2009**, 19, 215-222.
- [25] D. Weishaupt, V. D. Köchli, B. Marincek, *How does MRI work?*, Springer, New York **2006**.
- [26] K. N. Raymond, V. C. Pierre, *Bioconjugate Chem.* **2005**, 16, 3-8.
- [27] P. Caravan, J. J. Ellison, T. J. McMurry, R. B. Lauffer, *Chem. Rev.* **1999**, 99, 2293-2352.
- [28] P. Caravan, *Chem. Soc. Rev.* **2006**, 35, 512-523.
- [29] A. Datta, J. M. Hooker, M. Botta, M. B. Francis, S. Aime, K. N. Raymond, *J. Am. Chem. Soc.* **2008**, 130, 2546-2552.
- [30] D. E. Prasuhn, Jr., R. M. Yeh, A. Obenaus, M. Manchester, M. G. Finn, *Chem. Commun.* **2007**, 1269-1271.
- [31] Y. S. Lin, *Master Thesis* **2004**.
- [32] B. V. Enüstün, J. Turkevich, *J. Am. Chem. Soc.* **1963**, 85, 3317-3328.

- [33]J. Liu, Z. Sun, Y. Deng, C. Li, X. Guo, L. Xiong, Y. Gao, F. Li, D. Zhao, *Angew. Chem. Int. Ed.* **2009**, 48, 5875-5879.
- [34]C. T. Tseng, *Master Thesis* **2009**.
- [35]S.-J. Park, Y. J. Kim, S.-J. Park, *Langmuir* **2008**, 24, 12134-12137.
- [36]Y. S. Lin, Y. Hung, J. K. Su, R. Lee, C. Chang, M. L. Lin, C. Y. Mou, *J. Phys. Chem. B* **2004**, 108, 15608-15611.
- [37]C. Platas-Iglesias, L. Vander Elst, W. Zhou, R. N. Muller, C. F. G. C. Geraldles, T. Maschmeyer, J. A. Peters *Chem. Eur. J.* **2002**, 8, 5121-5131.
- [38]P.A. Rinck, R.N. Muller, *Eur. Radiol.* **1999**, 9, 998-1004.
- [39]M. Takahashi, H. Uematsu, H. Hatabu, *Eur J. of Radiology* **2003**, 46, 45-52.
- [40]M. Gueron, *J. Magn. Reson.* **1975**, 19, 58.
- [41]J. F. Schenck, *Med. Phys.* **1996**, 23, 815-850.
- [42]H. B. Na, T. Hyeon, *J. Mater. Chem.* **2009**, 19, 6267-6273.
- [43]J. W.M Bulte, T. Douglas, B. Witwer, S.-C. Zhang, B. K Lewis, P. van Gelderen, H. Zywicke, Ian D Duncan BVMS, PhD, FRCVS, FRCPath and Joseph A Frank *Acad. Radiol.* **2002**, 9, S332–S335.
- [44]K. Hoshino, H. Q. Ly, J. V. Frangioni, R. J. Hajjar, *Prog Cardiovasc Dis.* **2007**, 49, 414-420.
- [45]W.-C. Lo, C.-H. Hsu, A. T. H. Wu, L.-Y. Yang, W.-H. Chen, W.-T. Chiu, W.-F. Lai, C.-H. Wu, J. G. Gelovani, W.-P. Deng, *J Nucl Med.* **2008**, 49, 1512-1519.
- [46]C. P. Tsai, Y. Hung, Y. H. Chou, D. M. Huang, J. K. Hsiao, C. Chang, Y. C. Chen, C. Y. Mou, *small* **2008**, 4, 186-191; C. P. Tsai, *Docteral Dissertation* **2008**.
- [47]D. M. Huang, Y. Hung, B. S. Ko, S. C. Hsu, W. H. Hsu, C. L. Chien, C. P. Tsai, C. T. Kuo, J. C. Kang, C. S. Yang, C. Y. Mou, Y. C. Chen, *Faseb J.* **2005**, 19, 2014-2016.
- [48]N. Takaya, H. Watanabe, F. Mitsumori, *Proc. Intl. Soc. Mag. Reson. Med.* **2004**, 11.

- [49] Y. Xu, X. Zhu, H. S. Hahm, W. Wei, E. Hao, A. Hayek, S. Ding. *PNAS* **2010**, 107, 8129-8134.
- [50] S. Mornet, S. Vasseur, F. Grasset, E. Duguet, *J. Mater. Chem.* **2004**, 14, 2161-2175.
- [51] C. C Berry, A. S G Curtis, *J. Phys. D: Apply. Phys.* **2003**, 36, R198-R206.
- [52] D. E. Owens III, N. A. Peppas, *Inter. J. of Pharmaceutics* **2006**, 307, 93-102.
- [53] F. Alexis, E. Pridgen, L. K. Molnar, O.C. Farokhzad, *Molecular Pharmaceutics* **2008**, 5, 505-515.
- [54] S. M. Moghimi, H. M. Patel, *Adv. Drug Delivery Rev.* **1998**, 32, 45-60.
- [55] J. Xie, C. Xu, N. Kohler, Y. Hou, S. Sun, *Adv. Mater.* **2007**, 19, 3163-3166.
- [56] R. Gref, M. Lück, P. Quellec, M. Marchand, E. Dellacherie, S. Harnisch, T. Blunk, R.H. Müller, *Colloids Surf.* **2000**, 18, 301-313.
- [57] J. M. Chan, L. Zhang, K. P. Yuet, G. Liao, J.-W. Rhee, R. Langer, O. C. Farokhzad, *Biomaterials* **2009**, 30, 1627-1634.
- [58] Q. He, J. Zhang, J. Shi, Z. Zhu, L. Zhang, W. Bu, L. Guo, Y. Chen, *Biomaterials* **2010**, 31, 1085-1092.
- [59] S. D. Perrault, C. Walkey, T. Jennings, H. C. Fischer, W. C. W. Chan, *Nano Lett.* **2009**, 9, 1909-1915.
- [60] Y. S. Lin, C. L. Haynes, *Chem. Mater.* **2009**, 21, 3979-3986.
- [61] J. Kalia, R. T. Raines, *Bioorg. Med. Chem. Lett.* **2007**, 17, 6286-6289.
- [62] C. Fang, N. Bhattarai, C. Sun, M. Zhang, *small* **2009**, 5, 1637-1641.
- [63] C. Sun, J. S.H. Lee, M. Zhang, *Adv. Drug Delivery Rev.* **2008**, 60, 1252-1265.
- [64] K. Miyata, S. Fukushima, N. Nishiyama, Y. Yamasaki, K. Kataoka, *J. Controlled Release* **2007**, 122, 252-260.
- [65] B. D. Chithrani, A. A. Ghazani, W. C. W. Chan, *Nano Lett.* **2006**, 6, 662-668.